Synthesis and Control of Attosecond Light Transients

Mohammed Tharwat Hassan

München 2013

Synthesis and Control of Attosecond Light Transients

Mohammed Tharwat Hassan

Dissertation

an der Fakultät für Physik
der Ludwig-Maximilians-Universität
München

vorgelegt von
Mohammed Hassan
Aus Fayoum, Ägypten

München, February 2013

Erstgutachter: Prof. Ferenc Krausz
Zweitgutachter: Prof. Armin Scrinzi
Tag der mündlichen Prüfung: 14/3/2013.

Abstract

This thesis aims at extending the capabilities of ultrafast science in manipulating light fields. The instantaneous field of light transients has been tailored on demand with attosecond resolution by implementing ultrawideband field synthesis in the visible and flanking ranges. First experiments utilizing the considerably improved resolution, such as the study of ionization dynamics of the Kr atom, are conducted. Utilizing these transients, atoms are ionized for the first time by an optical field within a subfemtosecond time interval. By combining these transients with a synchronized EUV attosecond pulse the demonstration of the first attosecond pump probe experiment has been possible. The generated bound electron wave packets in the Kr^+ ion resulting from this interaction are measured to have nearly perfect coherence. By extending the synthesis to over more than two optical octaves, from Infrared (IR) to deep ultraviolet (UV), a new generation of tools in the science of light are generated. We call the tools the “attosecond light transients”. The first steps towards the control of bound electrons with these transients are taken.

Zusammenfassung

Diese Dissertation befasst sich mit der Erweiterung der Möglichkeiten der ultraschnellen Wissenschaft hinsichtlich der Manipulation von Lichtfeldern. Die Entwicklung und Umsetzung der spektral ultrabreitbandigen Lichtfeldsynthese im sichtbaren und angrenzenden Wellenlängenbreich ermöglicht die gezielte Formung der instantanen Lichtfeldtransienten mit einer Auflösung im Attosekundenbereich. Erste Experimente, bei denen die deutlich verbesserte Auflösung angewendet wurde, waren beispielsweise die Untersuchungen der Ionizationsdynamik des Kr Atoms. Unter Einsatz dieser Transienten werden Atome erstmals durch ein optisches Feld innerhalb von einem Zeitintervall von weniger als einer Femtosekunde ionisiert. Durch Kombination dieser Transienten mit zu diesen synchronisierten EUV Attosekundenpulsen, gelang die erstmalige Umsetzung eines Anrege-Abfrage-Experimentes, bei welchem die Pulslängen beider Pulse zugleich im Bereich von Attosekunden lagen. Das aus dieser Interaktion resultierende und detektierte, im Kr+ Ion gebundene Elektronenwellenpaket, weist eine fast vollständige Kohärenz auf. Die Verbreiterung der optischen Synthese auf über mehr als zwei optische Oktaven, beginnend im Infraroten bis zum fernen Ultraviolettbereich, stellt eine neue Generation von Werkzeugen in der Wissenschaft des Lichts bereit. Wir nennen diese Werkzeuge die „Attosekunden-Lichttransienten“. Erste Schritte zur gezielten Steuerung von gebundenen Elektronen werden unter Einsatz dieser Transienten durchgeführt.

Contents

Introduction

Light is a key tool for exploring and controlling the microcosm. Modern spectroscopic devices and techniques are using light in near infrared, visible and ultraviolet regions of the electromagnetic spectrum or even the soft X-rays and gamma rays to explore, with the finest spatial or spectral resolution, the detailed structure of matter down to the level of a single atom or a molecule.

The resolution that light can offer for tracing or driving dynamical processes in the microcosm is directly related to its waveform and, thus, to our capability to control it temporally. The validity of this conjecture has been proven by all essential achievements in the field of chronoscopy: from the pioneer experiments in 1899 by Abraham and Lemoine, in which electric spark-induced incoherent flashes of light were used to explore the Kerr response of matter [1] to the most innovative studies and applications enabled by the use of ultrashort coherent laser pulses [2], such as phenomena pertaining to molecular rotation, or the motion of atoms inside molecules or solids [3, 4], or even phenomena induced by electronic motions in atoms and molecules[5-9]. Over the last fifty years, the temporal resolution afforded by laser technology and light control has advanced through twelve orders of magnitude from the microsecond to the attosecond time scale.

Fig. 1 illustrates stages of the temporal control of light waves. The emission of incoherent light bursts—via an electrically induced spark—with the accuracy of this confinement roughly equal to the time it takes an electric discharge through a dilute gas in order to create a light flash (Fig. 1 (a)), is certainly one of the first steps. A gigantic leap on the temporal control of light has been made possible by the invention of coherent light sources, lasers[2]. The shaping of the temporal properties of coherent pulses (envelope) or the carrier frequency sweep across it (chirp) with gratings, prisms, pulse shapers and acousto-optic modulators was then possible as illustrated in Fig. 1 (b).

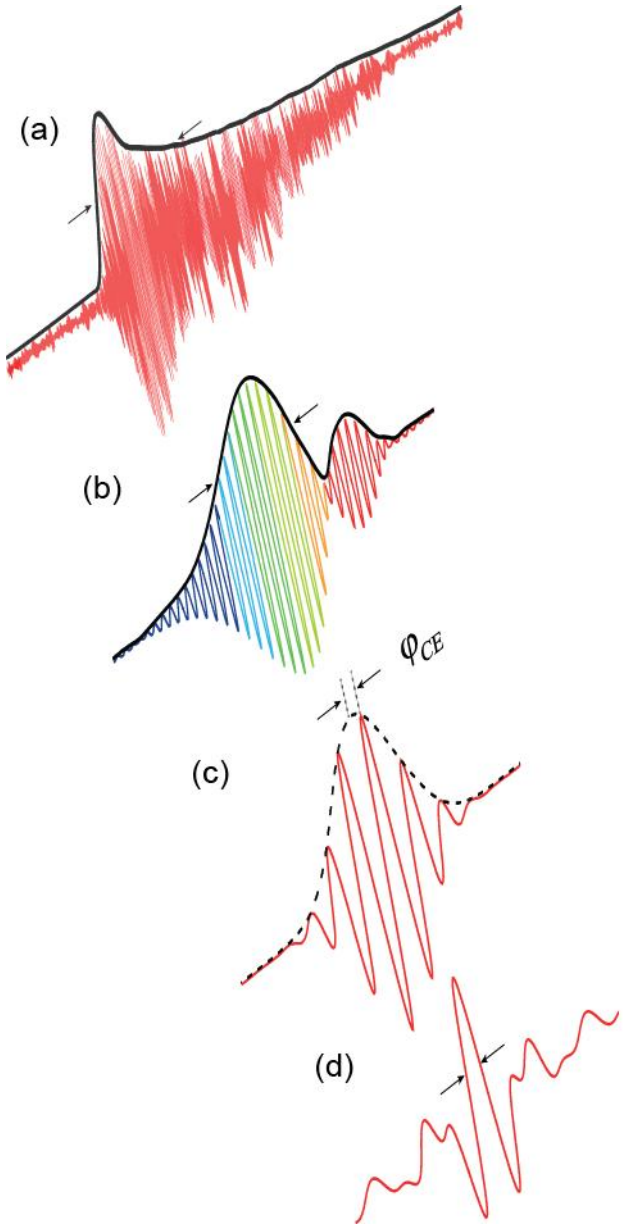

Fig. 1: Stages in the temporal control of light. Arrows denote the dynamical properties under control. (a) Confinement of light to incoherent flashes. (b) Femtosecond pulse shaping: control of cycle-integrated quantities of a light waveform (c) Carrier envelope phase control of few-cycle pulses (d) Sub-femtosecond tailoring of light fields (illustration is taken from [70]).

Shaped pulses have been of fundamental importance for the practical implementation of quantum control of matter [10, 11]: the exploitation of interference phenomena in the time and the frequency domains, in order to guide the evolution of vibrational and rotational wavepackets in complex molecular systems and to steer chemical reactions to predefined paths or products [12-14].
A finer level of field control can be achieved by control of the carrier-envelope phase ϕ_{CE} [15-20] (Fig. 1 (c)). The CEP-controlled few-cycle pulses in the terawatt power scale [21] paves the way to driving electronic processes with the field of light. This ability of light field control has had great achievements in attosecond science throughout its first decade [22]. These advances include the generation and measurement of EUV attosecond pulses [8, 21, 23], direct characterization of light fields [24], direct tracing of inner [7] and valence shell electronic wavepackets [9], ionization dynamics of atoms [25], electron dynamics in molecular processes [26, 27], and electron transport in solids [28].

Few cycle pulses and the precise adjustment of the carrier-envelope phase offset offer an effective, but still limited control knob for controlling the inner workings of the microcosm. Moreover, implementation of CEP control relies on independent pulse compression strategies which, so far, work effectively for pulses with spectra spanning less than an optical octave. This imposes considerable limitations on the capability of controlling the field evolution of a pulse with subcycle, or even attosecond, precision as the latter requires control over superoctave light sources with pulse-to-pulse reproducible waveforms.

Previously, important results towards superoctave field synthesis could be attained only via the technique of molecular modulations [29-34]. This approach has recently permitted the subcycle shaping of optical fields via the superposition of quasi-monochromatic waves in the infrared and visible ranges [35] and will be briefly discussed in the next introductory chapter.

Although these periodic waveforms are particularly important for advancing electronics to PHz frequencies, time-domain access to electronic phenomena calls for the temporal confinement of the sculpted waveform to a single cycle or just a few oscillation cycles.

The ultimate control of classical light is the direct tailoring of its instantaneous field vector through the precise sculpting and measurement (briefly: the synthesis) of its subcycle and subfemtosecond temporal profile (Fig. 1 (d)).

The principal objective of the research in this thesis is to synthesise subcycle and attosecond light field transients spectrally spanning over 1.5 to ~2 octaves, from the deep ultraviolet (DUV) to near infrared (NIR), and to harness attosecond science by their unique properties. Moreover, the efforts of this work are motivated by the desire to trigger, manipulate, and drive the evolution of attosecond/few-femtosecond electron dynamics on the nanometre scale [36]. In order to attain this fine degree of light control, the waveforms must be tailored with subcycle precision. On the other hand, for this resolution to be effective in experiments, the light pulses must feature the same field waveform (to attosecond precision) from pulse to pulse.
To reach these objectives, the development of the unique tool, light field synthesizer, has been done including all the technological developments required to reproducibility generate, sampling and synthesise these light transients, as published in [P1] and [P2].

The structure of this thesis work is as follows:

Chapter 1 gives an introduction to the mathematical description of electromagnetic fields, which are essential for a better understanding of light field synthesis, as well as the essential ingredients for the implementation of light field synthesis, including coherent wideband light sources and characterization techniques.

Chapter 2 presents basic elements of strong field physics and the generation of isolated EUV attosecond pulses.

Chapter 3 offers a brief introduction to the operation and properties of the front-end laser system.

Chapter 4 discusses in detail the technology of the central apparatus of this work – the light field synthesizer–. This chapter also covers the generation of the coherent super-octave light sources used in the experiments and presents details of alignment and metrology techniques that afford systematic characterization of the properties of the synthesized pulses, as well as passive and active interferometric stabilization schemes.

Chapter 5 deals with attosecond metrology apparatus that enables the complete characterization of the generated light transients based on the streaking technique [8, 24]. In the second part, it discusses attosecond sampling, design and control of the synthesized waveforms. Subcycle light transients generation and sampling are demonstrated here.

Chapter 6 shows the extension of the light field synthesizer to its second generation, that is, its extension to control 2-octave coherent light and to generate the world's first "optical attosecond transient".

Chapter 7 presents a first application of synthesized subcycle light transient in triggering and probing the subfemtosecond field ionization of Kr atom. The effects of utilizing the subcycle transient in the coherent of the valance electron in Kr^+ ion are discussed. Moreover, the preliminary application of the attosecond light transient in attosecond-bound electron control is demonstrated.

This thesis concludes with an outline of current and future implications of the synthesized attosecond light transients in ultrafast optics and technology in *Chapter 8*.

List of publications within the framework of this thesis:

[P1] M. Th. Hassan, et.al, Attosecond light transients, in preparation

[P2] M. Th. Hassan, A. Wirth, I. Grguras, A. Moulet, T. T. Luu, J. Gagnon, V. Pervak, and E. Goulielmakis, Invited Article: Attosecond photonics: Synthesis and control of light transients. Rev. Sci. Instrum. 83, 111301 (2012).

[P3] A. Wirth, M. Th. Hassan, I. Grguras, J. Gagnon, A. Moulet, T.T. Luu, S. Pabst, R. Santra, Z. Alahmed, A.M. Azzeer, V.S. Yakovlev, V. Pervak, F. Krausz and E. Goulielmakis, Synthesized of light transients, Science, 2011. 334(6053): p. 195-200.

Oral conference contributions of the author

[C1] M. Th. Hassan, et.al, Synthesis and Applications of Subcycle Light Transients, UP 2012, July, 2012, Lausanne, Switzerland.

[C2] M. Th. Hassan, et.al, Sub-optical-cycle waveform light synthesis, CLEO11, May 201, Munich, Germany.

[C3] M. Th. Hassan, et.al, Sub-optical-cycle waveform light synthesis, ATTOFEL Network Meeting, Feb 2011, Berlin, Germany

[C4] M. Th. Hassan, et.al , Attosecond light field synthesis, MCP-AS Workshop, July 2012, Munich, Germany (invited)

[C5] M. Th. Hassan, et.al, Sub-optical-cycle waveform light synthesis, SIECPC Conference, April 2011, Riyadh, Saudi Arabia (invited)

Chapter 1

Light field control

This chapter introduces the basic definitions of pulsed light waveforms and some of the most important concepts that have been explored in ultrafast science in order to control the waveform of light.

1.1 Mathematical description of ultrashort laser pulses

The electromagnetic field $E(t)$ of a pulsed waveform of light can be described by:

$$E(t) = A(t)e^{i[\omega_0 t - \phi(t)]} \qquad (1)$$

where $A(t)$ is a function known as the envelope of the field waveform, Figure 1-1 (a), ω_0 is the carrier frequency, and $\phi(t)$ is the temporal phase of the oscillating field. The connection between the field waveform and its spectrum is possible through the Fourier transform which can be expressed as:

$$E(t) = \frac{1}{2\pi}\int_{-\infty}^{\infty} \tilde{E}(\omega)\,\mathrm{e}^{(i\omega t)}\,d\omega, \qquad (2)$$

where E(t) is the complex electric field in the time domain. Alternatively, we can write:

$$\tilde{E}(\omega) = \int_{-\infty}^{\infty} E(t)\,\mathrm{e}^{-(i\omega t)}\,dt. \qquad (3)$$

Moreover, $\tilde{E}(\omega)$ can also be described by the spectral amplitude $\tilde{A}(\omega)$ and the spectral phase $\varphi(\omega)$ as:

$$\tilde{E}(\omega) = \tilde{A}(\omega)\, e^{i\varphi(\omega)} \qquad (4)$$

Equation 4 implies that control of the light field can be attained through $A(\omega)$ and or $\varphi(\omega)$. For waveforms confined spectrally over a central frequency ω_0 the phase can be also expressed through the Taylor expansion as:

$$\varphi(\omega) = \varphi_0 + (\omega-\omega_0)\varphi_1 + \frac{1}{2}(\omega-\omega_0)^2\varphi_2 + \frac{1}{6}(\omega-\omega_0)^3\varphi_3 + ... \qquad (5)$$

where $$\varphi_1 = \left.\frac{d\varphi}{d\omega}\right|_{\omega-\omega_0}, \ \varphi_2 = \left.\frac{d^2\varphi}{d\omega^2}\right|_{\omega-\omega_0}, ...$$

The zero-order phase (φ_0) is known as the absolute phase. For the electric field of a few cycle pulse which can be expressed as $E_L(t) = A_L(t)\cos(\omega_L(t)t + \phi_0)$ where, $A_L(t)$ is the pulse envelope, ω_L is the frequency of field oscillation, the absolute phase can be described as the relative phase of the carrier wave with respect to the envelope (carrier envelope phase ϕ_{CE}), as shown in Figure 1-1(a).

While the first-order phase (φ_1) is responsible for a linear translation of the waveform in time, also known as the group delay (GD).

The second-order phase (φ_2) also known as the linear chirp, is responsible for a linear variation of the instantaneous frequency as a function of time. Figure 1-1(c) and (e) show examples of a positively and negatively chirped pulse, respectively. Higher orders of the phase, such as the third order, can also have an important impact on the shape of a pulsed light waveform as shown in Figure 1-1(b).

As light waveforms propagate in materials both $A(\omega)$ and $\varphi(\omega)$ are being affected. The first generation of light control techniques and methods focused on discovering ways that could enable control on the most essential of terms in the Taylor expansion of equation (5), such as the linear chirp (GDD).

Although positive linear and higher order chirps can simply be introduced by propagation of light in ordinary materials, a key step has been taken by the invention of techniques that can introduce negative chirp on the temporal profile of a light waveform.

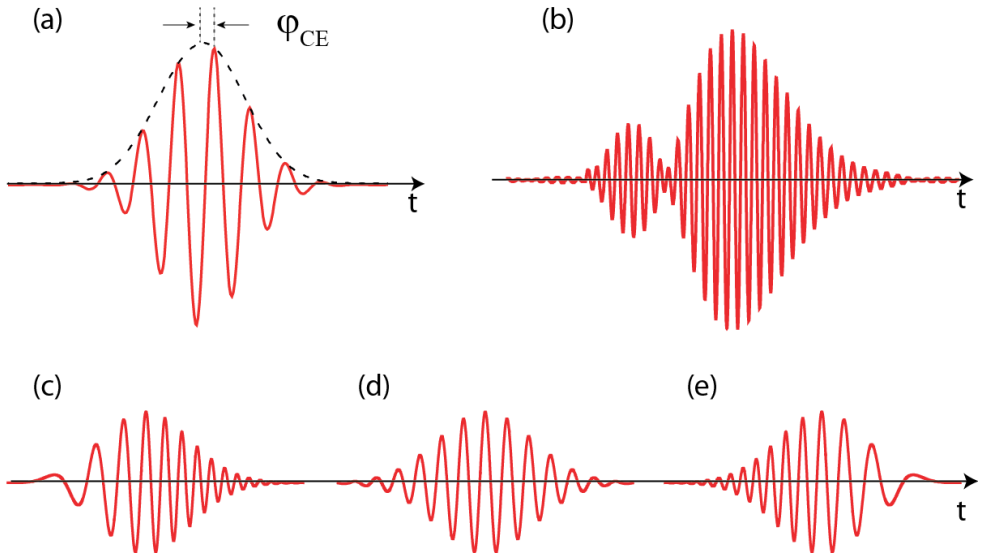

Figure 1-1: Effects of the various orders of the phase on the waveform of a light pulse (a) The Carrier Envelope Phase (CEP) shift— the envelope is shown in dashed black line. (b) Third order phase on simulated 10fs lase pulse at a central wavelength 800nm. The effect of the second-order phase (linear chirp) on a simulated ~5 fs laser pulse with a central wavelength (800nm) is shown from (c-e) (c) Positively chirped pulse. (d) Chirped-free pulse and (e) negative chirped pulse.

This has been demonstrated by Treacy (1969) [37] by the utilization of a parallel pair of identical diffraction gratings in an arrangement shown in Figure 1-2 (a). Later on, the idea was extended to utilizing prisms. The Brewster-angled prism pairs, as shown in Figure 1-2(b), were the first demonstrated low-loss sources of negative GDD [38, 39]. In both cases, negative GDD is accompanied by significant amounts of intrinsic high-order dispersion, which cannot be compensated. Another drawback of these light waveform control techniques is their limitation in controlling the dispersion over a broadband spectrum. The invention of Chirp mirror (CMs) by Krausz and coworkers [40], is among the most prominent technologies for broadband dispersion control and has enabled the compression of pulses down to the few cycle regime[40, 41]. The design of these mirrors relies on a multilayer structure with a gradual change in the optical thickness of dielectric layers across the structure, resulting in a wavelength-dependent penetration depth of the incident radiation.

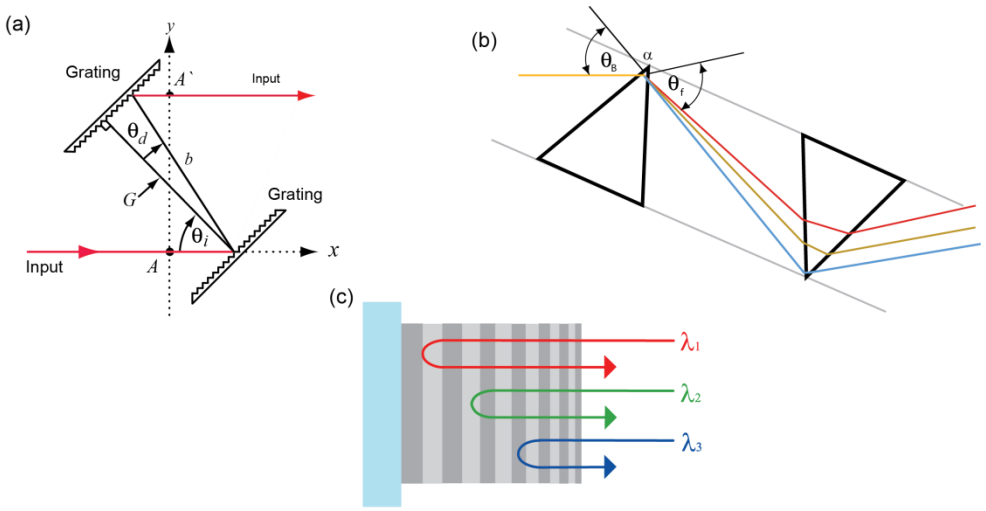

Figure 1-2: Dispersion control. (a) A pair of parallel grating dispersion compressor. (b) Prism compressor for dispersion control (c) The basic principle of the dispersive (chirped) mirror, (b), (c). (illustrations are adapted from [42,48]).

The GDD is controlled by setting up the sequence of layer such as the penetration depth of each wavelength of the waveform in the multilayer structure can be adjusted. The principle of the chirp mirror dispersion compensation is illustrated in Figure 1-2(c). Some of the key advantages of chirped mirrors are: the ability to compensate for second and higher order phases on demand, although not on a dynamic manner, high reflectivity and ability to control the dispersion over a broad band spectrum. The CM mirror technology have been used in this thesis work for the generation of few-cycle pulses in four different areas of the spectrum, as will be discussed in Chapters 4 and 6.

1.2 Light synthesis principles

The basic idea of light waveform synthesis can be described as follows: First, the spectrum of a light waveform is decomposed into its constituent spectral components by a disperser, then, adequate modulators acting on each of this spectral components individually modifies the relative phase (or delay), the amplitude and polarization of these components before they are coherently superimposed again by a combiner to create a desired tailored waveform (Figure 1-3(a)).

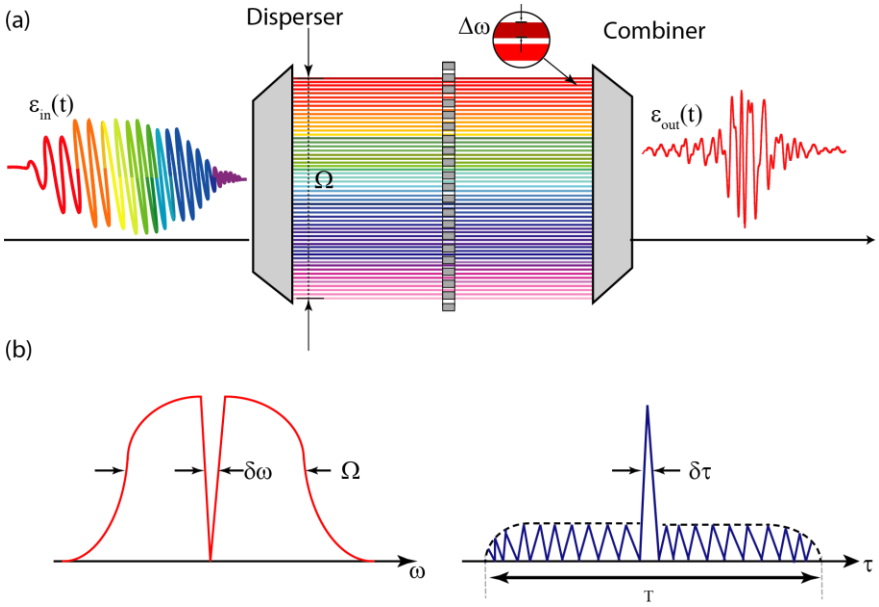

Figure 1-3: (a) the basic principle of light synthesis. (b) The pulse shaping in time and frequency domains (illustration is adapted from [42]).

Although equation (4) implies that any arbitrary field waveform can be composed by applying the above idea, in reality the arbitrariness is sensitive to two key parameters. These are: first, the spectral resolution of the disperser ($\delta\omega$) which defines the temporal window (T) with in which the control can be exerted. Second, the total bandwidth (Ω), this defines the shortest temporal feature ($\delta\tau$) that can be sculpted upon the intensity profile of the pulse which is given by $\delta t = 2\pi/\Omega$, as shown in Figure 1-3(b).

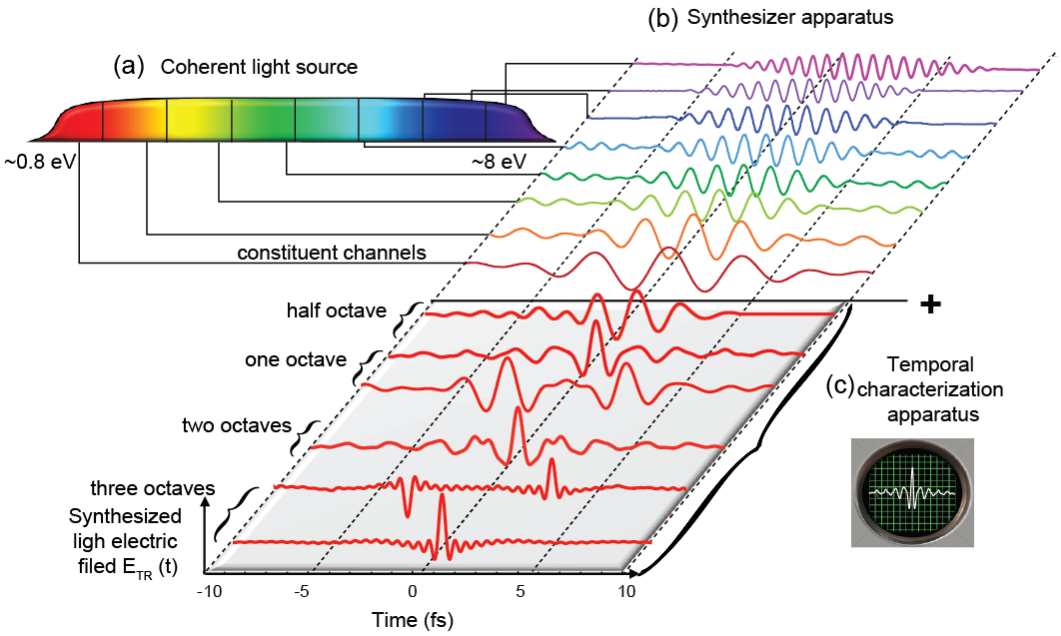

Figure 1-4: Principles of light field synthesis. (a) A light synthesizer is used to decompose a broadband supercontinuum into its constituent spectral bands. Relative phases and intensities for the spectral bands are fully controlled inside the synthesizer. Coherent superimposition of these bands creates a synthesized light waveform at the exit of the synthesizer (b) that can be sampled by an appropriate apparatus (c) (illustration is taken from [70]).

If the total bandwidth is narrower than the central (centroid) frequency at the limit $\Omega << \omega_0$, this resolution is indeed given by $\delta t \sim 2\pi/\Omega$, which corresponds to temporal features encoded on the pulse's envelope over the time window T. In that, case waveform synthesis is practically a control of the cycle integrated properties of the pulse. However, if the total bandwidth is comparable or preferably greater than the central frequency $\Omega \geq \omega_0$, the resolution will be given by $\delta t < 2\pi/\omega_0 = T_0$. This resolution is sufficient for tailoring the subcycle structure of the waveform, nearly as steep as a half-cycle of the field, and its instantaneous intensity. For the optical frequencies, this is implying attosecond resolution in sculpting the waveform which leads to field synthesis.

Figure 1-4 schematically illustrates light field synthesis. The spectral bandwidth spans over considerably more than an optical octave, in order to attain attosecond resolution. For many experiments, where the attosecond resolution is important [21], the required time window T will be on the order of a couple of optical cycles of the driver waveform. That will reduce the required spectral resolution of each band $\tilde{E}_n(\omega)$ down to the level of ~1 eV.

The previous discussion implies three main key elements for the light field synthesis, (a) a coherent light source with band width Ω, where $\Omega \geq \omega_0$, (b) light field synthesizer capable of manipulating this broadband light, and (c) tools for light field characterization. In the next paragraphs we will give a brief introduction of these three key elements.

1.3 Coherent white light sources

Although modern laser systems comprise extremely broadband sources themselves [43], they are typically limited to less than an optical octave around the visible or near infrared part of the spectrum. To generate a broadband spectrum that is spanning over more than an optical octave, nonlinear frequency conversion techniques become essential. One of the pioneering works in this respect is that of Alfano and Shapiro (1970) [44] who reported the first generation of a white light spectrum (or supercontinuum SC) covering the entire visible range from 400 to 700 nm by propagating picoseconds pulse in solid bulk (BK7 glass). These techniques have now extended SC generation to more than two octaves [45]. Due to material damage, the use of solid nonlinear media for SC generation is limited to the nonlinear upcoversion of low energy pulses. Alternative techniques, that are mostly used in strong field and attosecond physics, include pulse broadening in gaseous media, in particular, hollow-core fibers filled with noble gases are suitable for broadening the spectrum of laser pulses with higher energies [46]. The advantage of this technique is that the gases can recover from the ionization when the laser pulses are gone, whereas, damage to a solid by the laser is permanent. The strength of the nonlinearity can be achieved by changing the gas type and

pressure. It is for these reasons that gas-filled hollow-core fibers have been widely used to generate few cycle pulses [47].

In this work, we will demonstrate that this technique can now be extended to support the generation of light that spans over more than two optical octaves including the entire visible, deep ultraviolet, near-infrared. In the hollow core fiber technique, just as in the case of solids, the new spectral components are generated as a result of the self-phase modulation (SPM) of the laser pulse as it propagates in the medium [48], beside an additional nonlinear mechanisms [46, 49].

In that case, the time dependence of the variation of refractive index can be expressed as:

$$n(t) = n_0 + n_2 I(t) \tag{6}$$

A nonlinear phase shift is added to the temporal phase of the pulse, when the material dispersion is neglected, and this can be given by

$$\phi_{nl}(t) = -\frac{2\pi}{\lambda} I(t) n_2 L \tag{7}$$

The time-dependent nonlinear phase leads to a frequency shift

$$\Delta\omega(t) = \frac{d}{dt}\phi_{nl}(t) = -\frac{2\pi}{\lambda} n_2 L \frac{d}{dt} I(t) \tag{8}$$

The up and down frequency shifts introduce new frequency components to the pulses, which broadens the bandwidth.

For Gaussian pulses, in the absence of dispersion, the maximum broadening at the exit of a fiber with length L is given by

$$\delta\omega_{\max} = 0.86\gamma P_0 z_{eff} \frac{1}{\tau} \tag{9}$$

where P_0 is the pulse peak power, τ is the pulse duration, γ is the nonlinear coefficient $\gamma = n_2\omega_0 / cA_{eff}$ and $z_{eff} = (1 - e^{-\alpha L})/\alpha$ where $A_{eff} = \pi\alpha^2$ is the effective mode area, α is the mode radius , ω_0 is the centre frequency of the laser and n_2 is the

refractive index of the gas[50]. The broadening of the pulse depends on many parameters, such as: the temporal profile and the central wavelength of the seeded laser pulse, the length of the fiber and the pressure of the gas inside the fiber chamber.

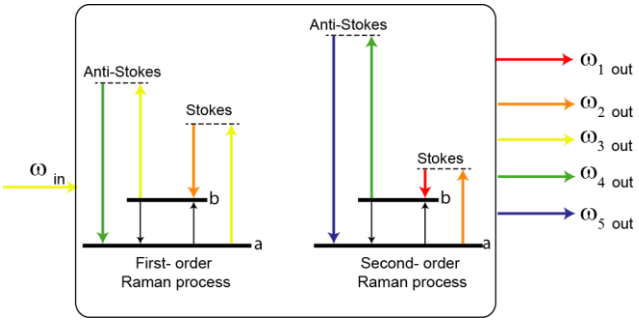

Figure 1-5: The process of cascaded Raman scattering. The input frequency ω_{in} (yellow) triggers the spontaneous emission of stokes and anti- Stokes frequencies (green and orange). These frequencies cause second order Raman scattering to produce new frequencies (blue and red) in cascade Raman scattering process (illustration is taken from [34]).

Another technique for generating superoctave radiation is based on the Raman resonance in molecule modulators, which produce a set of laser frequency modulations which could span multiple octaves [29, 30]. The Raman resonance process can be cascaded in a molecular modulator and a broadband frequency modulation can be generated, as explained schematically in Figure 1-5 [34]. This technique has been used for the successful demonstration of waveform synthesis for light spanning over two octaves[35]. The disadvantage is that the generated spectrum formed by this technique is discrete and this implies also repetitive structures in the time domain which could spoil the resolution in driving or controlling fast processes.

1.4 Pulse shaping and field synthesis techniques

In this section, representative pulse and field shaping techniques will be discussed. The most common arrangement for the pulse shaping is the so called *4f*-line arrangement which was proposed in 1983 by Froehly and co-workers [51]. This arrangement is shown in Figure 1-6. In this technique, the basic idea of Fourier synthesis, discussed earlier, is applied.

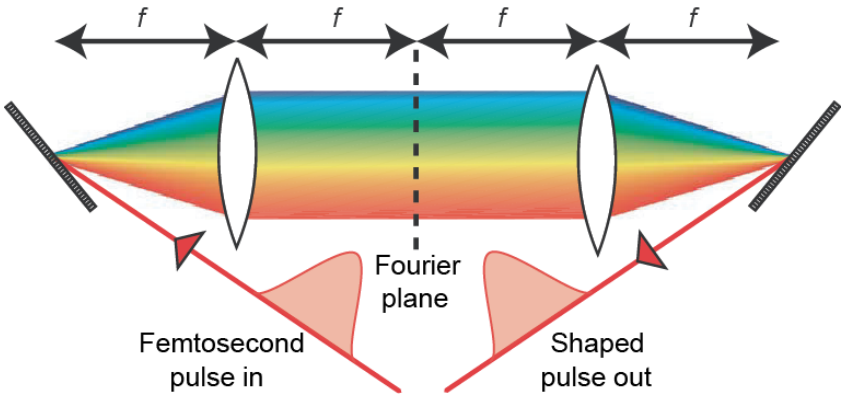

Figure 1-6: Zero dispersion 4*f*-line arrangement set up of pulse shaper (illustration is taken from [52]).

The input pulse is first decomposed into its constituent spectral components by a grating and is being focused by a lens or a curved mirror. Then, a mask introduced at the Fourier plane modulates the phase, amplitude and/or polarization of the dispersing spectral components. After the spectral components are recombined by a second lens and grating, a shaped output pulse can be obtained. An interesting point in the *4f* -pulse shaping arrangement is that, it is ideally free of temporal dispersion [38]; therefore, in the absence of a pulse shaping mask, the output and input pulses are identical [52, 53]. Different kinds of masks can be placed in the Fourier plane of a 4*f* -line to form a pulse shaper, primarily LCD masks [54, 55], an Acousto-optic modulator [56, 57], Micro-Mechanical Deformable Mirror (MMDM) [58], and Micro-Electro-Mechanical Systems (MEMS) [59].

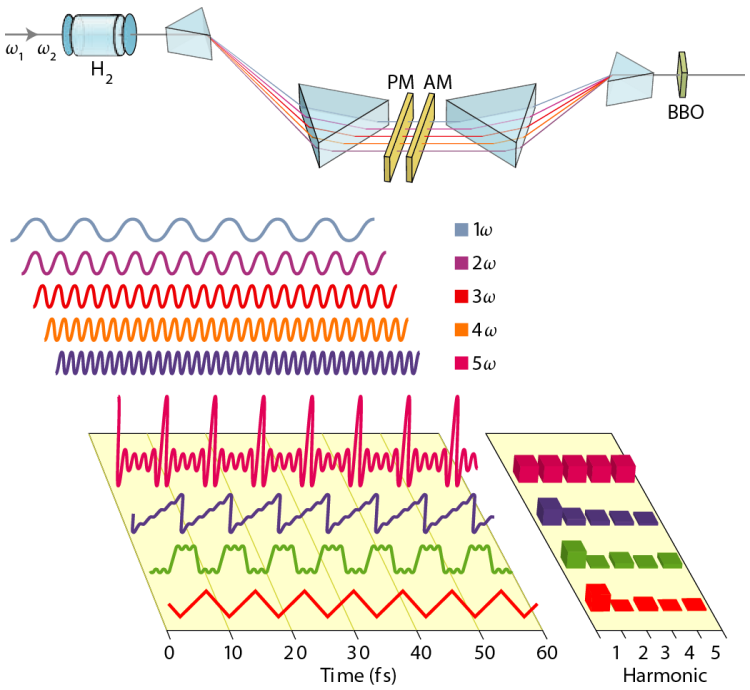

Figure 1-7: (b) Waveform synthesis of harmonics generated in molecular modulator (illustration is taken from [35]).

In combination with the idea of the molecular modulators, discussed earlier, synthesis can be realized by controlling the amplitude and the phase of the generated harmonics [35]. In this technique, the harmonics are generated by illuminating the molecular modulator medium, such as H_2, with the idler and the second harmonic of a nanosecond laser pulse (adiabatic technique). Before the different harmonics superimpose they propagate through two liquid crystal spatial light modulators to control the relative phases and amplitudes of the individual harmonic. By adjusting the relative amplitudes and phases of the superimposed harmonics, a train of synthesized waveforms are generated, such as the square, sawtooth, subcycle sine and cosine, and triangle waveforms, as illustrated in Figure 1-7. The drawbacks of this technique are that the generated synthesized waveforms are in a train which limits the ability to utilize these waveforms in many applications, and the low power of the generated waveform, in regarding the low power of seeded pulse and which is limited by the damage threshold of the phase and amplitude modulators.

1.5 Temporal Characterization Techniques

The accurate characterization of ultrafast laser pulses is, nowadays, an important asset in ultrafast science. Several techniques have been developed to this end. The autocorrelation-based techniques, for example, are one of the most commonly used. Moreover, more sophisticated techniques, such as frequency-resolved optical gating (FROG) [60] or spectral phase interferometry for direct electric field reconstruction (SPIDER) [61], have advanced the field of ultrafast metrology even further, since they have allowed access into the spectral phase of the pulse. In the last decade, attosecond science has made possible yet another essential technique, namely "attosecond streaking". This technique utilizes attosecond extreme ultraviolet pulses as samplers of the instantaneous field waveform of a pulse and is virtually insensitive to the pulse bandwidths. In this chapter, will be given a concise description of these techniques, especially due to the fact that they are critical for the work presented in this thesis

1.5.1 Intensity autocorrelation

In this technique, the autocorrelation occurs between the pulse under characterization and its replica. However, this does not provide any new information, unless there is a nonlinear interaction, for instance, second harmonic generation. In this case:

$$E_{sig}^{SHG}(t,\tau) \alpha E(t) E(t-\tau), \tag{10}$$

where τ is the delay. This produced field has an intensity that is proportional to the intensity of the two input pulses $I(t)$ and $I(t-\tau)$:

$$I_{sig}^{SHG}(t,\tau) \alpha I(t) I(t-\tau), \tag{11}$$

By time integration

$$A^2(\tau) = \int_{-\infty}^{\infty} I(t) I(t-\tau)\, dt, \tag{12}$$

Where $A^2(\tau)$ is the intensity autocorrelation,

$$\tilde{A}^2(\omega) = \left|\tilde{I}(\omega)\right|^2 \qquad (13)$$

where $\tilde{I}(\omega)$ is the Fourier Transform of $I(t)$. The measurement is based on recording the time-average of the second-harmonic power as a function of the relative delay τ between two identical replicas of the input pulse. The peak in second-harmonic power which is plotted as a function of τ contains information about the pulse width [62].

1.5.2 Frequency-resolved optical gating (FROG)

In Frequency resolved optical gating (FROG), the ultrashort pulse gates itself [63], the spectrogram of the pulse is measured by spectrally resolving the gated piece of the pulse in time domain [64]. Mathematically [65, 66] this can be described as,

$$S(\omega,\tau) = \left|\int_{-\infty}^{\infty} E(t)g(t-\tau)\exp(-i\omega t)dt\right|^2. \qquad (14)$$

where $S(\omega,\tau)$ is the pulse spectrum, $g(t-\tau)$ is the delayed gate function, τ is the delay and $E(t)$ is the electric field of the measured pulse. The spectrogram is a collection of spectra of all gated $E(t)$ at the different delay points. We can extract $E(t)$ from the measured spectrogram by different FROG analysis algorithms [67]. The FROG trace is described by

$$I_{FROG}(\omega,\tau) = \left|\int_{-\infty}^{\infty} E_{sig}(t,\tau)\exp(-i\omega t)dt\right|^2. \qquad (15)$$

where $E_{sig}(t,\tau)$ is the autocorrelation signal, which can be used to determine $E(t)$, since;

$$E(t) = \int_{-\infty}^{\infty} E_{sig}(t,\tau)\,dt. \qquad (16)$$

Where $E_{sig}(t,\tau) \propto E(t)E(t-\tau)$ in case of the second harmonic generation (SHG) FROG.

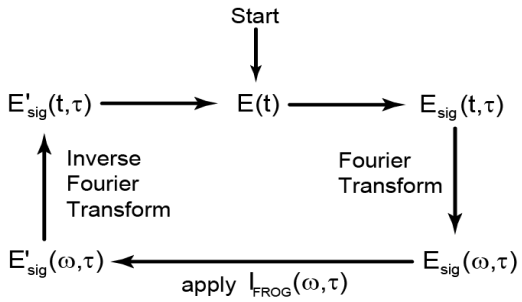

Figure 1-8: Schematic diagram of Fourier-transform algorithm for retrieving the intensity and phase from FROG trace (Illustration is adapted from [68]).

The retrieval algorithm strategy for retrieving the intensity and the phase from the FROG trace is shown in the diagram in Figure 1-8. The FROG technique has different beam geometries such as; polarization gating (PG), self-diffraction (SD), second harmonic (SH), third harmonic (TH) and transient grating (TG) FROG [68].

1.5.3 Transient-grating FROG

TG-FROG geometry arrangement, schematically illustrated in Figure 1-9, has three-beam geometry, where the measured pulse splits into three replicas. The three beams propagate in a so-called BOXCARS arrangement [69], and they are overlapped spatially and temporally in a nonlinear medium, where two of the beams produce a refractive index grating and the third is diffracted by the induced grating.

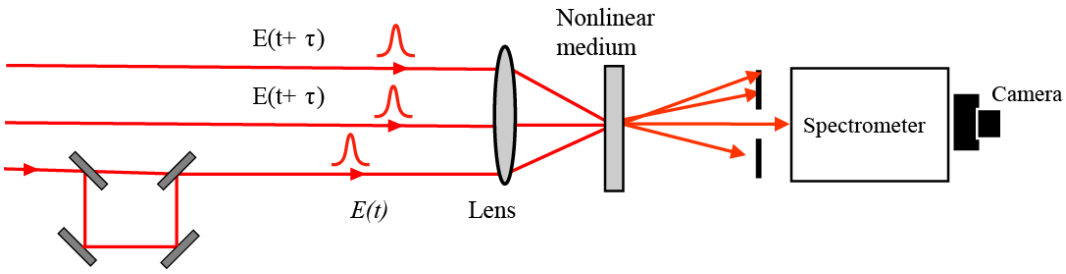

Figure 1-9: Transient grating (TG-FROG) geometry (illustration is adapted from [68]).

The nonlinear signal appears on the fourth corner of the rectangle, where the three input beams in the three outer corners are the only ones that are perfectly phase-matched. This is known as the TG-FROG signal; delaying one of the three input beams and spectrally resolving the resultant signal in a FROG-trace.
The signal pulse is given by

$$I_{FROG}^{TG3}(\omega,\tau)=\left|\int_{-\infty}^{\infty}E_1(t)\,E_2^{*}(t-\tau)E_3(t)\exp(-i\omega t)dt\right|^2. \qquad (17)$$

and since all the three pulses are identical, hence, it becomes

$$I_{FROG}^{TG3}(\omega,\tau)=\left|\int_{-\infty}^{\infty}|E(t)|^2\,E(t-\tau)\exp(-i\omega t)dt\right|^2. \qquad (18)$$

This TG-FROG geometry has been used to characterize the short pulses in this work. The key advantages of the TG-FROG geometry are; phase matching, almost background free, and can be used for measuring pulses in different spectral regions (i.e. NIR-Visible and UV) [70, 71].

1.5.4 Attosecond metrology: sampling of the XUV attosecond pulse and the optical field

Previously, described characterization techniques of the ultrashort femtosecond pulses have profound limitations. Pulses extending over more than an optical octave cannot be reliably characterized. Additionally, these techniques do not give access to the instantaneous electric field, which is essential in field synthesis. For that, the attosecond streaking [24] has been opted for sampling both the XUV and the optical field in this thesis work.

Attosecond streaking

The attosecond streak camera has been proposed in ref [72]. It is based on the following concept: An EUV pulse ionizes rare gas atoms and a bunch of photoelectrons (wavepacket) which mimics the temporal structure of the attosecond wavepacket are generated [73].

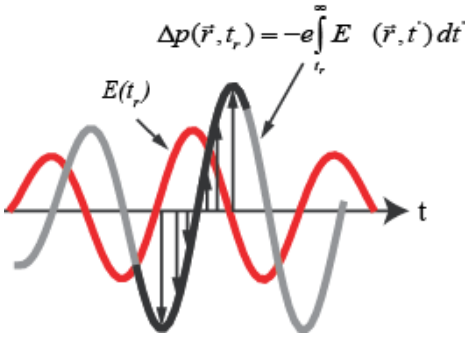

Figure 1-10: The concept of attosecond streaking light field sampling (illustration is taken from [70]).

The momentum of electrons (Figure 1-10) released in the field $E(\vec{r},t_r)$ at time t_r will undergo shifts $\Delta p\ (\vec{r},t_r)$ which are given by

$$\Delta p(\vec{r},t_r) = -e\int_{t_r}^{\infty} E(\vec{r},t')\,dt' \qquad (19)$$

The relation between the momentum shift and the vector potential $A(\vec{r},t)$ of the field $E(\vec{r},t_r)$ is

$$\Delta p(\vec{r},t) = -e\,A(\vec{r},t) \qquad (20)$$

Measuring the modulation of the electron spectra as a function of the time delay between the EUV pulse and the laser field provides all the information in order to retrieve both temporal profiles of EUV and laser pulses. This is better illustrated in Figure 1-11(i) and Figure 1-12. The first case, where the electron bunch is generated with Fourier limit EUV pulse as illustrated in Figure 1-11. If the electron bunch is synchronized with a zero transition of the vector potential, the corresponding final momentum distribution is broader (blue profile) as compared to the spectrum of the free field electron bunch distribution (magenta), as shown in Figure 1-11(ii). However, if the electron bunch is probed at the consecutive zero transition (shifted by π), as shown in Figure 1-11 (i), the broadening (violet profile) is identical to the free field electron bunch distribution (magenta).

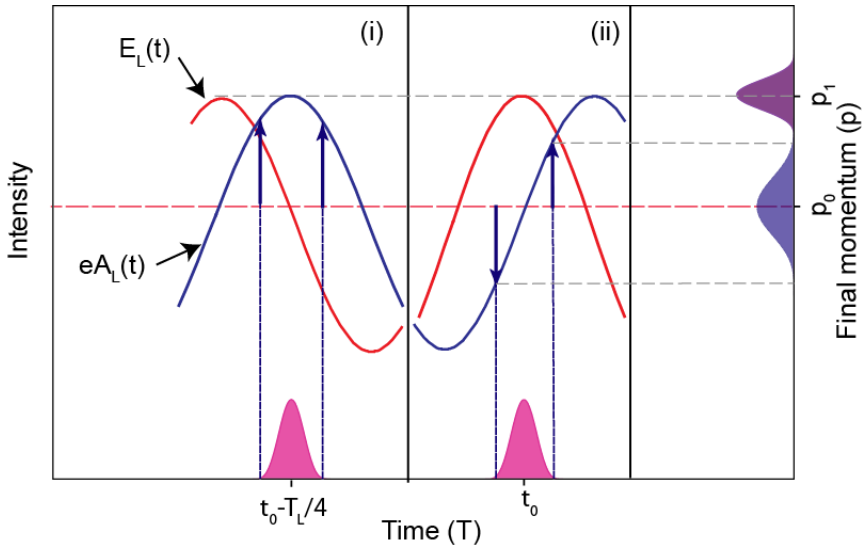

Figure 1-11: Attosecond streak camera principle. An electron bunch with an initial momentum distribution (magenta profile) is probed around the maximum of the electric field of a laser pulse (red line). The momentum transfer to the photoelectrons (given by the vector potential (blue line) results in symmetrically broadened final momentum distributions (blue profile), when probed at adjacent, zero transitions of the vector potential as shown in (ii) . However, in (i) the electron bunch is probed by a laser pulse around a zero-crossing of its field oscillation (red line), the electron bunch suffers a shift to higher energies and a slight broadening due to the curvature of the vector potential (blue line) (illustration is adapted from [22]).

The second case is illustrated in Figure 1-12 where a linearly chirped EUV pulse is employed to generate an electron bunch. In this case photoelectrons with different energies are localized at the two ends of the bunch. Figure 1-12 shows the influence of this chirp on the resulting momentum distribution when probed at adjacent zero crossings of the vector potential for the two most extreme cases. If the slope is parallel to the chirp (Figure 1-12 (i)), the vector potential leads to a broadening of the electron momentum distribution (blue profile). In the opposite case, shown in Figure 1-12(ii), the slope of the vector potential counteracts the chirp of the electron bunch and compresses the momentum distribution. The shift in central energy and the deformation of the spectra are clearly visible (violet profile). A series of electron spectra recorded as a function of the delay between the electric field and the attosecond pulse are referred to as a "streaking spectrogram" [5, 7, 8, 72]. The spectrogram can be reconstructed, based on reconstruction algorithms originally developed for FROG [63].

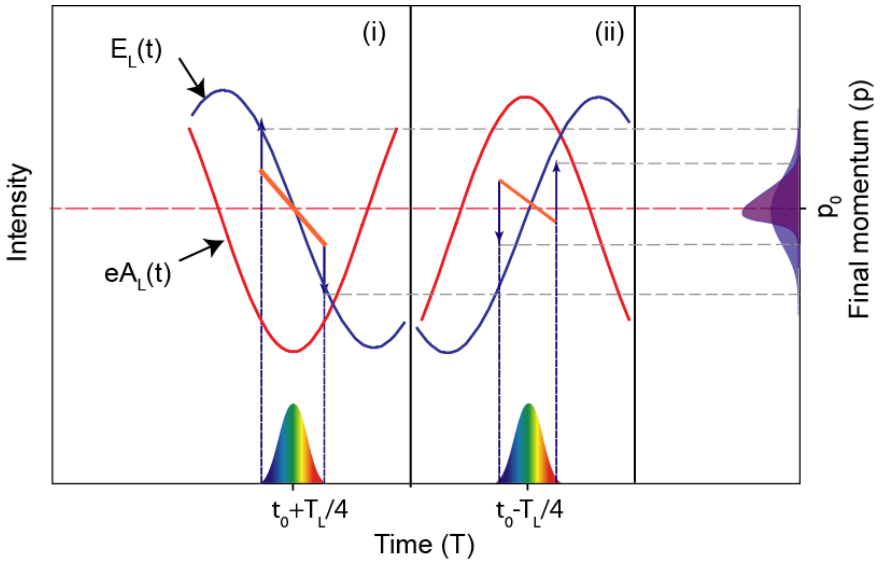

Figure 1-12: Attosecond streak camera principle in the case of chirped attosecond EUV pulse generated electron replica which carries this information as chirp of its momentum distribution. The figure shows the influence of this chirp on the resulting momentum distribution for the two most extreme cases. (i) The emission is around a laser field oscillation with slope parallel to the chirp, the vector potential leads to a broadening of the electron momentum distribution. (ii) The opposite case, the slope of the vector potential compresses the momentum distribution which suffers from central energy shift (illustration is adapted from [22].

Typically, these methods reconstruct the spectrogram based on a numerical algorithm, offering access to both the pulse and the gate. In this work, we have explored (ATTOGRAM) [75] in order to reconstruct the temporal dynamics of our attosecond pulses.

Retrieving of the light fields can be performed by a simplified [76, 77], considerably faster (seconds), and equally accurate retrieval method, but is less noise-sensitive, than the complex method based on FROG-type reconstruction algorithms. This method is based on the evaluation of the first moments (centroids) of the streaked photoelectron spectra as a function of the time delay between the EUV pulse and synthesized transient fields. The basic assumption is that the attosecond pulse must be shorter than a half-cycle of the highest frequency of light transient, which is accurate down to wavelengths of ~120nm.

First, the attosecond EUV pulse ionizes the gas atom with ionization energy W can be modelled as:

$$E_{EUV}(t) = \left|E_{EUV}(t)\right| \exp\left[i\left(\omega_{EUV} t + \varphi(t)\right)\right]. \qquad (21)$$

where ω_{EUV} is the central EUV frequency and $\varphi(t)$ contains higher-order temporal phase variations (chirp). Photoelectron trajectories are launched in a continuum by a laser field at various moments *t*.

These trajectories end at the detector with a final kinetic energy $E_K(t)$, which is given in atomic units ($\hbar = a_0 = 4\pi\varepsilon_0 = m_e = 1$) by,

$$E_K(t) = \left(\sqrt{E_0 + \dot{\varphi}(t)} - \frac{1}{\sqrt{2}} A_{TR}(t) \right)^2 \approx E_0 - p_0 A_{TR}(t) + \frac{1}{2} A_{TR}^2(t) + \left(1 - \frac{A_{TR}(t)}{p_0}\right)\dot{\varphi}(t). \qquad (22)$$

with $p_0 = \sqrt{2E_0}$, and $E_0 = \omega_{EUV} - W$, where $A_{TR}(t)$ is the vector potential and W is the ionization energy. Since the variations in the attosecond pulse's instantaneous frequency, represented by $\dot{\varphi}(t)$, are small compared to its central frequency ω_{EUV}, the final term on the furthest right-hand side of the pervious equation is negligible. This implies that the center of the streaked photoelectron spectrum is insensitive to the phase of the attosecond pulse.

Moreover, if the attosecond pulse is shorter than a half-cycle of the laser field, the central energy E_S of the streaked photoelectron spectrum is well approximated by $E_S \approx E_K(t_r)$, where t_r is the central time of the attosecond pulse, *i.e.* the release time of the electron. This allows for a direct evaluation of the vector potential $A_{TR}(t)$ which, in turn, yields the complete time dependence of the synthesized waveform's electric field

$$E_{TR}(t) = -\partial_t A_{TR}(t). \qquad (23)$$

The light transients characterized by this method agree with those of the detailed FROG analysis of the streaking spectrogram. Details on the numerical implementation of the algorithm has been done by Justin Gagnon are given in Appendix I.

Chapter 2

Strong field physics

The development of high intensity laser pulses with fields comparable or in excess of the Columbic binding field in atoms or molecules gives the opportunity to explore a new dynamic area of light mater interaction—strong field interactions—and, particularly, the ionization of materials in the presence of a light field. As ionization will be an important platform in this thesis, in order to demonstrate the capabilities of synthesized light transients, a brief introduction will be given to the physics of the interaction of the strong fields with atoms, including the generation of attosecond pulses [78, 79].

2.1 Multi-Photon Ionization

Multi-Photon Ionization (MPI) is a highly nonlinear process; it takes place when the atom absorbs a number of photons to release one or more electrons. For valence electrons the multi-photon transition occurs from a bound state to a continuum state[80]. This ionization process can be described by perturbation theory. The n-photon ionization rate is be given by

$$\Gamma_n = \sigma_n I^n \qquad (24)$$

where n is the number of photons required for the ionization process, σ_n is the ionization cross section, and I is the intensity of the laser. In the multi-photon ionization, the scaling-up of the intensity is limited by the reaching of saturation in which all the atoms have been ionized and no more ionization occurs.

In the process of multi-photon ionization, if the excited electron is still under the influence of the atomic potential, and absorbs more photons than those needed for photon ionization (n+s), this is called the **Above-threshold ionization (ATI)** (illustrated in Figure 2-1(a))**.** In this case, non-perturbation theory is applied[80, 81]. Ionization rate can be given by:

$$\Gamma_{n+s} \propto I^{n+s} \tag{25}$$

where s is the number of excess photons absorbed, the invention of the high resolution time-of-flight spectrometer gives the possibility to measure the photoelectron spectra at higher energy. Lompré *et al.* (1985) and Xiong *et al.* (1988) observe that at high energy many photoelectrons peaks disappear, which consider as indicator for breakdown of perturbation approach at this regime.

2.2 Tunnelling ionization

Tunnelling ionization is another essential mechanism of ionization which occurs under certain conditions as realized by Keldysh in 1965 [80, 82]. If the laser field is strong and the carrier frequency of this field is low enough, the atomic potential is distorted such that the potential barrier is formed and the electron tunnels, as illustrated in Figure 2-1(b). Keldysh identified a parameter known as γ which is given by:

$$\gamma = \frac{\omega_L \sqrt{2m_e I_p}}{eE_0} = \sqrt{\frac{I_p}{2U_p}} \tag{26}$$

where γ the adiabaticity parameter is the ratio between the laser field frequency and the tunnelling frequency, ω_L and E_0 are the angular frequency and the electric field strength of the laser field, m_e and e are the mass and charge of the electron and, I_p is the ionization potential of the system.

For $\gamma \succ 1$, multi-photon ionization is the dominant process, and if $\gamma \prec\prec 1$, tunnel ionization is more important. Increasing the low frequency field strength makes the interaction stronger, which may lead to a decrease of the potential barrier until the ground state is no longer bound and the wavepacket is not affected by the Coulomb atomic potential, this is called over-the-barrier-ionization (OTBI) (Figure 2-1(c)). The intensity required to trigger the over-the-barrier-ionization is called critical intensity I_{OTBI}, and can be given by

$$I_{OTBI} = \frac{\pi^2 c \varepsilon^3 I_p^4}{2Z^2 e^6} (W\, cm^{-2}) \qquad (27)$$

where Z is the charge state of the atom or ion of the system. For instance, the (OTBI) occurs in neutral Krypton atom at intensities exceeding $\sim 1.3 x 10^{14} W/cm^2$ but for the natural Xenon atom it happens at $\sim 8.6 x 10^{13} W/cm^2$.

Tunnelling ionization has been treated quantum mechanically in [83], and it has been investigated and verified experimentally in [84, 85]. The tunnelling ionization rate can be given by

$$\Gamma = N \cdot \exp\left(-\frac{4\sqrt{2m_e} I_p^{3/2}}{3\hbar e E_0} \right) \qquad (28)$$

where N is the varying function that depends on the cycle average field intensity, and I_p is the ionization potential. However, the ADK-theory is not applicable in the case of few-cycle NIR laser pulses, since the envelope changes considerably on a subcycle time scale and, therefore, the adiabaticity parameter undergoes changes too. For the subcycle ionization, the rate in the intermediate range of γ has been driven in simple expression in [86]. In this case, the adiabaticity parameter $\gamma(t)$ depends on the envelope function $f(t)$. More details are given in [86]. In this intermediate range of γ, the multi-photon ionization cannot be ignored, however, the tunnelling ionization is dominated.

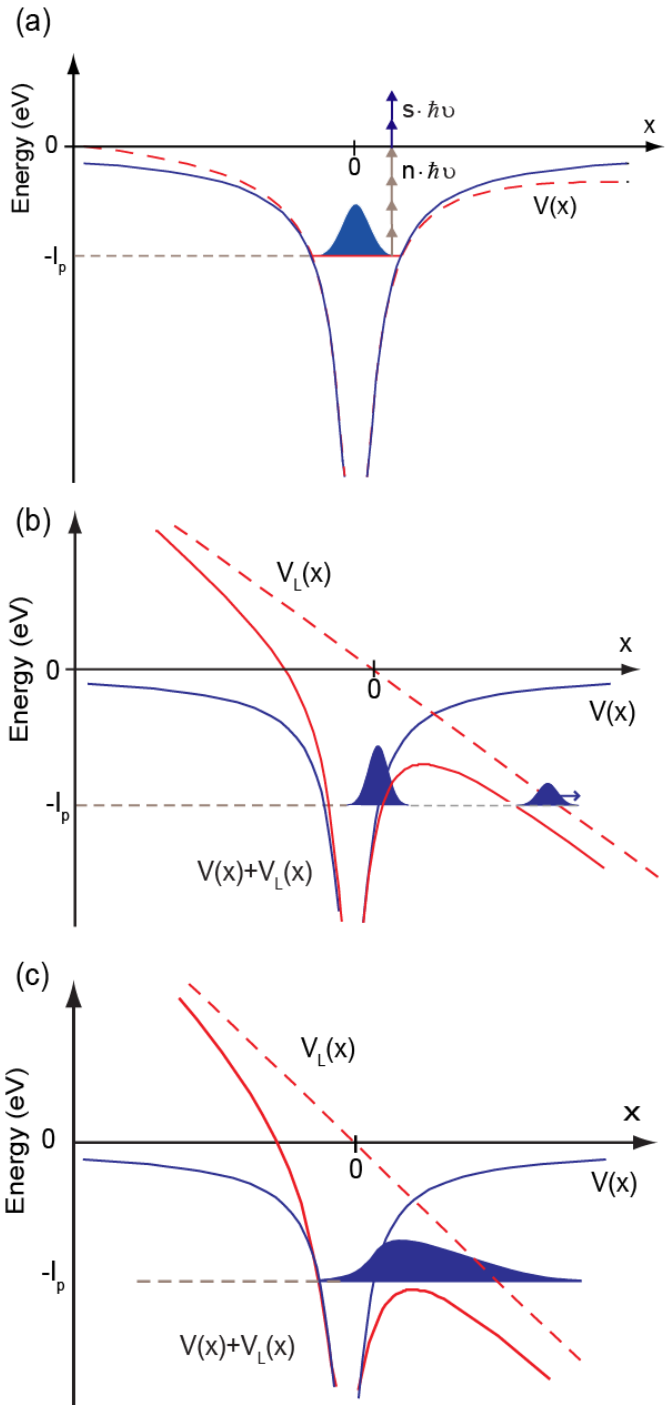

Figure 2-1: The mechanisms of intense field photoionization (a) Multi-photon ionization (absorbed (n) number of photons) and above threshold ionization (absorbed (n+s) photons). (b) Strong field interaction, and the atomic potential is distorted, tunnelling ionization occurs. Increasing the laser intensity even more, the initial wavepacket is free to escape from the atomic potential; this is barrier suppression ionization (c) (illustration is adapted from [114]).

2.3 Isolated attosecond EUV pulse generation

EUV radiation is emitted when intense pulses interact with atoms. High harmonic generation is used to describe the emitted radiation; as in the first experiments, this radiation emerged in form of comb frequencies at a multiple of the frequency of the driver field.

A generic HHG spectrum is illustrated in Figure 2-2, and has a generic shape which contains three regions, the region of the low-order harmonics, the generation of which can be described well on the basis of perturbation theory. They are followed by the plateau-harmonics, where the harmonics intensity is nearly independent of the harmonic order, and a final region - the cut-off - which contains the highest generated harmonics. The highest harmonic (cut-off) is numerically calculated in [87], and it is given by

$$E_{cut-off} \approx I_P + 3.17U_P \qquad (29)$$

where I_P is the ionization potential of the atoms in interactions with strong field and $U_p = eE_0^2 / m_0\omega_0^2$ is the ponderomotive energy which defines as to the cycle averaged quiver energy of a free electron in an electric field. The cut-off can be increased by using longer wavelength and higher intensity laser for the driver lasers. Only the odd harmonics of the fundamental frequency have been observed, because of the dipole selection rules and the symmetry of the atomic potential.

The HHG process mechanism has been explained semi-classically by a three-step-model [88], as illustrated in Figure 2-3, and can be summarized as follows;

Ionization, the high intense laser field ($10^{14} - 10^{16}\, W/cm^2$) ionizes the gas atom. Then, the electron tunnels through the atomic potential barrier (Figure 2-3 (a)).

Acceleration of the free electron, the free electron generated by tunneling with a zero initial velocity is accelerated away from the parent ion by the driven field. In the next quarter cycle of the field, the electron is driven back to the parent ion.

The highest given return energy to the electron takes place at the phase of 17º after the crest peak where the tunneling ionization takes place. These can be explained classically in [88] and quantum mechanically in [78]. This is shown in Figure 2-3 (b).

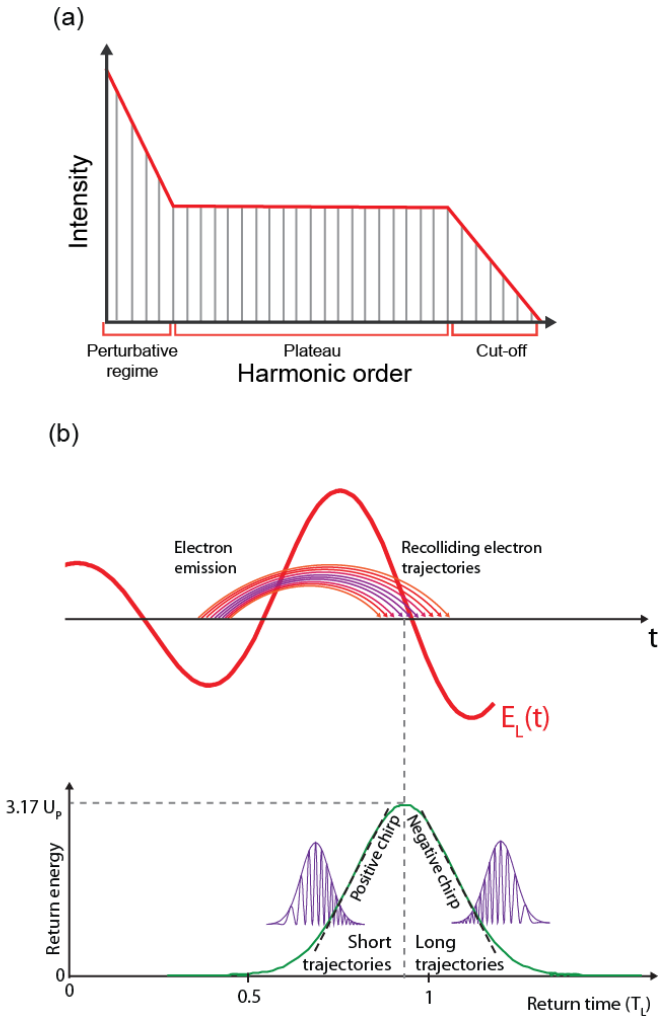

Figure 2-2: (a) The HHG spectra divided into three regions, Perturbative regime, and plateau and cut-off region. (b) For an isolated recombination cycle of ionized, accelerated and recombining electrons, trajectories for different times of birth are visualized in the higher panel, while in lower panel. The vertical coordinate displays the distance from the parent ion versus the return time in laser cycles T_L (illustration is adapted from [22]).

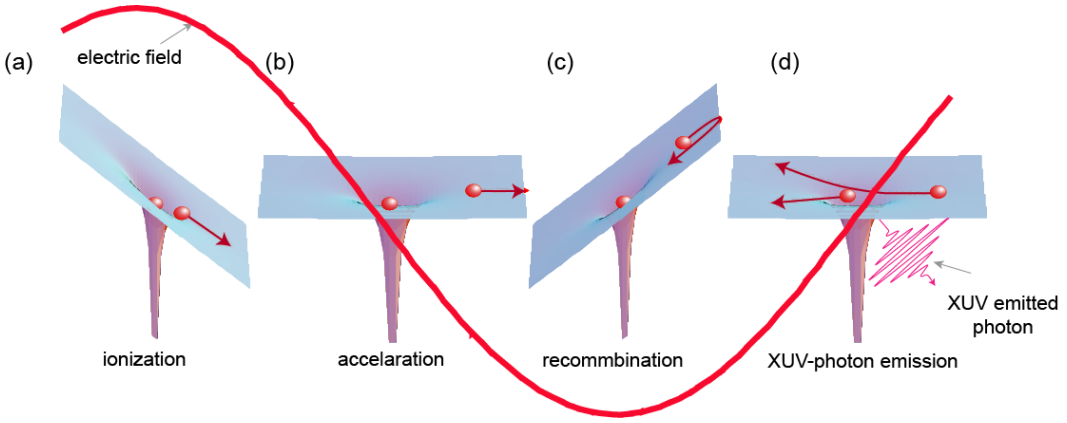

Figure 2-3: Illustration for the three-step model for HHG generation, (a) the tunnelling ionization occurs in an atom by high intensity laser field. (b) the electron accelerated by the laser field away from the parent ion. (c) the recombination of the electron with the parent ion which this leads to emitting of EUV photon, as shown in (d) (illustration is taken from [89]).

Figure 2-2 illustrates the dependence of the energy of the electron on its trajectory. The electrons encounter the core at different times with different energies depending on the ionization moment. The lower panel shows the corresponding return energy as a function of return time. The trajectory with the highest return energy defines the cut-off energy. If the recolliding electron trajectories have return times smaller than the excursion time of the trajectory which provides the highest return energy, these are called short trajectories and, otherwise, long trajectories.

Recombination, the electron recombines with its parent ion and a broadband extreme-ultraviolet (EUV) photon is emitted (Figure 2-3(c) and (d)). The extremely low probability of a recombination has, as a consequence, the very low EUV efficiency of radiation in the cut-off range ($\sim 10^{-6}$). The EUV bursts emerge as a train of attosecond pulses with a half optical laser period $T_{osc}/2$ spacing in time domain which corresponds to $2\hbar\omega_0$ in the frequency domain.

Controlling the shape and the waveform of the optical pulse controls the amplitude (ionization) and the phase of the recombination of the electrons and generated EUV pulse. Such control has been possible by controlling the carrier envelope phase (CEP) of few cycle pulses and comprises an essential prerequisite for gen-

erating reproducibly single attosecond EUV pulses. EUV bursts being dominated by short trajectories carry positive chirp, while these are being dominated by long trajectories carrying negative chirp [90]. As a consequence, by filtering out the most energetic recombination events, the EUV burst would carry the least amount of chirp. These days, isolated attosecond pulses are generated by utilizing 1.5 cycle (800nm) driver pulses in combination with spectral filtering of the cut-off HHG radiation, as illustrated in the Figure 2-4.

Special ultrathin metal filters such as zirconium, aluminum and palladium, with thickness of about 150 nm, in combination with EUV multilayer optics are acting as optical high-pass filters for the generated EUV photons. This combination allows the adjustment of the central energy and bandwidth of the attosecond EUV pulse, based on the requirement of the experiment applications. The photons transmitted through the filter are the prerequisite for a single isolated attosecond pulse.

However, the ϕ_{CEP} setting of the pulse affects the energy and the number of generated EUV photons, as illustrated in Figure 2-4. For a cosine waveform ($\phi_{CEP} = 0$) (Figure 2-4 (a)) only one recombination event creates the EUV photons transmitted through the spectral filter. However, for a sine waveform ($\phi_{CEP} = \pi/2$) (Figure 2-4 (a)), two subsequent recombination bursts are generating photons of a similar energy distribution which can transmit through the spectral filter. Hence, the ϕ_{CEP} should be close to zero. As the driver pulse becomes shorter, the probability to create a satellite EUV attosecond pulse decreases.

There are other techniques that can be used for isolating the attosecond pulses generated via HHG. For instance; polarization-gate [91], and generalized double optical gating (GDOG)[92]. In this thesis work, the spectral gating technique for generating isolated EUV pulses is used, utilizing the advantage of very short driver pulses are generated in our laboratory.

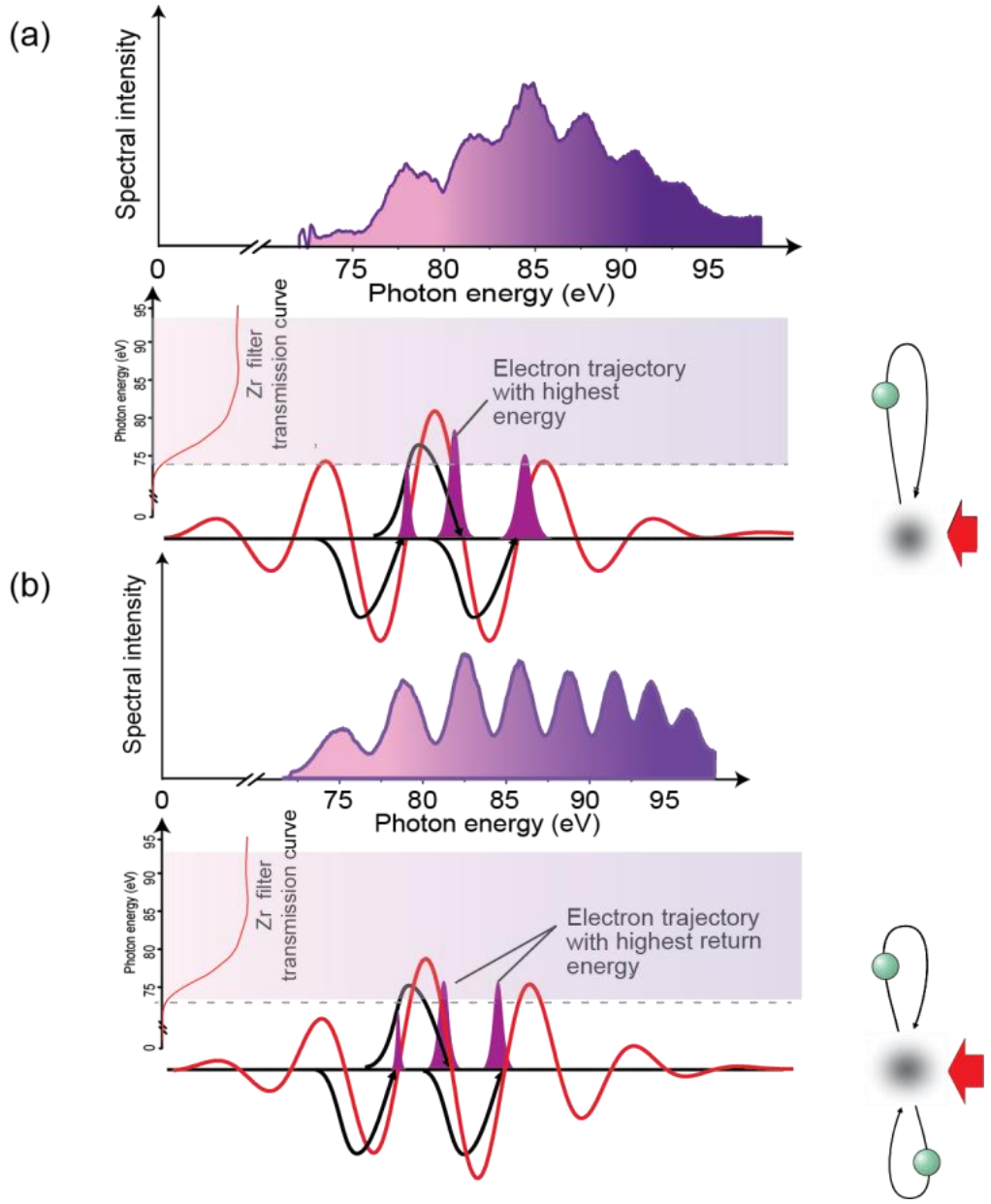

Figure 2-4: Generation of isolated attosecond light bursts by means of spectral gating utilizing an optical high pass metal filter in combination with EUV optics. (a) For a cosine waveform $\varphi_{CEP} = 0$ only the strongest recombination event is spectrally gated, the reflective curve for the 150nm ultrathin (150nm) Zr filter is shown in the upper graph with red line. (b) For the sinusoidal waveform $\varphi_{CEP} = \pi/2$, two identical EUV bursts (violet) are emitted. Corresponding EUV spectra are shown in the graphs on top (illustration is adapted from [22]).

Chapter 3

Femtosecond front-end phase stabilised Laser system

3.1 Laser system and its principle of operation

A femtosecond commercial laser is used in the frame of this thesis work and plays the role of the front-end source for light field synthesis and relevant developments [93]. An ultra-broadband oscillator, based on a titanium-doped sapphire (Ti:Sa) crystal and pumped by a Continuous Wave (CW) pump laser, provides the seed pulses for the amplifier system, as shown in Figure 3-1. The oscillator emits pulses (~6 fs) with an output power of ~300 mW at 78 MHz [94].

The beam which exits the oscillator is focused into a periodically poled magnesium-oxide-doped lithium niobate (PP-MgO:LN) crystal. Spectral broadening is taking place, as well as different frequency generation, which serve as the basis for the CEP stabilization of the oscillator [15,18,95]. The concept will be discussed in higher detail later in the text. Before seeding the amplifier (seed pulse energy ~ 1 nJ), the oscillator pulses are stretched to around 15 ps in a simple SF_5 glass stretcher. The complete MHz train of pulses is amplified by four passes in the Ti:Sa CPA multi-pass amplifier, pumped by a Q-switched neodymium-doped yttrium lithium fluoride (Nd:YLF) pump laser at 527 nm (~20 W), before a Pockels cell reduces the repetition rate to 3kHz. Another five amplification passes through the amplifier crystal raises the pulse energy to 1.3 mJ. Two dielectric filters, installed in the seed beam path, modulate the spectrum of the oscillator, such

that the narrowing during the amplification process is reduced and a spectral bandwidth of 70 nm is maintained after the amplification. The spectrum of the amplified pulse is shown in Figure3-2 (a).

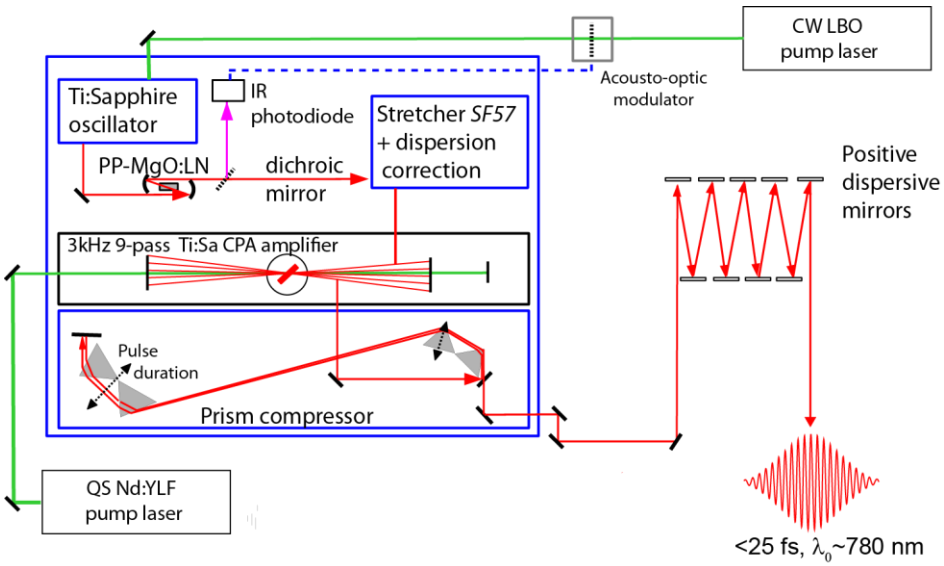

Figure 3-1: Schematic illustration of the commercial front-end consisting of a Ti:Sa oscillator seeding a 9-pass Ti:Sa amplifier system.

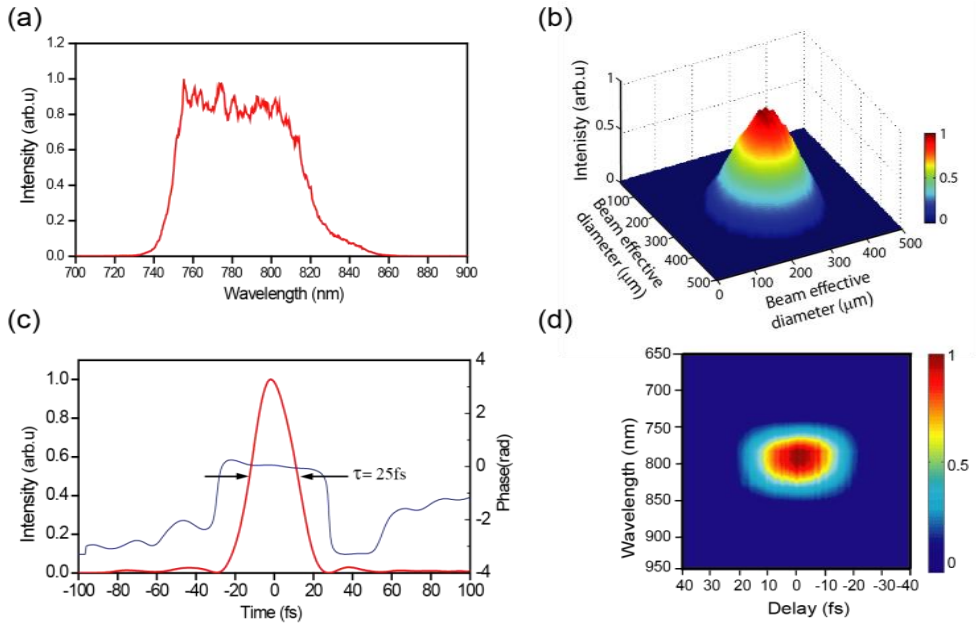

Figure3-2: properties of the laser pulses (a) The spectrum of the laser pulses. (b) The beam profile of the laser beam at the focus of (f=1.8m) lens. (c) The temporal profile of the laser pulses (τ =25fs) retrieved from recorded FROG spectrogram is shown in (d).

This spectral bandwidth of the amplified pulses supports a Fourier limit duration of ~18 fs. Subsequent re-compression takes place in a hybrid prism/positive dispersive mirror-compressor. The prism compressor is modified to over compensate for the positive chirp of the amplified pulses to avoid self-phase modulation (SPM). Then, the pulses are compressed by positive-dispersion chirped mirrors yielding ~25 fs pulses at 850 μJ [96]. These pulses have been characterized by utilizing a Transient Grating-Frequency Resolved Optical Gating (TG-FROG). The recorded spectrogram is shown in Figure3-2 (d). The temporal profile has been retrieved and it is shown in Figure3-2 (c).

3.1.1 Carrier-envelope phase stabilization of laser pulses

For few–cycle laser pulses, controlling the carrier envelope phase becomes essential for many experiments [26, 97-99] especially for attosecond experiments which are based on the generation of single isolated attosecond EUV pulses, as well as these using these waveforms, for triggering ultrafast dynamics. The pulses delivering from the laser system have to be carrier-phase stabilised. This requires the carrier envelope phase (CEP) stabilization of the oscillator and the amplified pulse.

CEP Stabilization of laser oscillator: The *f-to-zero* technique

The temporal evolution of the electric field of a pulse can be expressed as:

$$E_L(t) = A_L(t)\cos\left(\omega_L(t)t + \phi_{CE}\right) \qquad (30)$$

where, $A_L(t)$ is the pulse envelope, ω_L is the frequency of field oscillation and ϕ_{CE} is the carrier envelope phase. For nonlinear applications, which are sensitive to the strength of individual field crests, a change in ϕ_{CE} results in a physically measurable difference only if the amplitude is subjected to significant variation within the light period $T_0 = 2\pi/\omega_0$ [100].

In a laser cavity, the carrier envelope phase is shifted with each laser pulse by

$$\Delta\phi = 2\pi \omega_{CE} / \omega_{rep} \qquad (31)$$

Where ω_{rep} is the repetition rate of the laser and ω_{CE} is a frequency shift from the exact integer multiple of ω_{rep}. $\Delta\phi$ can be compensated for by adjusting the cavity dispersion. The stabilization of the laser oscillator can be achieved by forcing all the emitted pulses to carry the same phase. Locking the ω_{CE} of the oscillator can be performed to the nth fraction of the repletion rate in principle to make sure that every nth pulse of the laser pulse train has the same carrier envelope phase. The detection of the CE drift relies on the tracing of frequency beat from the laser modes of the frequency comb which are separated by a spectral octave.

The low frequency mode is frequency doubled and the two modes are interfering with each other to produce the CE frequency,

$$\omega_{CE} = 2(n\omega_{rep} + \omega_{CE}) - (2n\omega_{rep} + \omega_{CE}). \qquad (32)$$

The output of the laser oscillator is tightly focused into a highly nonlinear periodically poled magnesium-oxide doped lithium niobate (PP-MgO:LN) crystal which is optimized for the second-harmonic generation (SHG) at 1500 nm. The pulses undergo spectral broadening due to SPM and difference-frequency generation (DFG). This leads to generate spectral components of the laser pulses up to 1600 nm. DFG between modes from the high $(f_{CEO} + n_{high} f_r)$ and low $(f_{CEO} + n_{low} f_r)$ sides of the frequency comb result in frequencies at the long wavelength side of the spectrum, according to

$$f_{DFG} = (f_{CEO} + n_{high} f_r) - (f_{CEO} + n_{low} f_r) = (n_{high} - n_{low}) f_r \qquad (33)$$

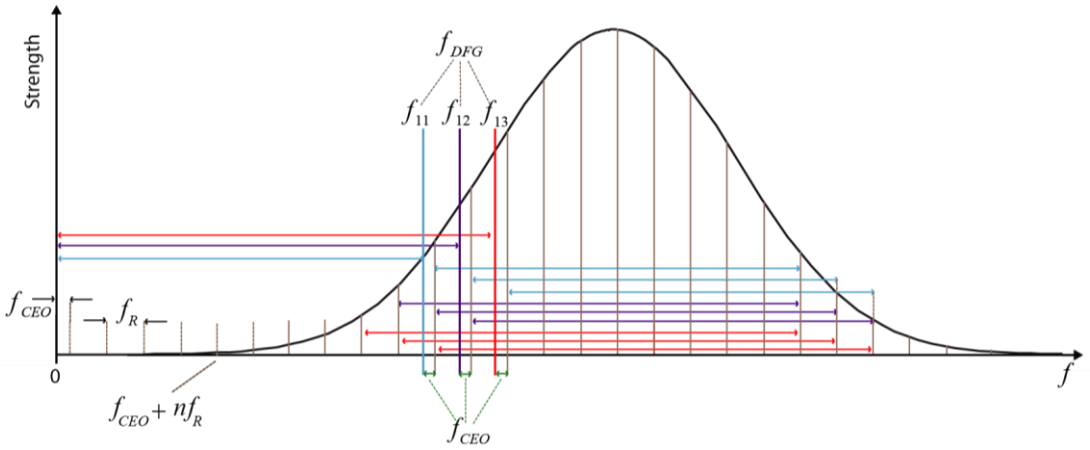

Figure 3-3: scheme for *f-to-zero* measurement used for tracking the offset frequency of the frequency comb (illustration is adapted from [114]).

Mixing those DFG frequencies spaced by multiple integers of f_r, is shown schematically with blue, violet and red arrows in Figure 3-3, with modes $f_{2k} = (f_{CEO} + k\ f_r)$ from the low-frequency wing as indicated in Figure 3-3 for which $(n_{high} - n_{low}) = k$, results in a beat frequency of f_{CEO}. This beat frequency is imprinted on the pulse train in the spectral range above 1350 nm. A dichroic mirror, in combination with a long-pass interference filter isolates the spectral range of interest and directs the beating signal into a fast photodiode. Locking electronics and the fast photodiode are used to detect the beat frequency and to generate an error signal proportional to the deviation of f_{CEO} from the desired value which is set, in this case, to one fourth of the repetition rate.

The derived error signal is used in a closed loop as a feedback signal to drive an acousto-optic modulator which is installed in the beam path of the oscillator pump laser and modulates the pump power depending on the laser system. A Pockel cell picks only integer multiples of every fourth pulse of the oscillator output pulse train to ensure amplification of only isolated pulses which should have, by definition, in the absence of any thermal/optical fluctuations, the same carrier-envelope

phase and, thus, inherit identical waveforms. The stabilization is used to compensate for phase drifts that occur due to instabilities introduced by thermal changes or drifts of the pump laser parameters, as well as path length drifts.

CEP stabilization of amplified pulses: The *f-to-2f* approach

This technique is based on the frequency conversion of the generated broadband spectrum by the nonlinear propagation in hollow core fiber filled with pressurized Ne gas, as will be explained in detail in the next chapter. The low-frequency wing of that supercontinuum ($f_{CEO}+n_{low}f_r$) is doubled and recombined with the high-frequency wing ($f_{CEO}+n_{high}f_r$), as shown in Figure 3-4.

A part of the supercontinuum broadband spectrum after the HCF (~3%) enters the detection set up for the phase stabilization which is the so called $f-2f$ interferometer which is shown schematically in Figure 3-5(b). In this interferometer, the light is focused by a parabolic mirror into β-BBO where the second harmonic generation takes place.

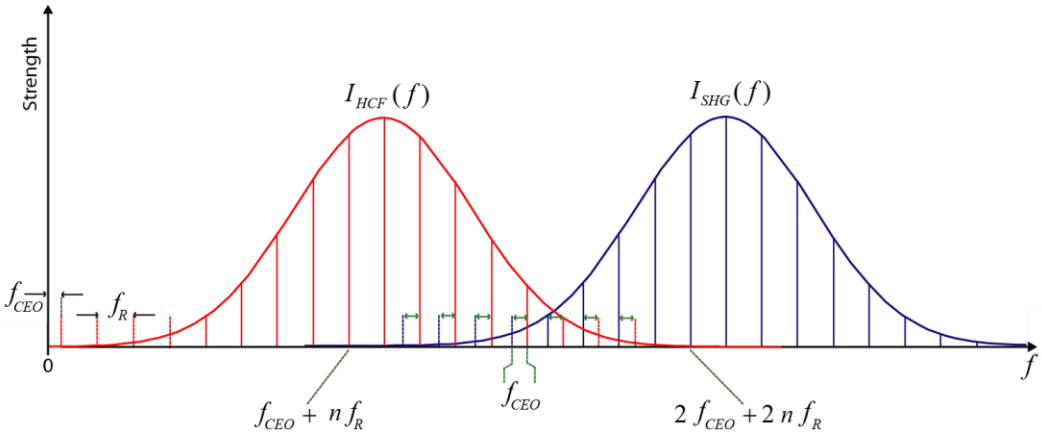

Figure 3-4: *f*-to-2*f* measurement scheme used for tracking changes in the carrier envelope phase of amplified pulses (illustration is adapted from [114]).

A short-pass filter and half-wave plate are installed in the beam path for filtering the low frequency part of the spectrum and to correct the polarization of the second harmonic generated frequency, in order to have the same polarization of the broadband spectrum. Beating of the modes $(2f_{CEO}+2n_{low}f_r)$, with modes $(f_{CEO}+n_{high}f_r)$ gives rise to a beat note at

$$2(f_{CEO}+n_{low}f_r)-f_{CEO}+n_{high}f_r=f_{CEO}. \tag{34}$$

Experimentally, the signature of the beat frequency is observed in the form of an interference pattern (Figure 3-5(a)) in the spectral region where the fundamental and the frequency doubled light overlap.

A Glan-Thompson polarizer is used to adjust the relative intensity and the interference pattern which carries the information about changes in the carrier envelope phase. The spectral interference, shown in Figure 3-5(a), is recorded with a fiber spectrometer.

Mathematically treated, the spectral interference resultant $S(f)$ between the output of the fiber I_{HCF} and its frequency doubled counterpart I_{SHG}, separated by a time delay τ upon walk-off effects in the $\alpha-BBO$ and related optics, can be expressed as

$$\begin{aligned} S(f)=&(1-\in)I_{HCF}(f)+\in I_{SHG}(f)+2\sqrt{\in(1-\in)I_{HCF}(f)\,I_{SHG}(f)} \\ &\cos(\phi_{SHG}(f)-\phi_{HCF}(f)+2\pi f\tau+\phi_0). \end{aligned} \tag{35}$$

Where $\in$ is the polarizer transmission for the polarization of the SHG light, ϕ_0 the carrier envelope phase and $\phi_{SHG}(f)\,\&\,\phi_{HCF}(f)$ denote the spectral phase of the fiber broadened (frequency doubled) pulse [100].

A Fourier analysis of the part of the spectrum containing the interference pattern tracks changes of ϕ_0 . Changes of the spectral phases of the two interfering spectra, and especially of the delay between the two interfering pulses, can be neglected for an intense-stable laser system. A standard proportional controller algorithm adjusts the insertion of the prisms in the prism compressor, based on the deviation of the fringe phase of the interference pattern from the user defined reference phase. The achieved CEP stability is typically better than 100 mrad rms fluctuations[101].

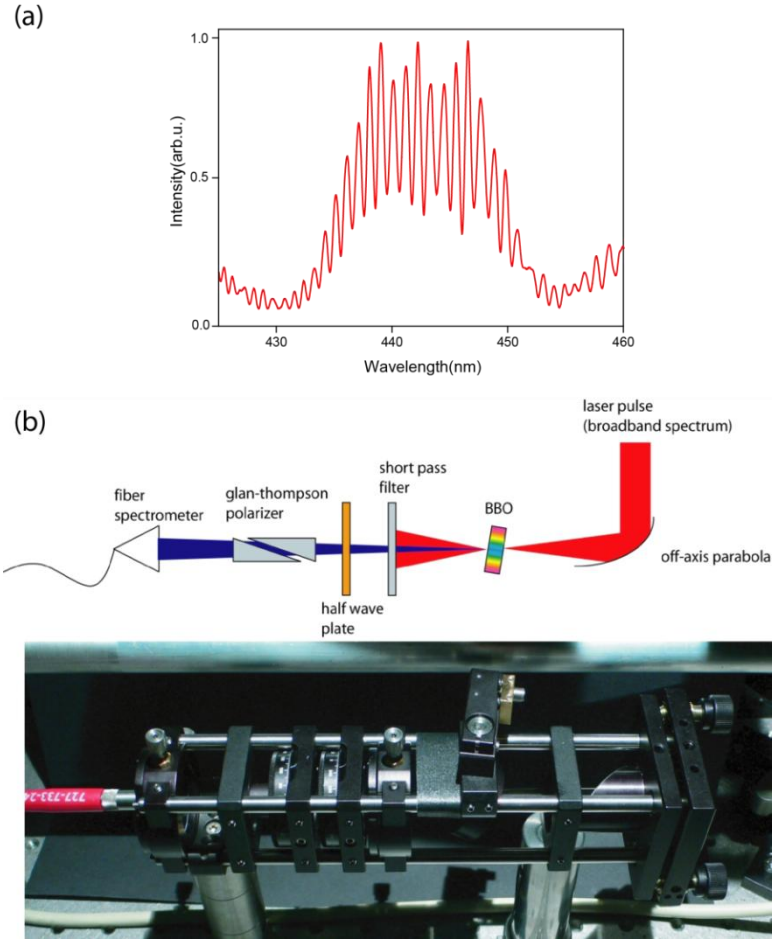

Figure 3-5: *f*-2*f* interferometer setup. The supercontinuum pulses are focused on thin α-BBO thin crystal and second harmonic is being generated. By adjusting the polarization vector of the supercontinuum and the second harmonic generated beam by a half wave plate and a polarizer, interference fringes can be traced by the spectrometer.

Chapter 4

Light field synthesis

In this chapter, a three-channel light field synthesizer is demonstrated. It controls the properties of light spans over more than 1.5 octaves. The supercontinuum source, the light field synthesizer apparatus and the relevant technological advances will be discusses. Theses technological advances includes the transportation of the supercontinuum spectrum to/from the synthesizer, the full characterization of the constituent spectral band`s pulses of the synthesizer, the coherent superposition of these pulses and the stabilization of this sophisticated polychromatic interferometer with very high precision.

4.1.1 Supercontinuum, intense light source

The broadband light source is an essential prerequisite for light field synthesis. The supercontinuum generation is based on the nonlinear propagation of the multi-cycle laser pulse in a gas filled hollow core fiber (HCF).

The produced laser pulses from the system (~ 25 fs, a pulse energy of >800 μJ and carried at central wavelength ~780nm) are focused by a bi-convex lens (f=1.8 m). The beam size at the focus is ~ 200 μm (Figure3-2). The converging beam enters the HCF chamber, which is schematically illustrated in Figure 4-1(a), through a ~0.5mm fused silica (anti-reflection coated) entrance window mounted in far distance (~80 cm) to reduce the self-phase modulation.

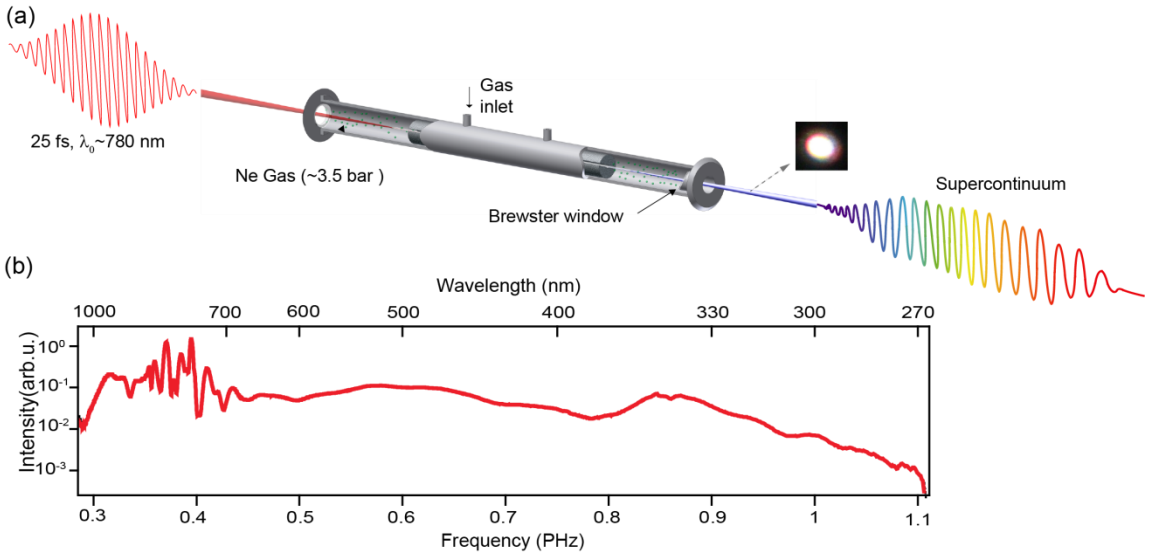

Figure 4-1: Supercontinuum light generation. (a) Supercontinuum generation in a Ne-filled hollow-core fiber (b) The generated supercontinuum with nearly uniform intensity (~20 dB) spanning over about two optical octaves (1100 nm-270 nm) (illustration is taken from [70]).

The HCF apparatus consist of a fiber with inner diameter 250 μm and a length of ~1.1 m. The container chamber is filled with Ne. The Ne gas pressure has been adjusted inside the chamber to ~2.0-3.0 bar, in order to yield the broadest spectra [102].

This broadband spectrum exits the capillary through a thin (~0.5 mm) UV-grade fused silica window, which is mounted at Brewster's angle of ~780 nm at the end of the HCF`s chamber, in order to provide efficient transmission over a broad spectral range [77]. The generated supercontinuum spectrum spans over more than two octaves extending from the IR to the DUV (1100 to 270 nm) with a uniform intensity (~ 20 dB), as shown in Figure 4-1(b). The HCF technique has been chosen, because it generates an intensive supercontinuum and it is being implemented for high power well beyond the damage threshold of solids.

The generated supercontinuum has energy ~450 μJ– (~56%. transmission) with an excellent beam profile and pulse to pulse energy stability (< 1 % normalized rms).The CEP of the generated supercontinuum pulses is stabilised, as explained in (3.1.1).

4.1.2 Transportation of the supercontinuum

For the 1.5-octave supercontinuum (350-1000 nm) transportation, silver coated mirrors have been chosen. Silver mirrors provide a high reflectivity on average a reflectivity, which is higher than ~ 97% over the entire band. The divergent beam exiting the HCF is recollimated to a diameter of ~9 mm by a spherical, silver-coated, mirror (f =87.5 cm) and with two additional reflections on flat silver-coated mirrors, it is guided to the field synthesizer.

4.1.3 Three channel (1.5-octave) light field synthesizer apparatus

Inside the prototypical three-channel (1.5-octave) light field synthesizer [77], represented in Figure 4-2(a), the broadband spectrum is decomposed utilizing two types of dichroic beamsplitters (DBSs). The $DBS_{UV\text{-}Vis}$ reflects the band from (350-500 nm) and transmits the band from (500-700), while, $DBS_{Vis\text{-}NIR}$ reflects the band from (500-700 nm) and transmits the band from (700-1100 nm). Theoretical spectral response of the DBS's is shown in Figure 4-3(a). The synthesizer contains three constituent spectral channels, each channel spans over approximately 0.5-octave, as follow; Ch_{NIR} spans over the near-IR spectral region (700-1100 nm), Ch_{VIS} spans over the visible spectral region (500nm-700 nm) and $Ch_{VIS\text{-}UV}$ spans over the part of the visible and ultra-violet spectral region (350nm-500 nm), as shown in Figure 4-4 (a).

The design strategy of the synthesizer is highly important as it minimizes the exposure of the short wavelength spectral components —most susceptible to dispersion— of the supercontinuum pulses to material propagation while, at the same time, minimizes the complexity —to the benefit of performance— of the dichroic beamsplitters as they are required to deal with narrower spectra, as the beam advances into the synthesizer. Indeed, the beam splitter $DBS_{Vis\text{-}NIR}$ is designed to manage a narrower bandwidth in comparison to $DBS_{UV\text{-}NIR}$. This strategy has also important consequences for the scalability of the synthesis towards the deep ultraviolet as will be demonstrated later in this thesis.

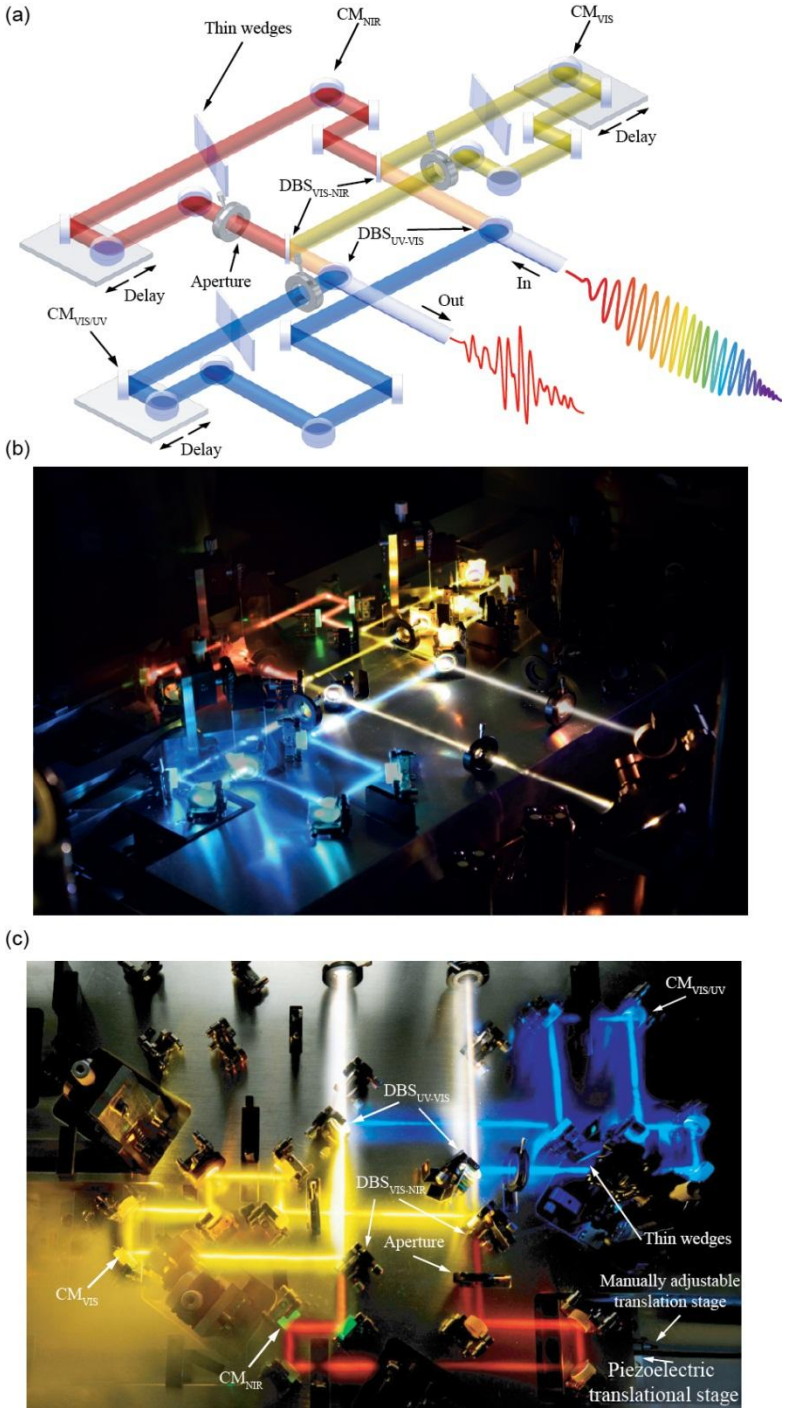

Figure 4-2: (a**) Schematic representation of a prototypical three-channel (1.5–octave) light field synthesizer. DBS (Dichroic Beamsplitters), CM (chirped mirrors). (b) Photograph (perspective) of the light field synthesizer in operation (c) Top view of the apparatus (illustration is taken from [70]).**

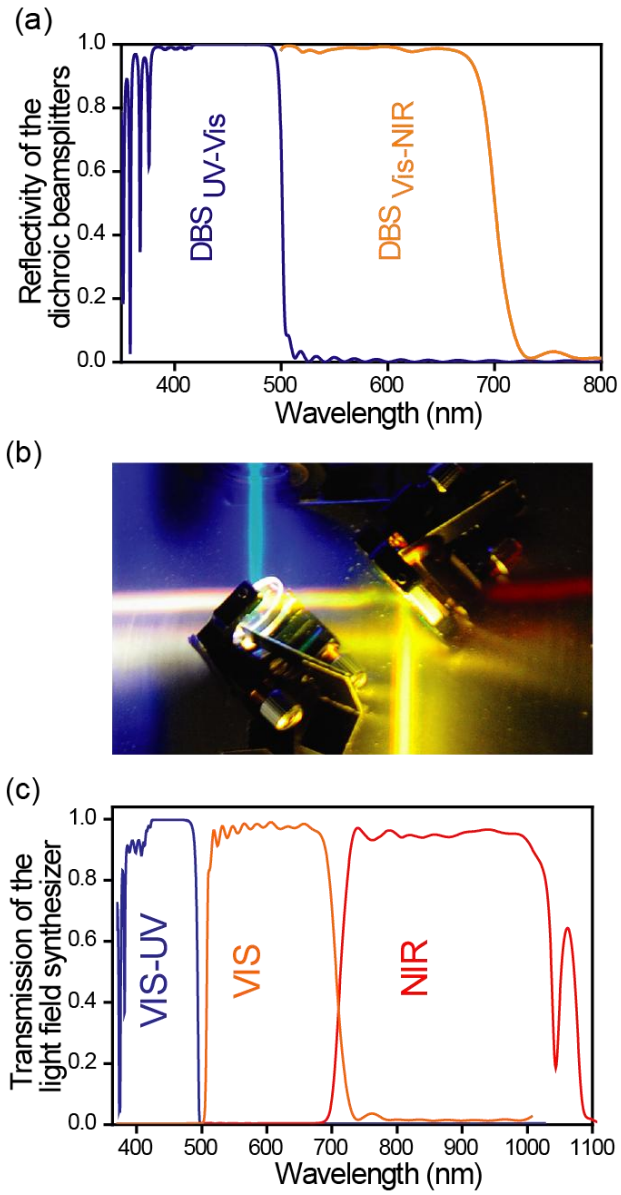

Figure 4-3: Dichroic Beamsplitters (a) simulated reflectivity of the dichroic beamsplitters (DBS_{UV-Vis} and $DBS_{Vis-NIR}$). (b) Photograph of DBS_{UV-Vis} and $DBS_{Vis-NIR}$ in action. (c) Simulated transmission of the individual channels of the optical field synthesizer (illustration is taken from [70]).

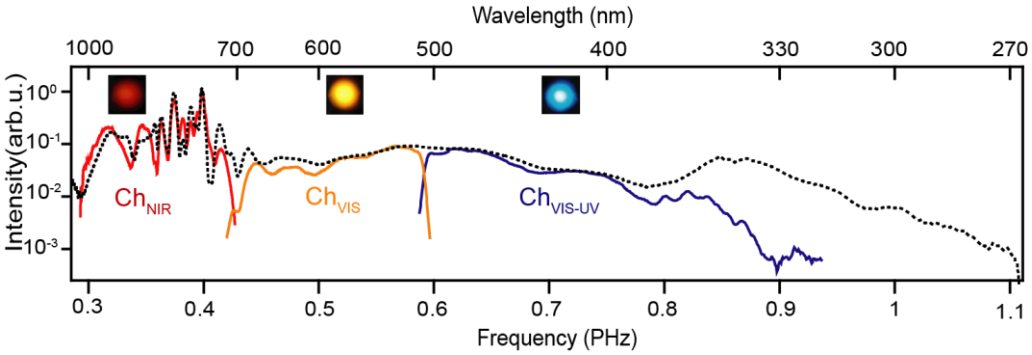

Figure 4-4: Spectra of pulses in the constituent channels of the three channel synthesizer are shown in red for Ch_{NIR} (700nm to 1100 nm), yellow for Ch_{Vis} (500nm to 700 nm), and blue for $Ch_{Vis\text{-}UV}$ (350nm to 500 nm). Insets show photographs of the beam profiles of the individual channels taken at the exit of the apparatus (illustration is taken from [70]).

The pulses of the constituent channels of the synthesizer are temporally compressed by six dispersive (chirped) mirrors [41]. The dispersive mirrors are introduced into the beam path of the corresponding channel (CM_{NIR} in NIR channel, CM_{Vis} in visible channel and $CM_{Vis\text{-}UV}$ ultra-violet channel) and are designed to compensate the positive dispersion of the pulse of each channel. The design strategy of these optical elements contains two steps. First, the dispersion measurements, utilizing six-metal coated mirrors in place of the chirped mirror by transient grating (TG) based, Frequency Resolved Optical Gating (TG-FROG) apparatus. The measured uncompressed pulses of the three constituent channels are shown in Figure 4-5. Second, design the dispersive mirrors, the retrieved spectral phases are used as a target for the design of the dispersive mirrors of each channel [103].

To allow flexible dispersion control, the dispersive mirrors are designed to be able to deal with the dispersion corresponding to the propagation through ~2 m of air plus 1-2 mm of fused silica in each channel. On other word, the dispersive mirrors are able to compensate for approximately (-75 fs^2) per reflection for the chirped mirrors of $Ch_{Vis\text{-}UV}$, (-70 fs^2) of Ch_{Vis} and (-70 fs^2) of Ch_{NIR}. The theoretical reflectivity and overall transmission of the synthesizer optics are shown in Figure 4-3 (a) and (b).

In reality, the contrast of the spectral partition is, somewhat, lower than what is designed; the overall transmission through the synthesizer is ~83%. The transmission per optical channel is as follows; Ch_{NIR} ~85%, Ch_{Vis} ~74%, and $Ch_{-Vis-UV}$~57%. The synthesized field at the exit of the synthesizer carries an energy of ~300 µJ, distributed among the three channels as (Ch_{NIR}~250 µJ, Ch_{Vis}~36 µJ and Ch_{Vis-UV}~14 µJ).The constituent channels pulses are spatiotemporally superposed—with the same type of beamsplitters—at the exit of the apparatus.

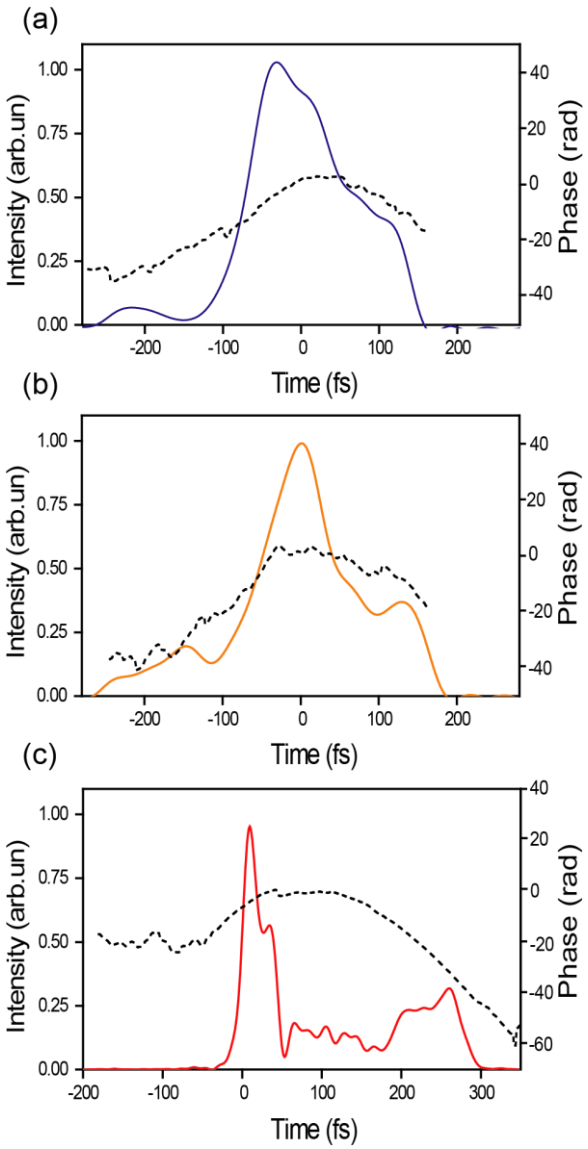

Figure 4-5: The temporal profile of uncompressed pulses and phases of Ch_{UV-Vis} ,Ch_{Vis} are shown in (a), (b) and (c) respectively

There are many elements that have been implemented inside the apparatus and serve for the control of the properties of the synthesized waveforms. These elements are; a pair of movable, thin, *fused silica wedges* (apex: 2°48', 30x20mm) introduced in the beam path of the individual channels—at the Brewster angle of each band, to minimize losses—used to fine-tune the dispersion as well as the CEP phase of the constituent pulses, *adjustable irises*, which have been introduced in the beam path of each channel (Figure 4-2(a)) for controlling the relative intensities among constituent channels, and *a translation unit*, which carries a pair of mirrors in the path of each constituent channel to adjust the relative phases. This unit consists of; (a) A manually adjustable translation stage (precision ~10 μm) used for coarse adjustment of the optical paths in each channel, and (b) a piezoelectric translational stage, is used for finer adjustments of the temporal delays of individual channels with the necessary attosecond precision. In the implementation presented here, rough optical path adjustment is possible for all optical channels while fine resolution (via piezoelectric stages), and is implemented only for $Ch_{Vis\text{-}UV,}$ and Ch_{NIR}.

4.1.4 Temporal characterization and compression of pulses in the constituent channels

The temporal characterization of the pulses of the constituent channels ($Ch_{Vis\text{-}UV,}$ Ch_{Vis} and Ch_{NIR}) has been performed by compact, homemade, transient-grating-based, Frequency-Resolved Optical Gating (TG-FROG) apparatus. The schematic diagram and a photograph of the apparatus are shown in Figure 4-6(a) and (b), respectively. In the TG-FROG apparatus, the input beam is divided into three identical beams via a spatial input mask. The three beams are focused by a split concave mirror to a thin fused silica substrate that acts as the nonlinear medium.
A piezoelectric actuator attached on one of the two D-shaped segments of the split mirror is used to introduce a delay with nanometric precision. Using the concave mirror for focusing the beam minimizes multiple reflections in the apparatus.

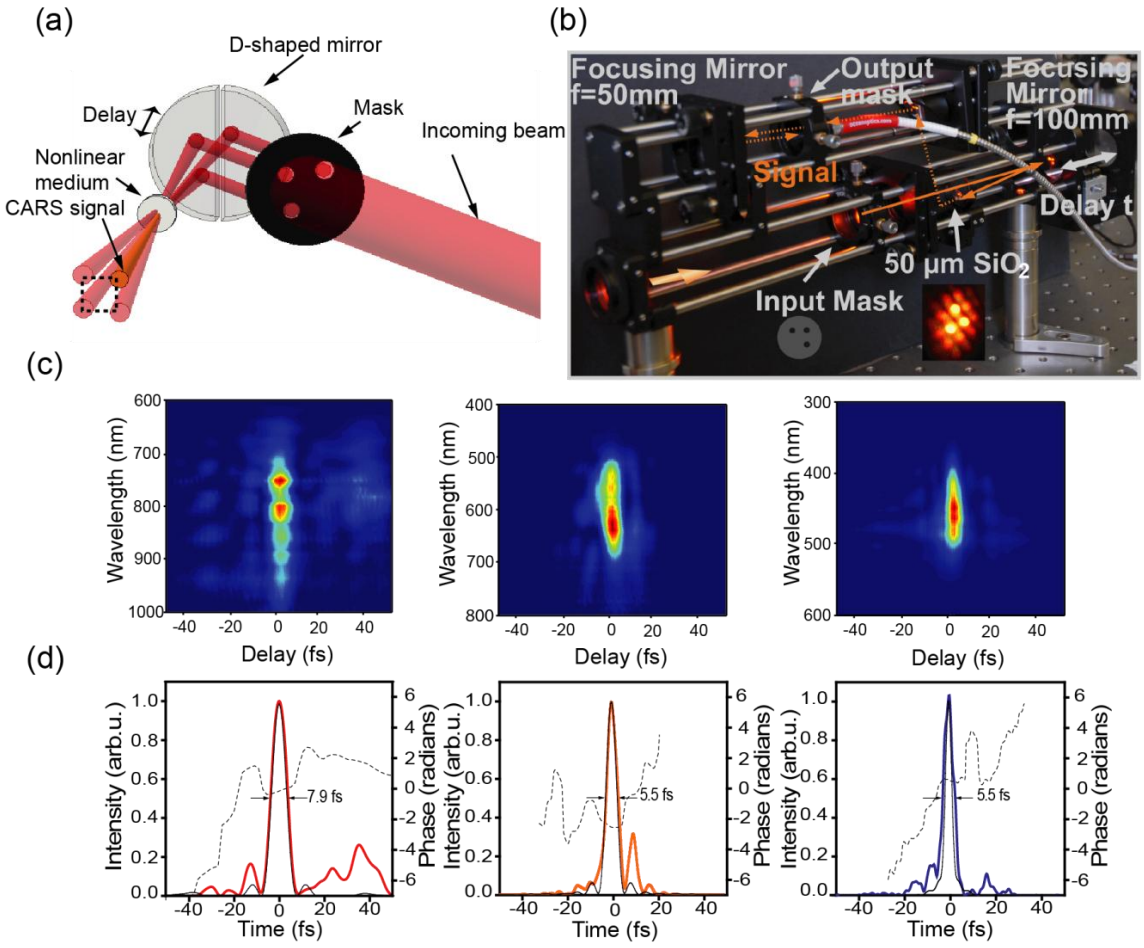

Figure 4-6: Temporal characterization of the three-channel synthesizer pulses. (a) Schematic illustration for the TG-FROG setup. (b) Photograph of the TG-FROG. (c) Recorded TG-FROG spectrograms of the Ch_{NIR}, Ch_{Vis} and Ch_{Vis-UV} pulses respectively. (d) The retrieved temporal intensity (solid lines) and phase (dashed curves) profiles of the corresponding pulses. The thin black lines represent the intensity profiles of the corresponding bandwidth-limited pulses (illustration is taken from [70]).

The three wave mixing process occurs and the non-linear signal pulses are generated at the same wavelength range as the pulses under characterization [104]. To mimic the pulse properties of the constituent channels in the experiment apparatus, a piece of fused silica with the same thickness of the entrance window of the experiment apparatus (~0.5mm) has been implemented in the beam path of the TG-FROG apparatus. The FROG spectrograms of constituent channel pulse have been recorded at the exit of the synthesizer.

Temporal intensity profiles and phases of the $Ch_{NIR,}$ Ch_{Vis} and $Ch_{Vis\text{-}UV}$ pulses have been retrieved from the recorded FROG spectrograms by using commercial software (Femto-soft Technologies). These spectrograms are shown in Figure 4-6 (c). The dispersion of the individual channel pulses can be adjusted by adjusting the thin pair of wedges in the beam path of the individual channel. The FWHM pulse duration of the individual channel pulses are $\tau_{Ch(NIR)}$ = 7.9 fs, $\tau_{Ch(Vis)}$ = 5.5 fs, and $\tau_{Ch(Vis\text{-}UV)}$ = 5.5 fs. These are close to the pulses duration of its bandwidth-limit.

4.1.5 Coherent superposition of the constituent fields

Light field synthesis in this work is based on the coherent superposition of polychromatic pulses. The pulses of the constituent channels of the synthesizer therefore should be spatially and temporally overlapped. Moreover, the pulses should have the same divergence. In the next sections these developments will be discussed.

4.1.5.1 Spatial overlap

As the envisaged applications will require high intensities, the properties of the synthesized field waveforms need to be optimised in the focus of their beam; therefore, the spatial overlap of the constituent channel pulses is essential to be performed in the Rayleigh range of the focusing polychromatic beam.

The setup illustrated in Figure 4-7 (a) is used for investigating and monitoring the spatial properties within the Rayleigh range of all constituent pulses. This setup contains: a CCD based beam profiler mounted on a linear motorized stage, this stage can be longitudinally translated along the Rayleigh range of the focused beam, and spherical mirror-with a focal length (f= - 40 cm), similar to the focusing element is used for focusing the synthesized waveform in the experimental apparatus. The constituent channel pulses are overlapped in the focal plane to ensure their angular alignment, whereas, the lateral alignment can be achieved by their spatial superposition at the exit aperture of the synthesizer. The focal spot

sizes of all three constituent beams are quite comparable (Ch_{Vis-UV}=60 µm, Ch_{Vis}=75µm, Ch_{NIR}=65 µm), as shown in Figure 4-7(b).

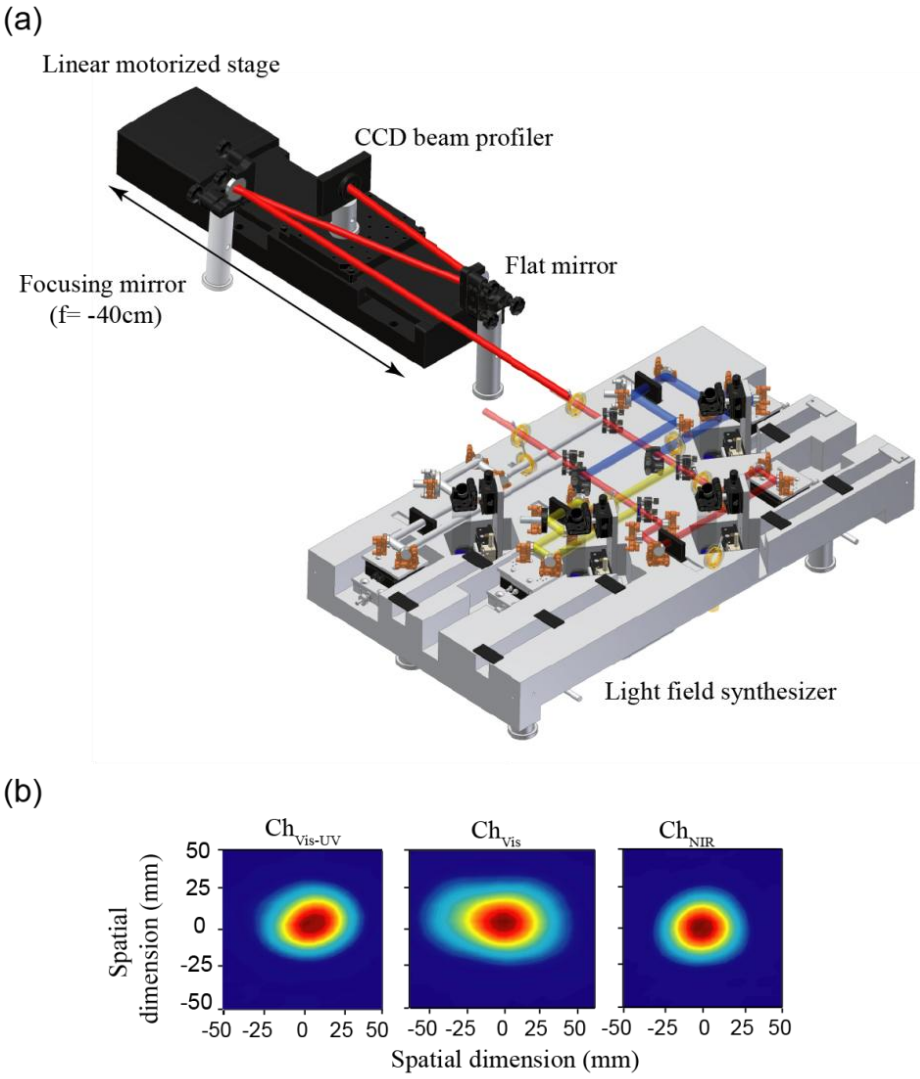

Figure 4-7: Spatial overlap of the constituent beams in the field synthesizer (a) imaging setup (b) beam profiles for pulses of Ch_{Vis-UV}, Ch_{Vis} and Ch_{NIR} in the focus of a spherical mirror (f = 40 cm) placed at the exit of the apparatus. The corresponding effective beam diameters are: Ch_{Vis-UV} (60 µm) , Ch_{Vis} (75µm) and Ch_{NIR} (65 µm).

4.1.5.2 Divergence

The constituent beams should have the same divergence, in other words; the beam wavefront of the pulses should match at any point along the propagation axis. This is hardly possible if the beams are transmitted or reflected through/off various different optical elements which can arbitrarily affect their wavefront, such as beamsplitters, mirrors, thin wedges, etc.

In the light field synthesizer, employed two types of dichroic beamsplitters, $DBS_{UV–Vis}$ and $DBS_{Vis\text{-}NIR}$, which can affect the beam properties. The coating procedure of these beamsplitters, are based on deposition of the dielectric coatings at the front side of a plane substrate; this induced a radius of curvature (f~-10 m) effect. To compensate for this deformation and to minimize the losses of the transmitted pulses, a broadband antireflection coating is deposited at the rear side of each beamsplitter to a thicknesses comparable to that of the dielectric coating, $DBS_{UV–Vis}$ (4.4 μm) and $DBS_{Vis\text{-}NIR}$ (4.7 μm), on the front side. This creates a balance between the strain forces exerted at both faces of the dichroic mirror and results in a rough correction of the deformation. Focal profiles sampled at the beam waist of each constituent channel utilize the imaging system in Figure 4-7 (a). The variation of the effective beam size (at $\sim 1/e^2$, average diameters in x and in y axis) along the Rayleigh range is shown in Figure 4-8 (a). Primarily, aberrations on the beams of $Ch_{Vis\text{-}UV}$ and Ch_{Vis} are present, because they are reflected off two dichroic beamsplitters each. The beam of Ch_{NIR} is virtually unaffected as the beam path in this channel is comprised only of dispersive mirrors. Most importantly, a considerable longitudinal displacement of the focal spot of Ch_{Vis} suggests aberrations not corrected by the balancing antireflection coating. For finer corrections of the beam wavefront, a more elaborate scheme has been introduced. It is based on the mechanical adjustment/adaptation of the radius of curvature of a thin (originally flat) mirror installed in the beam path of the Ch_{Vis} channel.

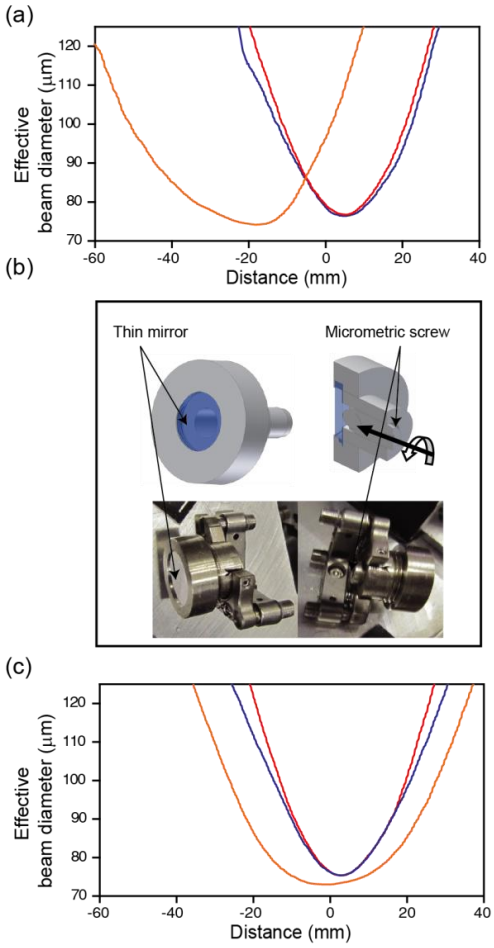

Figure 4-8: Divergence measurements of the constituent beams of the three-channel synthesizer. (a) Tracing the focal profile of Ch_{NIR} (red line), Ch_{Vis} (orange line) and $Ch_{Vis\text{-}UV}$ (blue line) by sampling their beam sizes through their confocal parameters. (b) Module for beam divergence control. (c) Focal profiles of the beams of the three channels after optimizing the divergence of Ch_{Vis} with the module represented in (b) (illustration is adapted from [70])

The adjustment module, shown in Figure 4-8 (b), is based on the action of a micrometric actuator attached to the rear side of the mirror. Adjustment of the divergence of a beam -within this scheme- result in a displacement of the focal point (here, the center of the confocal parameter)—beam waste— along the propagation axis. Corrections are implemented by the adjustment of the beam divergence of Ch_{Vis} by the module used, yield satisfactory overlap of the foci, as shown in Figure 4-8(c).

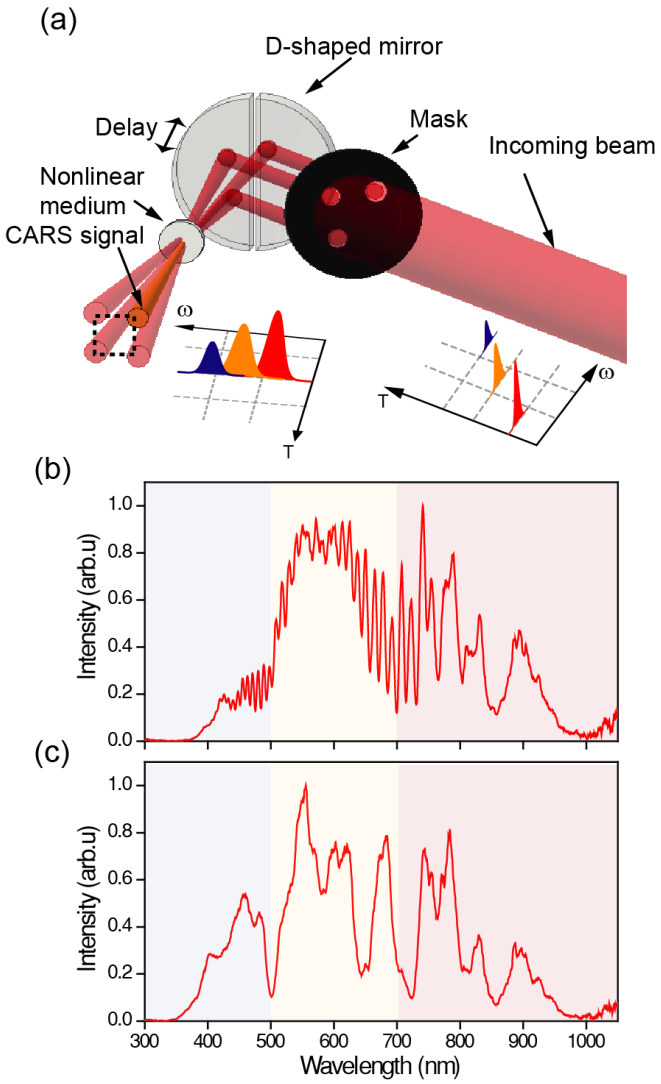

Figure 4-9: **Temporal synchronisation of the constituent channels of the field synthesizer. (a) Schematic illustration of the basic idea of the temporal synchronisation of the synthesizer pulses. The nonlinear generated signal pulses are broader in comparison to the original pulses and results in spectral fringes at the spectral borders of adjacent channels (b) or temporal overlap to yield a single spectral fringe upon adjustment of the optical paths (c) (illustration is taken from [70]).**

4.1.5.3 Temporal Synchronisation

Temporal synchronisation of the light field synthesizer pulses can be attained by the TG-FROG apparatus introduced in (4.1.4). The basic idea is that the nonlinear signal pulses are spectrally broader, as compared to their driver pulses. Hence, although the spectra of the pulses in these channels virtually do not overlap, see for example the spectral partitions in Figure 4-4, interference between their considerably broader nonlinear signal pulses offers a convenient way to trace their relative delays via the principles of spectral interferometry, as illustrated in Figure 4-9 (b). For synchronising the constituent channels' pulses, Ch_{Vis} is considered as reference, and by adjusting the piezo stages and/or the manually adjustable translation stage that integrated in $Ch_{Vis\text{-}UV}$ and Ch_{NIR}, one can adjust the relative delays to zero. This yields a reduced number of the spectral fringes to a single fringe, as shown in Figure 4-9 (c).

4.1.6 Passive and active path-length stabilization

The stability and reproducibility in creating a synthesized field is essential for high precision attosecond applications and high field experiments. This level of stability can be achieved by passive, as well as, active path length stabilization for the synthesizer apparatus.

4.1.6.1 Passive stabilization

The synthesizer apparatus has been designed as a quasi-monolithic setup where the mounts that host the optical components are directly attached to monolithic aluminum board, as shown in Figure 4-10. Thermal stabilization is achieved by constant water flow. The temperature of the water is stabilized at 19 º C by a water cooler with an accuracy of ~0.1º C.

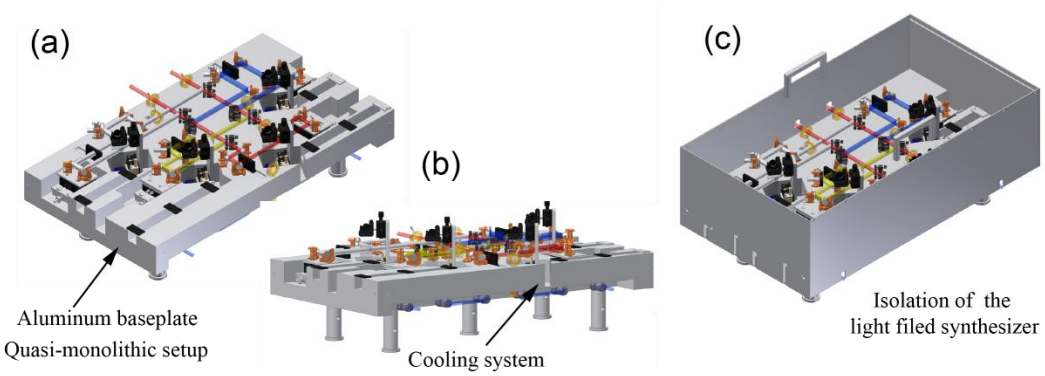

Figure 4-10: Passive stabilization of the light field synthesizer. (a) Quasi-monolithic setup of the light field synthesizer. (b) The cooling system. (c) The light field synthesizer is tightly covered to shield it from the air flow.

4.1.6.2 Active stabilization

Additionally, an active stabilization scheme has been implemented to ensure compensation against long term drifts. This scheme exploits two key features of the experimental apparatus: (a) the supercontinuum source suffers a small degree (~ 1-2%) of de-polarization, this rise *S* polarized components despite that the supercontinuum source is optimized for *P* polarization and (b) that each constituent channel in the synthesizer exhibits a wider spectral transmission for its *S* rather than for its *P* polarization components, even at very limited efficiency and dispersion control. These features enable spectral overlap between *S* and *P* polarized spectral components from a channel and its adjacent ones, and the introduction of additional group delay (typically, tens to hundreds of femtosecond, here) among them, given that the phase properties for *S* and *P* polarization are different in dielectric optics at non-normal incidence. For the use of spectral interferometry as a method to trace and control the timing between pulses in adjacent channels, the latter is essential, because it can permit generation of several fringes in the area of spectra overlap between these bands even though the *P* components are perfectly synchronized.

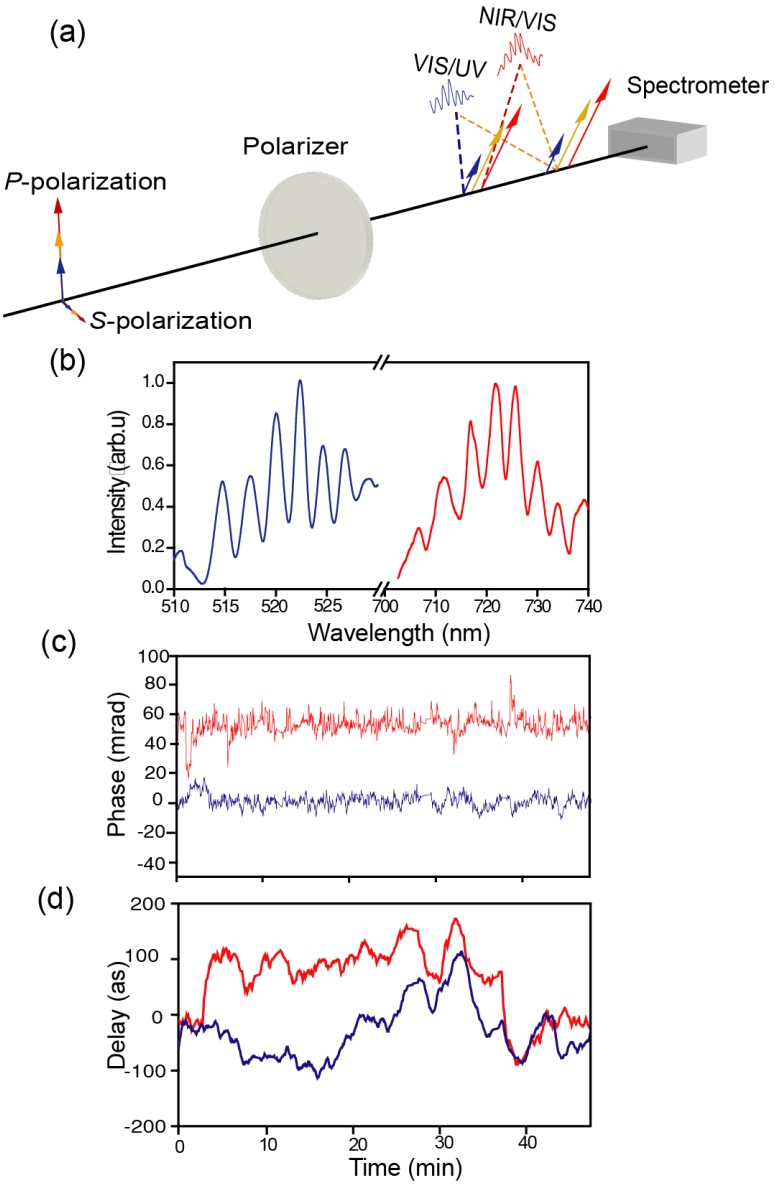

Figure 4-11: Active interferometric stabilization of the three-channel synthesizer. (a) The active stabilization setup, A Glan-Thomson polarizer adjusts the relative amplitude of P and S polarized spectral components to generate spectral interference fringes recorded by the fiber spectrometer. (b) Interference fringes between ChVis-UV and ChVis (blue line) channels as well as ChVis and ChNIR (red line) when the constituent pulses of the synthesizer are temporally overlapped at the exit of the synthesizer. (c) Phase drift between (ChVis-UV and ChVis) and (ChVis and ChNIR) with the feedback loop turned on. (d) Corresponding delay compensated for by adjustment of the optical path in ChVis-UV and ChNIR to yield the results of (c) (illustration is taken from [70]).

To detect spectral interference and to trace the relative delay between the pulses in different channels, a thin pellicle is used to route a small fraction (~2.5%) of the broadband beam—through a Glan-Thomson polarizer— to the entrance of a fiber spectrometer, as shown in Figure 4-11 (a).

The Glan-Thomson polarizer projects *S* Polarized and *P* polarized components of adjacent channels on the same axis, and adjusts their relative amplitude depending on its angle; so that it can enable their spectral interference. Spectral fringes are recorded between pulses of $Ch_{Vis\text{-}UV}$ and Ch_{Vis}, as well as Ch_{Vis} and Ch_{NIR}, as shown in Figure 4-11 (b). Once the two beams are brought into interference, spectral interferometry can be used to derive the relative delays between pulses in adjacent channels. In order to compensate for the detected drifts in the optical paths among different channels, a computer program is used to analyze spectra in real-time, such as those of Figure 4-11 (b). They, accordingly, adjust the position of the piezoelectric translational stage in each channel such that they stabilize their relative optical length. Under active stabilization scheme on, the phase drift between pulses in $Ch_{Vis\text{-}UV}$ and Ch_{Vis} as well as pulses in Ch_{Vis} and Ch_{NIR} are shown in Figure 4-11 (c) over a period of ~1 hour, and the standard deviation of the phase drift between $Ch_{Vis\text{-}UV}$ and Ch_{Vis} is $\sim\pi/30$, and that between Ch_{Vis} and Ch_{NIR} is $\sim \pi/60$.

Chapter 5

Synthesized light transients

The demonstration of field synthesis is only complete by the sampling of the synthesized transients. In this thesis work, attosecond streaking technique [105-107] has been utilized for sampling the synthesized transients, which gives an access to the field of the synthesized waveform. For this sampling technique, the generation of isolated attosecond pulse is essential. The sampling takes place at the focus of these transients where the planned experiment takes place in order to attain high intensities, as we will explain in chapter 7. Other important reasons are; superoctave light transients are very sensitive for the propagation through dispersive media and/or wavefront shaping elements. For instance, propagation through length of 10 cm in air is sufficient to induce a relative delay of ~7 fs between pulses of $Ch_{Vis\text{-}UV}$ and Ch_{NIR}. Such a delay is detrimental for the temporal profile of these transients. Moreover, the focusing of a polychromatic field will still result in complex spatiotemporal transformations of the waveform, due to the frequency dependence of the Gouy phase shift. In this chapter the generation, sampling, and synthesise of sub-optical-cycle light field transients with attosecond resolution will be demonstrated.

5.1 Generation of isolated EUV pulse and sampling apparatus setup

The isolated EUV attosecond pulse is generated following the principles discussed in Chapter 2. In these experiments, this is attained by focusing (f~ -40 cm) the light transients generated at the exit of the synthesizer apparatus into a quasi-static gas cell, a thin nickel tube (~2mm inner diameter), filled with neon gas and kept

at a constant backing pressure of ~230 mbar. For quasi-static gas cell, the tube diameter can be chosen so as to maximise the EUV photon flux in the spectral range 70–130eV. The experimental setup, discussed henceforth, and as shown in Figure 5-1, is fully realised in a vacuum [102, 108] in which the synthesized transients enter through a 0.5 mm thin UV-grade fused silica Brewster window. An ionization-based detector for the EUV flux (HH-Meter) is implemented after 10 cm of the quasi-static gas cell. It collects the charged fragments that are liberated by ionization of the residual gas providing a rough, but extremely useful detector for the EUV flux. The signal of the HH-Meter also acts as a sensitive indicator of the temporal synchronisation of the synthesizer's pulses. The EUV radiation flux can be maximised by fine-tuning the relative delay between the channels. To this end, a CCD camera placed downstream the EUV source, is used to record the flux and the profile of EUV radiation transmitted through an approximately ~1 μm thick Zirconium (Zr) foil. The Zr foil allows the transmission of photons with energies exceeding ~ 70 eV up to the cut-off energy.

Moreover, the signal of the HH-meter and its stability reflects also the stability conditions of the source which is better than 2.5 % (standard deviation/mean value). Nearly diffraction-limited EUV beams are emerging collinearly to the driving radiation (due to the short wavelength of the generated light), together with its high degree of coherence are transmitted through a disc-like Zirconium (Zr) foil (thickness of 150 nm) mounted on a thin nitrocellulose pellicle (~15 μm). The nitrocellulose pellicle absorbs the UV photons and burns after one hour of illumination. These causes reduce in intensity and profile distortion for the beam. Eventually, the nitrocellulose pellicle is replaced by double tungsten wire to hold the Zr-filter, as shown in Figure 5-1 (b). This can stand for weeks and allow for having the same synthesized light transient on the sampling and experiment point for a long period of time. The driving radiation travels through the gas cell is transmitted around the margins of the Zr disc to create an annular beam. The beam profiles of the three channels pulses are not affected by these wires.

The multilayer coated mirror, together with the high pass Zr filter, comprise a band pass filter of width $\Delta E \sim 13 eV$ centred at $E_0 \sim 85 eV$, leading the isolation of a single attosecond pulse [8, 23].

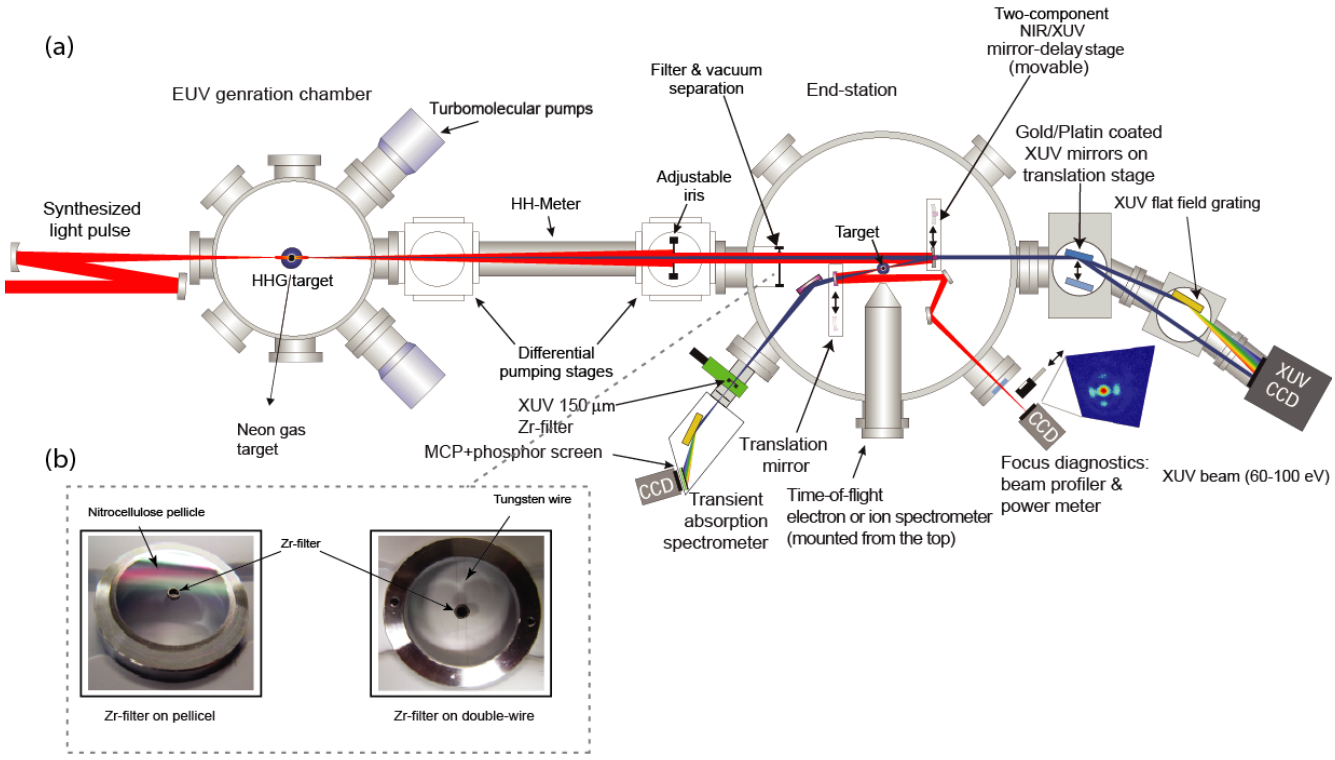

Figure 5-1: (a) Apparatus for sampling the synthesized field transients and attosecond pump-probe experiments. The schematic displays the three main parts in the apparatus; (i) EUV generation chamber, (ii) differential pumping stage, and (iii) End-station, as explained in the text (b) photo shows The Zr-filter stands on thin pellicle of nitrocellulose or on double-wire (illustration is adapted from[108]).

The setup of the apparatus for sampling the synthesized field transients and atto-second pump-probe experiments is schematically shown in Figure 5-1 (a). The apparatus consists of three main parts; (a) EUV generator chamber, where the generation of EUV attosecond pulses takes place. (b) Differential pumping stage; where the separation between synthesized transient and EUV based on the differ-ence in the divergence between the two beams and a special pellicle filter takes

place. Adjustable iris has been implemented in this stage to adjust the power of the synthesized transient pulses. (c) End-station, this consists of; a two-component delay mirror module, it contains a multilayer mirror attached to a piezo stage and an outer mirror, this module introduces a delay between synthesized transient and EUV pulses and focuses both beams into the experiment target. Diagnostic tools performing attosecond streaking as the TOF spectrometer and a EUV sensitive camera are used to characterize the EUV beam profile (60-120 eV). Also, an imaging system including triple-lens and CCD camera is installed to image the synthesized transient beam profile on the experiment target. On the other hand, a high resolution-McPherson spectrometer which used in the experiments is attached to the end-station chamber.

5.2 Attosecond streaking of the synthesized light transients

The attosecond streaking setup is schematically illustrated in Figure 5-2(a). After being transmitted through a disc-like Zirconium, both the light transients and the generated EUV beams are focused utilizing a module comprised of a concave, multilayer coated inner mirror and an aluminium coated concave annular sector (outer mirror) of the same focal length (f = -12.5 cm), respectively, into a second neon gas nozzle. The second neon gas nozzle is placed underneath a Time-Of-Flight (TOF) electron spectrometer with a spectral resolution better than 1% of the electron kinetic energy which is used to collect electrons released along the EUV pulse polarization vector [77].

In the TOF spectrometer [109], the electrons pass a magnetic shielded drift tube, which at the end of this tube undergo acceleration. This post acceleration ensures a uniform response of the Micro-Channel Plates (MCP), irrespective of the electrons kinetic energy. At the entrance of the TOF, an electrostatic lens increases the acceptance angle of electrons within a certain range of kinetic energies. The measured signal at the MCP is digitised using a multi-scale card with a minimal time discrimination of 250 ps.

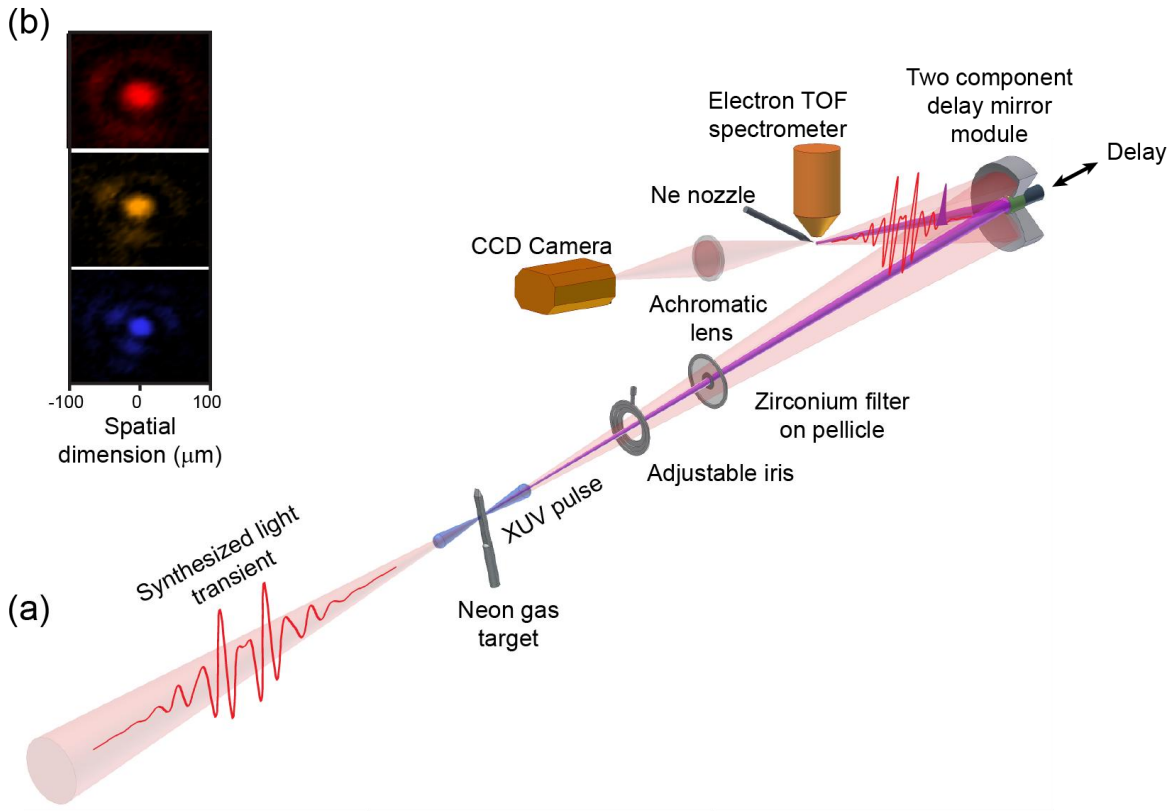

Figure 5-2: Sampling of the synthesized light transients. (a) Schematic diagram of the experimental setup for sampling synthesized light field transients. (b) The beam profiles of the constituent channels on the focal plane (illustration is adapted from [70]).

The electron TOF scheme typically yields on a count per laser pulse within the experimental bandwidth, using neon as a target gas. The inner-mirror is attached to a piezoelectric stage that allows the introduction of a delay between the light field transient and the EUV attosecond pulse with nanometric precision. A set of electron TOF spectra are rerecorded over a range of delays between the light field transient and the EUV attosecond pulse with 200 as delay step. The temporal evolution of the laser electric field (more precisely, it's associated vector potential) can be retrieved from the "Streaking spectrogram" [5, 7, 8, 72]. The ATTOGRAM algorithm has been used to reconstruct temporal structure of the attosecond pulse, including its temporal and spectral phase, as shown in Figure 5-3.

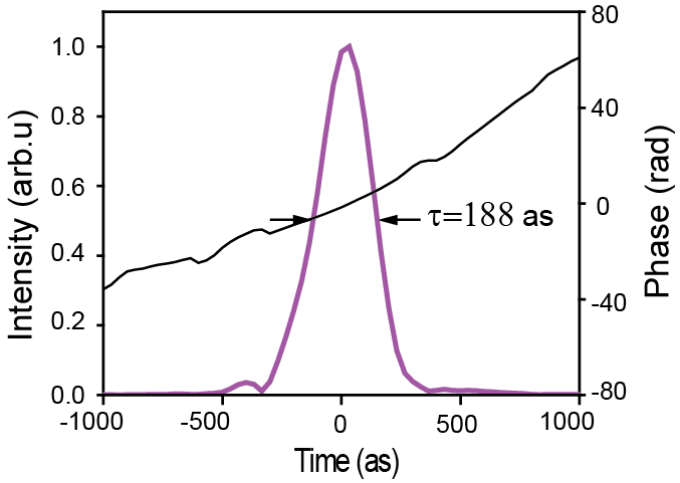

Figure 5-3: Temporal profile of a EUV attosecond pulse carried at ~ 85 eV (illustration is taken from [70]).

A controllable motorized iris is used to adjust the energy transported by the beam of the light transient from the level of few microjoules (adequate for streaking) to that of several tens of microjoules for strong field attosecond experiments, which will be demonstrated later, offering a dynamic range over several orders of magnitude, from < 10^{12} W/cm^2 to ~ 10^{15}W/cm^2. Streaking measurements are typically performed at intensities of the order of 10^{13} W/cm^2.

The profiles of the beams of the four channels at the place of characterization are monitored by imaging the focus on a CCD camera through a broadband achromatic lens. Figure 5-2(b) shows representative beam profiles of the constituent channels on the focal plane of the double mirror module on which synthesis and temporal characterization of light transients are performed.

5.3 Subcycle light field transients

The three-channel synthesizer provides the ability to compress the 1.5-octave coherent radiation close to its Fourier limit. In the three-channel synthesizer, the three bands coherently superimpose to generate a "subcycle" light field transients[77]. These transients encompass only 0.88 cycles within the FWHM of their intensity profile. The term "subcycle" implies a comparison between a pulse's widths with respect to the period of its carrier wave. A carrier wavelength of this pulse $\lambda_C = 710\,nm$ corresponds to an oscillation period of $T_C = 2.34\ fs$ estimated by the weighted averaged wavelength derived from the spectrum which is directly measured at the exit of the synthesizer. The subcycle field transient is sampled and the streaking spectrogram has been recorded (Figure 5-4(a)). The electric field and the intensity envelope of the subcycle transients are shown in Figure 5-4(b) and (c), respectively. The analysis yields a FWHM pulse duration of ~ 2.08 fs (in intensity). The blue line in Figure 5-4(c) corresponds to the Fourier limited intensity profile. The difference between the two profiles may come from unperfected compression of the individual constituent channels.

5.4 The stability and reproducibility if the synthesized transient fields

The stability and the reproducibility of the synthesized transients are essential in the field synthesis. In that spirit, we investigate the stability and the reproducibility of the synthesized transients by recording a series of streaking spectrograms over long time periods[77]. The first sampled attosecond streaking spectrogram is shown in Figure 5-5 (a) and is followed by two additional spectrograms shown in Figure 5-5 (b) & (c), the total acquisition time is > 1 h. For accurate comparison, the three retrieved electric fields for the pervious spectrograms are plotted in the same graph in Figure 5-5 (d).The rms field difference [110] between these transients is only 0.09 on a ±15 fs window. One can conclude that, the waveform of synthesized transients is exceptionally stable and reproducible for long periods of time.

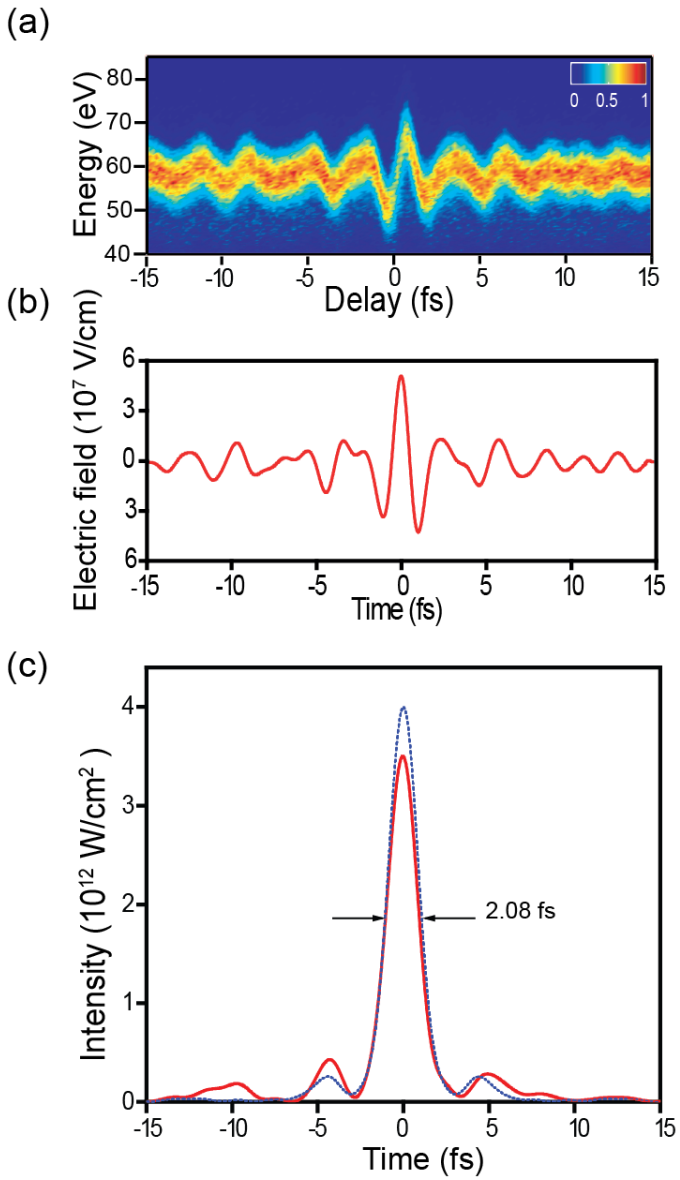

Figure 5-4: Subcycle light transient (a) Attosecond streaking spectrogram (b) The retrieved electric field and (c) Temporal intensity profile (red) of subcycle pulse with a τ_{FWHM} ~ 2.08 fs, compared to the bandwidth limited profile (blue) (illustration is taken from [70]).

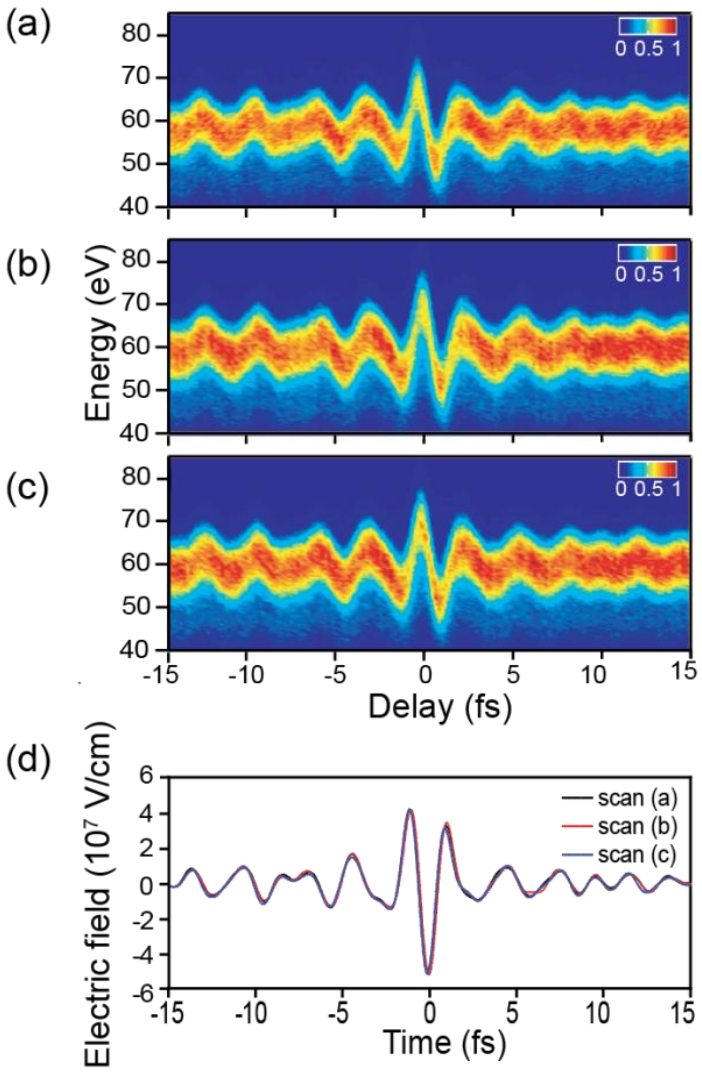

Figure 5-5: demonstration the stability of synthesized light transient generation. From (a) to (c), show the streaking spectrograms of a synthesized light transient sampled sequentially over a period of > 1 hour. (d) The corresponding retrieved electric fields of the waveforms in comparison (illustration is taken from [70]).

5.5 Tailoring of light field transients

Here, is discussed the issue of on demand synthesis of light transients [77]. Each recorded light transient can be considered as a reference to access the detailed properties of the constituent channels at a certain time; band-pass filtering is constrained to the spectral margins of each channel and is performed for the reference waveform to investigate the pulse properties in each individual channel, and their relative phases (or delays). Some of the pulse properties of the individual channels extracted via this methodology ($\tau_{Ch(NIR)}$ = 7.3 fs, $\tau_{Ch(Vis)}$ = 5.5 fs, and $\tau_{Ch(Vis\text{-}UV)}$ = 4.5) agree well with those retrieved with the FROG measurements, as demonstrated in Chapter 4.

Having the access and the control on this parameter, especially the relative phases, enable one, by changing one of these parameters, to compose a desired waveform. For instance, the waveform, shown in Figure 5-6 (b), is retrieved from the measured streaking spectrogram (Figure 5-6 (a)). It is considered as reference waveform. The pulse properties of the constituent three channels of the light field synthesizer are extracted as shown in Figure 5-6 (c). By changing the relative phases between the individual channels (Figure 5-6 (d)), one can reach the predicted waveform, which is shown in Figure 5-6 (e).

5.6 Subcycle light field synthesis

The ability of subcycle control of the light transient's span over more than the 1.5-octave is demonstrated in Figure 5-7 and Figure 5-8, by changing the relative phase delay of $Ch_{Vis\text{-}UV}$ and Ch_{NIR}, respectively [77]. In both figures, the electric fields are represented by showing the red lines in the middle column. Black lines in the middle represent the simulated predicted waveforms calculated from the reference waveform by applying a corresponding delay as explained in (5.5). The instantaneous intensities are represented in the right column. They are derived from the corresponding streaking spectrograms represented in left column.

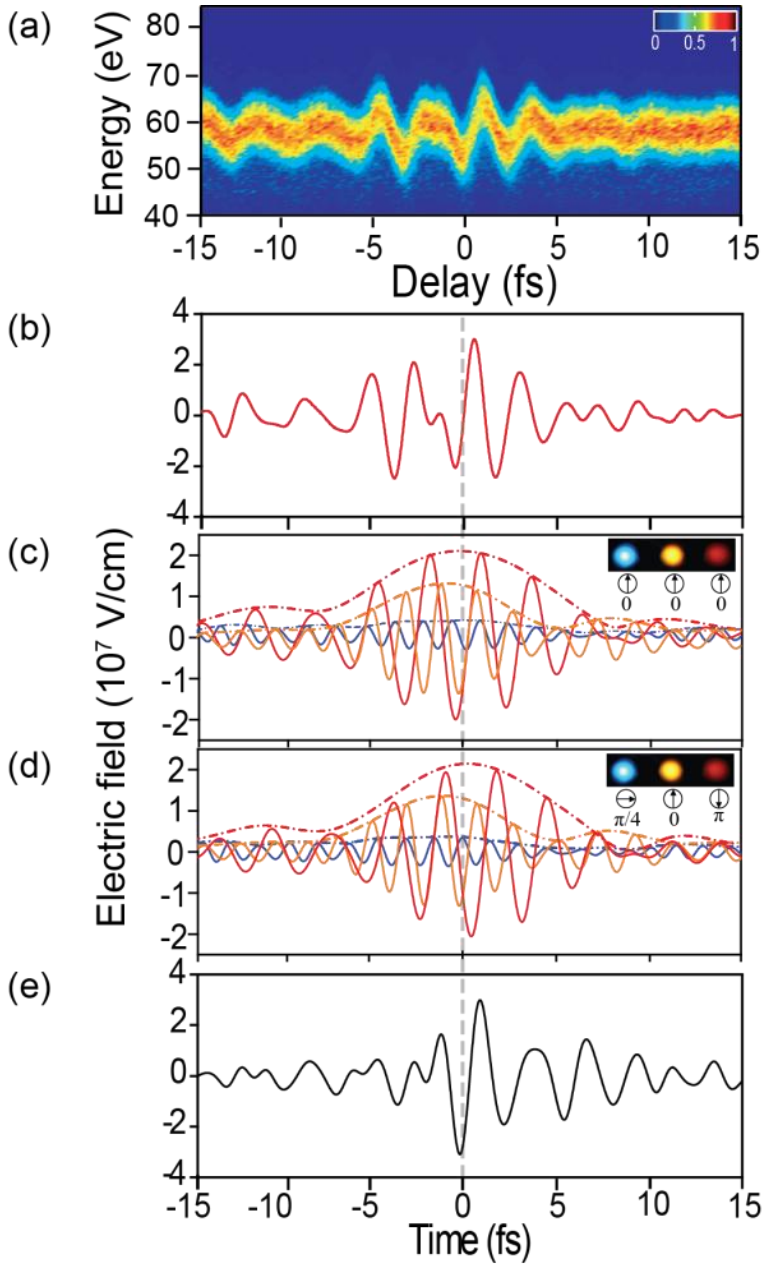

Figure 5-6: Designing a light transient. (a) Attosecond streaking spectrogram of a reference transient and (b) its corresponding retrieved field. Decomposition of the retrieved field into its constituent channels (c). By changing the relative phases of ChVis-UV by $\pi/2$ and of ChNIR by π in (d), one can generate the designed waveform in (e) (illustration is taken from [70]).

In Figure 5-7, the light transient, in Figure 5-7 (a), is considered as a reference. Field transients in Figure 5-7 (b) and (c) are synthesized by delaying $Ch_{Vis\text{-}UV}$ in steps of $\pi/4$ (~ 200 as) with respect to the reference waveform in Figure 5-7 (a). Delaying $Ch_{Vis\text{-}UV}$ gradually transforms the field into the highly asymmetric transient (Figure 5-7 (c)). This transient is led by its most intense half-cycle, followed by field crests with a gradually decreasing intensity giving rise to a transient having a leading edge of a sub-fs rise time. The field transient in Figure 5-7 (d) is generated by delaying $Ch_{Vis\text{-}UV}$ by $-\pi/2$ to reproduce the reference waveform in Figure 5-7 (a).

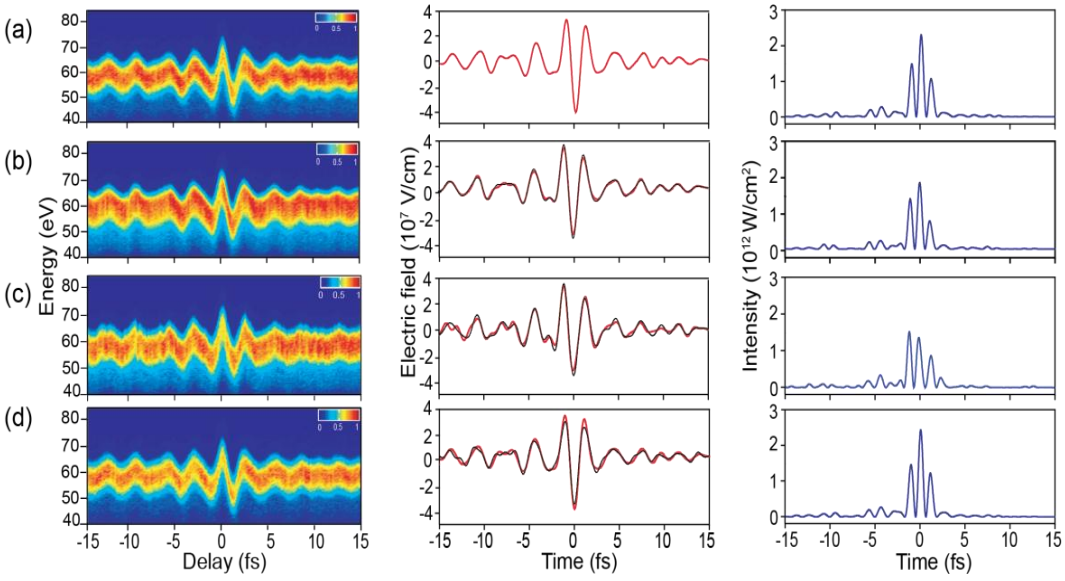

Figure 5-7: Light field synthesis with attosecond resolution. Attosecond streaking spectrograms composed by photoelectron spectra normalized to their integral (left), the respective retrieved electric fields (red line) and the predicted field transients calculated from the previous light transient by applying the delay introduced experimentally (black line) in the (middle) and instantaneous intensity (right). (a) The reference field transient, by delaying $Ch_{Vis\text{-}UV}$ by $\pi/4$ leads to generating the light transient in (b). Another delay step by $\pi/4$ generates the asymmetric transient which led by its most intense half-cycle in (c). Resetting the relative phases similar to the reference light transient in (a) (illustration is adapted from [70]).

Complex light field synthesis is demonstrated in Figure 5-8. The nonsinusoidal transient is generated by adjusting the CEP phases of all channels and the delay of Ch_{NIR} such that the fields of the three constituent channels cancel each other at the center of the synthesized waveform (Figure 5-8(a)). Adjusting the delay of Ch_{NIR} by $\sim\pi$ generates a transient of subcycle temporal confinement (Figure 5-8 (b)). The complex light transient is regenerated by delaying Ch_{NIR} by $\sim -\pi/2$ in two step; Firstly, one can create the light transient shown in Figure 5-8 (c), and secondly, the complex waveform in Figure 5-8 (d) is created, for this light transient, in the instantaneous intensity the two most intense field crests of which are separated by ~4.5 fs and a virtually annihilated by a half cycle in its middle.

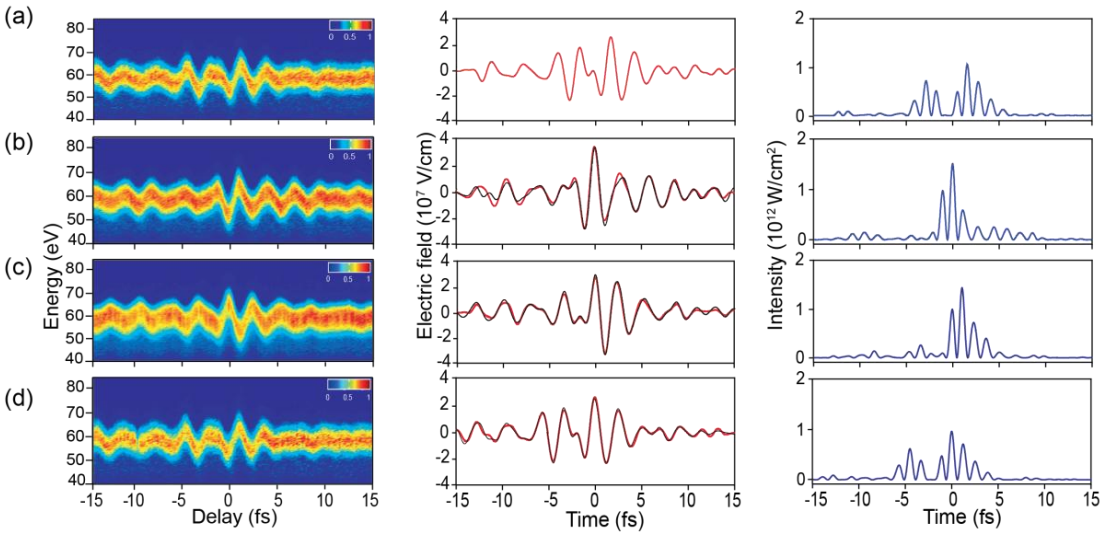

Figure 5-8: Light field synthesis for complex light transients. Relative delays and CEPs of the individual channels are adjusted so as to create a complex nonsinusoidal transient with a field minimum in between them is present in (a). Tuning the delay of Ch_{NIR} by $\sim\pi$ led to create the subcycle transient pulse in (b). The complex light transient in (d) regenerated in two step by delaying Ch_{NIR} by $\sim -\pi/2$ and create the transient in (c) followed by another $\sim -\pi/2$ step. In the instantaneous intensity of (d) it shows the two most intense field crests are separated by ~4.5fs (illustration is adapted from [70]).

Chapter 6

Attosecond light transients

The generation of isolated EUV attosecond pulse has been demonstrated for the first time in the beginning of the last decade [5, 111]. The EUV attosecond pulse generation is relying on the high harmonic generation technique detailed in the previous chapters. Although, the EUV attosecond pulses are essential important tools for studying and controlling the motion of electrons inside atoms, the very low efficiency of generated the EUV attosecond limits using of this pulse in pump-probe experiment. Therefore, the generation of the attosecond pulse in the optical domain can advance attosecond science to a new realm.

In this thesis work, the generation of "attosecond light transients" (ALTs), is demonstrated for the first time. Moreover, the advances in light synthesis that have allowed attaining this challenging goal such as extending the prototype synthesizer to the DUV spectral region, and the low dispersion control of the supercontinuum that spans over 2-octaves are explained.

6.1 From subcycle to attosecond light transients

Earlier in this work the ability of control light transients extend over 1.5-octaves which leads to subcycle light control has been demonstrated. The light field control can be extended to 2-octaves covering the NIR, the Visible, UV and Deep-Ultra-Violet (DUV) part of the spectrum by adding additional band towards the UV side of the prototype synthesizer and executing phase and amplitude control of the synthesized waveform. Figure 6-1 shows the simulated light transient that can be composed by amplitude and phase control over a two-octave spectrum

spanning from 260 nm to 1110 nm. The τ_{FWHM} confinement of the main field crest is in sub-femtosecond time scale since the synthesis is performed in the optical frequencies. This is what we called "Attosecond light transients" (ALTs).

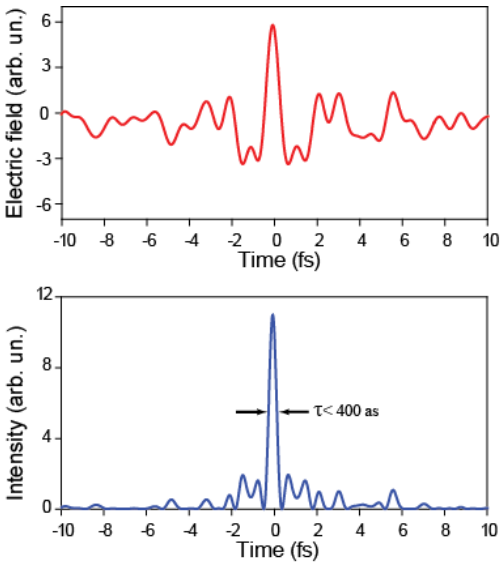

Figure 6-1: Simulated attosecond light transients for a broadband 2-octave spectrum from 280-1100 nm. The simulated light transient can be generated by proper adjustment of the relative intensity and phase the constituent channels of the four-channel synthesizer. In lower panel the simulated electric field, and in upper part the instantaneous intensity, the main field crest has contrast >5 times side crests. The FWHM duration of this main field crest is < 500 as.

6.2 2-Octave light field synthesis

Scaling up the synthesizer to four channels has been attained by the implementation of more spectral channel (Ch_{DUV}) in the DUV region. For generating the required 2-octave, the seeded pulse power into the hollow core fiber has been increased to ~900 μJ, and the Ne gas pressure inside the hollow core waveguide has been adjusted (~1.5-2 bar) to optimize the broadening. Critically, the duration of the input pulse has been reduced to ~22fs. The 2-octave (230-1100 nm) supercontinuum has been generated as shown in Figure 6-2. The power of the supercontinuum at the exit of the HCF is ~ 550 μJ.

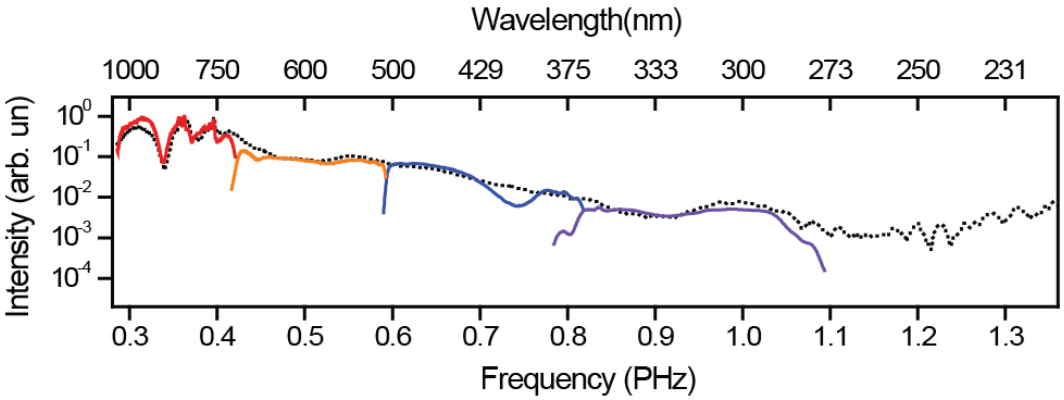

Figure 6-2: Supercontinuum generation in a Ne-filled hollow-core fiber pressurised at ~1.7bar, seeded by 22 fs pulse carried at centre wavelength 790 nm with ~ 1 mJ spanning from NIR to DUV (230-1100nm). The individual spectral bands of the four-channel light field synthesizer are measured.

6.2.1 Efficient transportation of the supercontinuum

Transportation of the UV component of the generated supercontinuum is very essential for scaling up the synthesizer. The supercontinuum beam cannot be transported utilizing the silver-coated mirror as in case of 1.5-octave supercontinuum since the reflectivity of these mirrors dropped to zero at the spectral region less than 350nm.

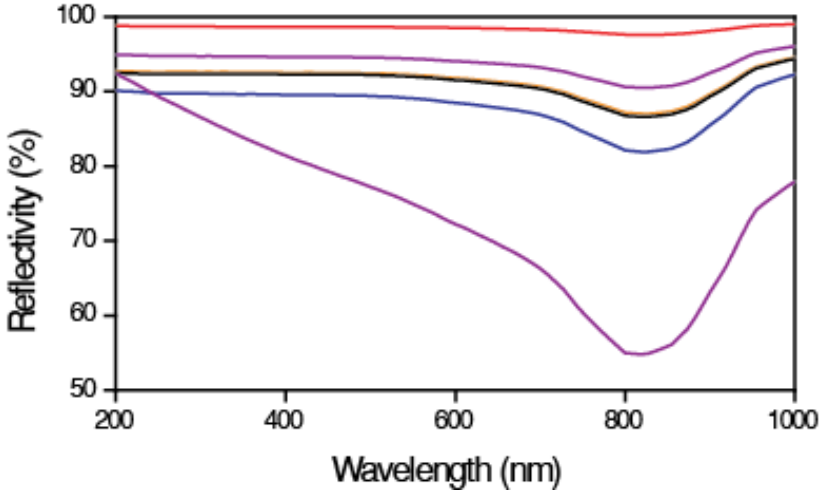

Figure 6-3: Reflectivity of an-aluminium coated reflector at different incident angles and polarizations. The reflectivity for *s* polarized light at (80°, 45° and 10°) of incident angle is represented in red, blue, and black lines, respectively. The reflectivity of aluminium coated mirror for *p* polarized light at (80°, 45° and 10°) of incident angle are represented in violet, magenta and orange lines, respectively.

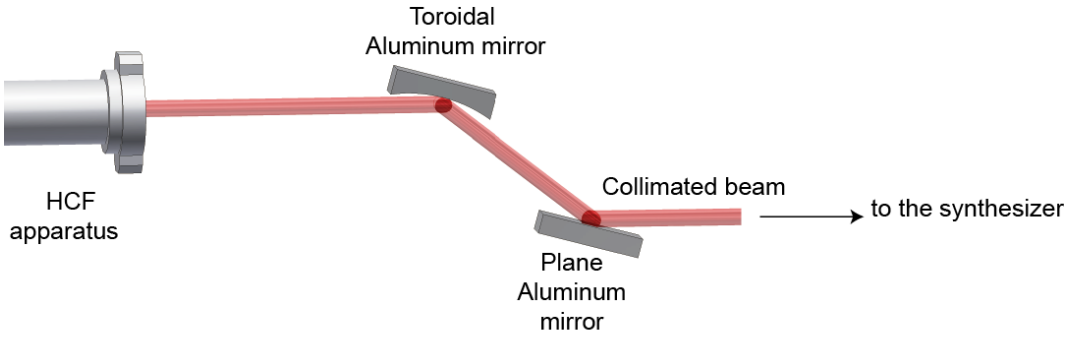

Figure 6-4: Quasi-grazing incident set up for transporting the 2-octave supercontinuum spans NIR, visible and DUV.

For that, aluminium- coated mirrors have been chosen. It supports the reflectivity from less than 200 nm to more than 1100 nm. Fortunately, the average reflectivity of this mirror is ~ 94% at the spectral region from 200-700 nm, however, it drops to ~ 80 % at the NIR region (800-1100nm) at 45º reflective angle for *P*-polarized light, as shown in Figure 6-3. The 2-octaves coherent light is transported from the source (HCF) to the synthesizer and from the synthesizer to the experiment target by seven aluminium reflectors (three reflectors at 45º and four reflectors at 10 º incident angle). This reflectivity reduces the power by 60%.

To overcome this loss in power, grazing incident setup was chosen, schematically illustrated in Figure 6-4. Toroidal, aluminium-coated, mirror with a focal length ~75 cm, and a rectangular plane, aluminium –coated, mirror at grazing incident, have been used, instead of the 4 reflectors at 80º incident angle to collimate the output beam from the fiber waveguide, to have ~8mm beam size. The loss in the power regarding the transporting of the supercontinuum from the HCF to the synthesizer and from the synthesizer to the experiment's target decreased to ~ 40%.

6.2.2 Four-channel light field synthesizer

The implementation of the Ch_{DUV} has been done in many steps; first, a dichroic beam splitter $DBS_{DUV/Vis}$ has been designed to reflect the light from (280-350 nm) and transmit the rest of the supercontinuum. The reflectivity design of this beamsplitter is shown in Figure 6-5 (a). Second, aluminium-coated mirrors (six mirrors) have been placed in the positions of the chirped mirrors of this channel. The spectral phase, introduced by propagation through air or dispersive material (i.e. the 0.5 mm fused silica of the exit window of HCF and 0.5 mm fused silica of the entrance window of the experimental chamber), of the Ch_{DUV} has been retrieved from the measured FROG spectrogram of the Ch_{DUV} pulse.

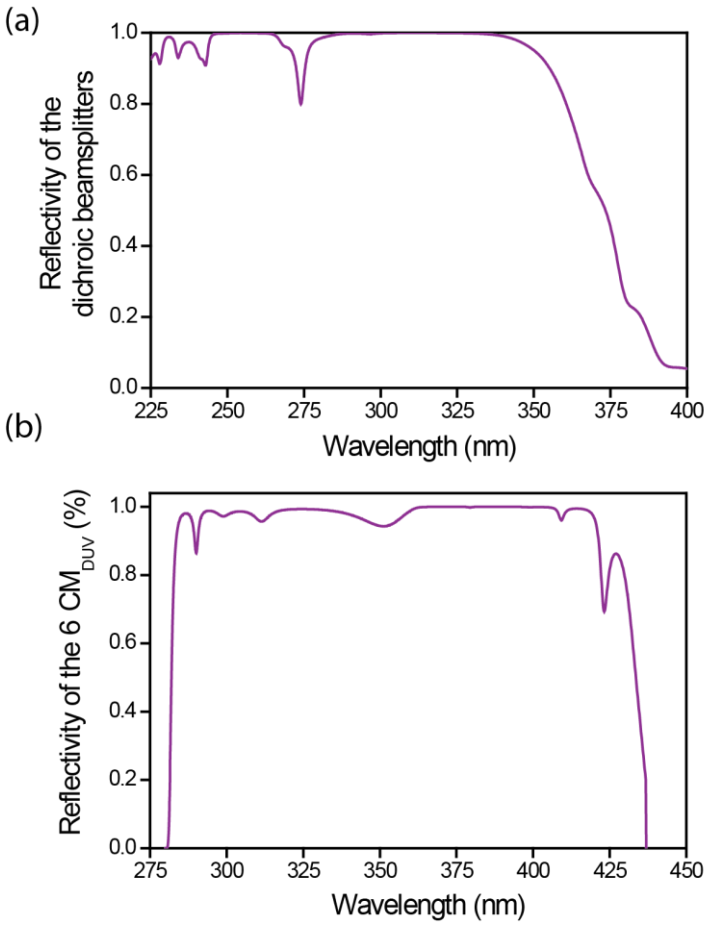

Figure 6-5: Designed reflectivity of Ch_{DUV} optics (a) for the dichroic beamsplitter $DBS_{DUV-Vis}$ and (b) for the chirped mirrors CM_{DUV}.

The pulse of Ch_{DUV} before compression is shown in Figure 6-6. The group-delay dispersion (GDD) of the Ch_{DUV} pulse (Figure 6-7 (a)) is calculated from measured spectral phase. The chirped mirror has been designed to compensate this measured dispersion. This chirped mirror is able to compensate 60 ~ fs^2 per reflection. The designed reflectivty of this chriped mirror is shown in Figure 6-5 (b).

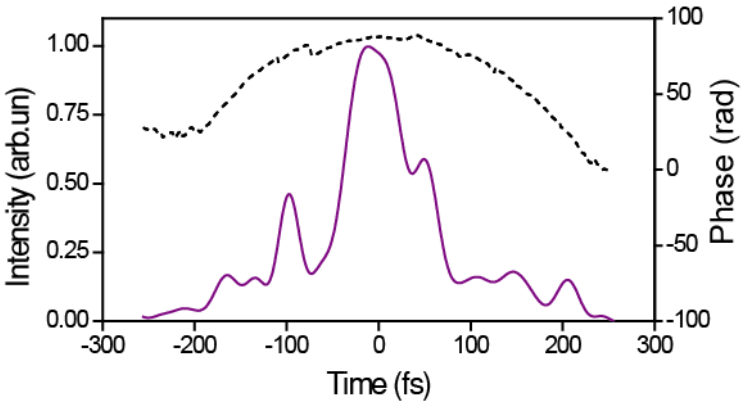

Figure 6-6: Uncompressed pulse of Ch_{DUV}.

The design strategy of the prototype synthesizer is based on the principle of separating the channel with higher frequency first, so by implementing the $DBS_{UV/Vis}$, the pulse of the Ch_{DUV} separates first. Implementation of $DBS_{UV\text{-}Vis}$ (2mm at 45º) increases the dispersion for the $Ch_{Vis\text{-}UV}$, Ch_{Vis} and Ch_{NIR} Pulses. For Ch_{NIR} Pulse, this has been compensated by adjusting the thickness of the pair of wedges in the path of this channel. However, this introduced dispersion cannot be compensated by adjusting the wedges thickness for $Ch_{Vis\text{-}UV}$ and Ch_{Vis} pulses. The design of a new CM_{Vis} and $CM_{Vis\text{-}UV}$ became obligatory. The new dispersion for the Ch_{Vis} and $Ch_{Vis\text{-}UV}$ pulses has been measured by the same method as in the case of the $Ch_{DUV.}$ The GDD of $Ch_{Vis\text{-}UV}$ and the Ch_{Vis} pulses are shown in Figure 6-7 (c) and (d), respectively. These have been calculated from the measured spectral phases and have been used as a target for designing new dispersive mirrors for these channels. The dispersion compensation of the new $CM_{Vis\text{-}UV}$ and CM_{Vis} mirrors is ~ 80 fs^2 and 75 fs^2 per reflection respectively.

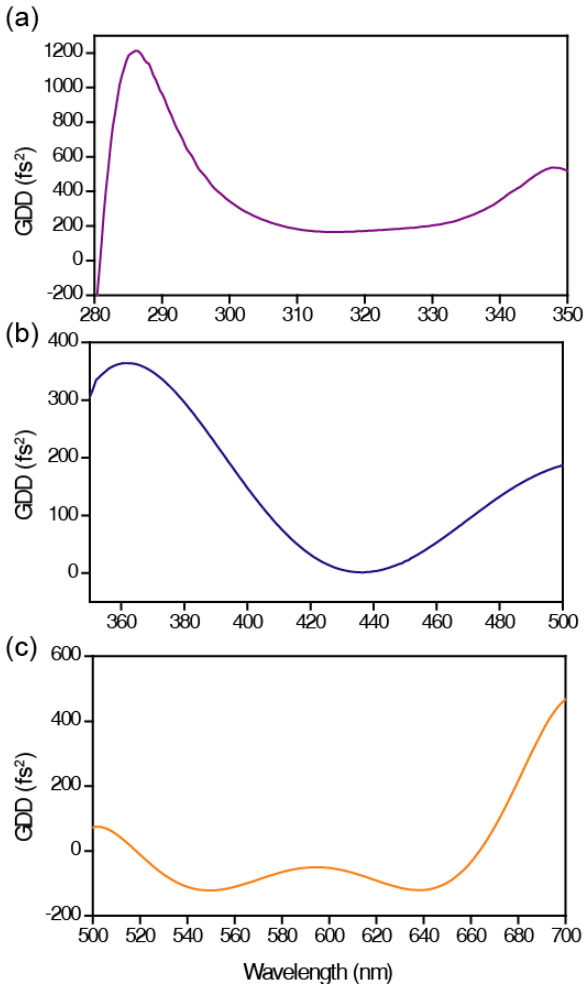

Figure 6-7: Group-delay dispersion (GDD) of (a) $Ch_{DUV,}$ (b) Ch_{Vis-UV} and (c) Ch_{Vis} , extracted from the measured spectral phases of these channels.

The four-channel synthesizer, shown in Figure 6-8, has a total transmission of about 82%. The transmission per optical channel is Ch_{NIR}~85%, Ch_{Vis} ~75%, Ch_{Vis-UV} ~60%, and Ch_{DUV} ~ 55%. The synthesized waveform at the exit of the synthesizer carry an energy of ~320 µJ distributed among the four channels as Ch_{NIR}~255 µJ, Ch_{Vis}~45 µJ, Ch_{Vis-UV}~15 µJ, and Ch_{DUV} ~4 µJ. As in the case of Ch_{Vis-UV} and Ch_{NIR}, the translation unit consists of manually adjustable translation stage and a piezoelectric translational stage are implemented in the beam path of the Ch_{DUV}.

(a)

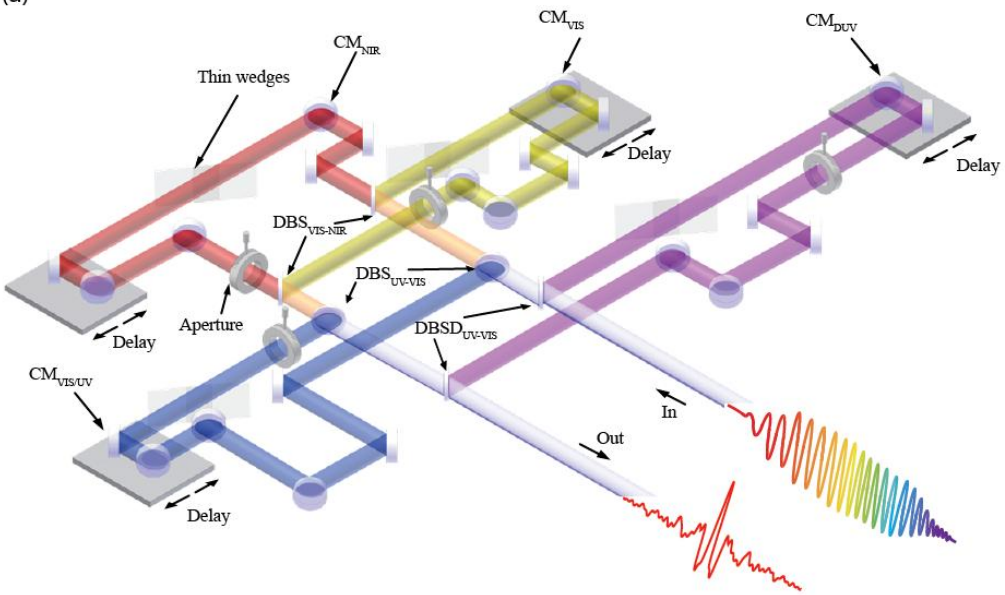

(b)

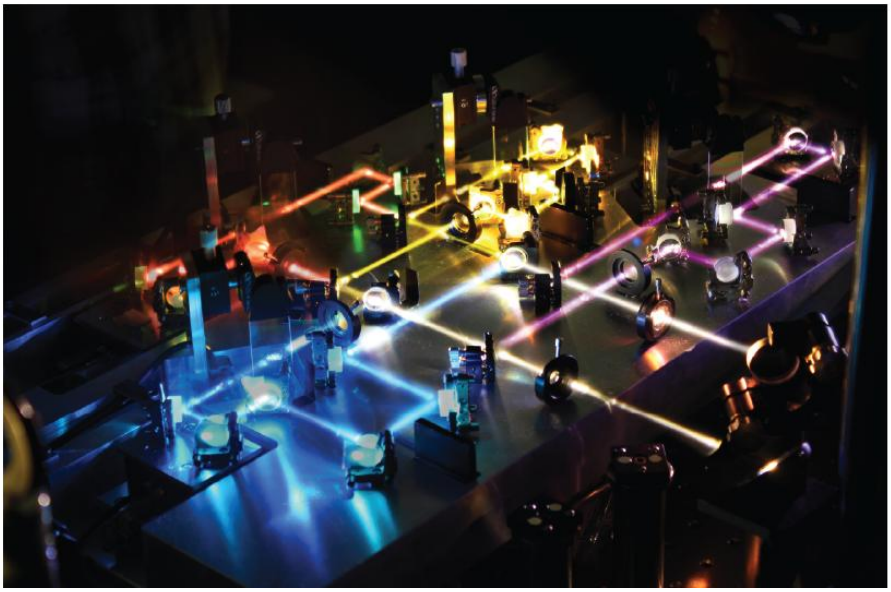

Figure 6-8: Four-channel light synthesizer (a) Schematic representation of a prototypical four-channel light field synthesizer. (b) Photograph (perspective) of the four-channel light field synthesizer in operation.

After the implementation of $Ch_{Vis,}$ $Ch_{Vis\text{-}UV}$ and Ch_{DUV}, FROG spectrograms for $Ch_{NIR,}$ $Ch_{Vis,}$ and $ChVis_{\text{-}UV}$ and Ch_{DUV} pulses have been measured, as depicted in Figure 6-9. The τ_{FWHM} pulse duration of the individual channel pulses are : $\tau_{Ch(NIR)}$ = 8 fs, $\tau_{Ch(Vis)}$ = 6.4 fs, and $\tau_{Ch(Vis\text{-}UV)}$ = 6.3 fs which are slightly longer than the pulse durations in case of three-channel synthesizer. These may come from the high order phases introduced from the propagation through $DBS_{UV\text{-}Vis}$ which cannot be compensated by the chirped mirrors. The pulse duration of the $Ch_{DUV,}$ $\tau_{Ch(DUV)}$ = 6.5 fs.

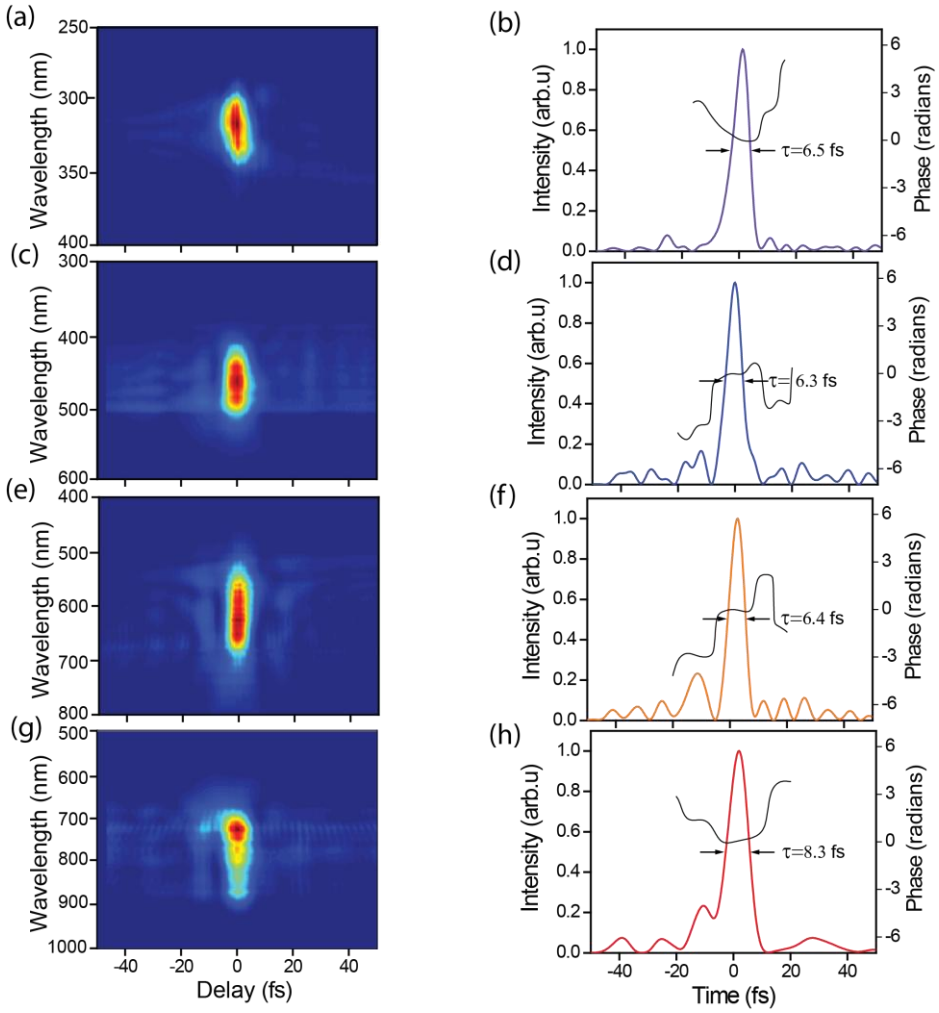

Figure 6-9: Temporal characterization for the pulses of constituent channels in the four-channel synthesizer, in the left row, the FROG spectrograms and the retrieved temporal profile, in the right row, for the constituent channels pulses.

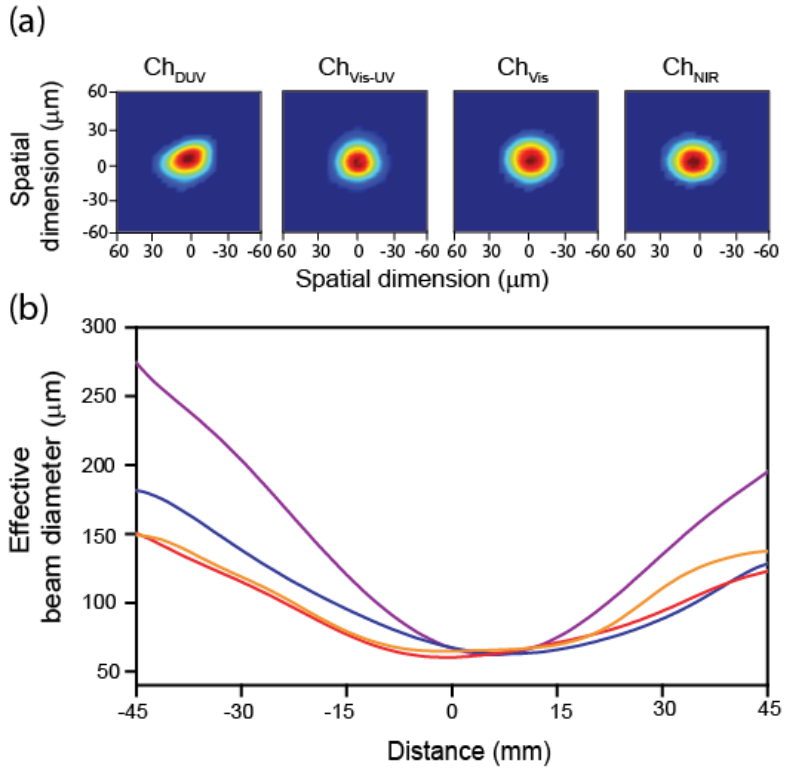

Figure 6-10: (a) Beam profiles of Ch_{DUV}, Ch_{Vis-UV}, Ch_{Vis} and Ch_{NIR} pulses at the focus.(b) Tracing the focal profile of Ch_{NIR} (red line), Ch_{Vis} (orange line) ,Ch_{Vis-UV} (blue line) and Ch_{UV} (violet line) by sampling their beam sizes through their confocal parameters.

The spatial overlap and temporal synchronisation for the constituent channels in case of the four-channel synthesizer have been performed in similar way such in the case of the three-channel synthesizer. The focal spot size of Ch_{DUV} beam is quite comparable to the other three channels (Ch_{DUV}= 60 μm) as illustrated in Figure 6-10 (a). Ch_{DUV} has also a similar divergence to the other three channels as shown in Figure 6-10(b), and no adjustable unit was needed. The temporal synchronisation for the four-channel synthesizer is performed utilizing the TG-FROG apparatus as discussed in (4.1.5.3). In this case, Ch_{Vis-UV} and Ch_{NIR} are temporally synchronized with Ch_{Vis}, and Ch_{DUV} is synchronized to Ch_{Vis-UV}.

Active stabilization in the four-channel synthesizer has been performed based on the same principle as explained in (4.1.6.2). The recorded spectral fringes between pulses of Ch_{DUV} and $Ch_{Vis\text{-}UV}$ are shown in Figure 6-11 (a). Under the stabilization scheme on, the stability of the Ch_{DUV} over a period of ~1 hour has been observed and measured. The detected phase drifts between pulses of Ch_{DUV} and $Ch_{Vis\text{-}UV}$ is shown in Figure 6-11. The standard deviation of the phase drift between Ch_{DUV} and $Ch_{Vis\text{-}UV}$ is ~ $\pi/6$ as shown in Figure 6-11 (c).

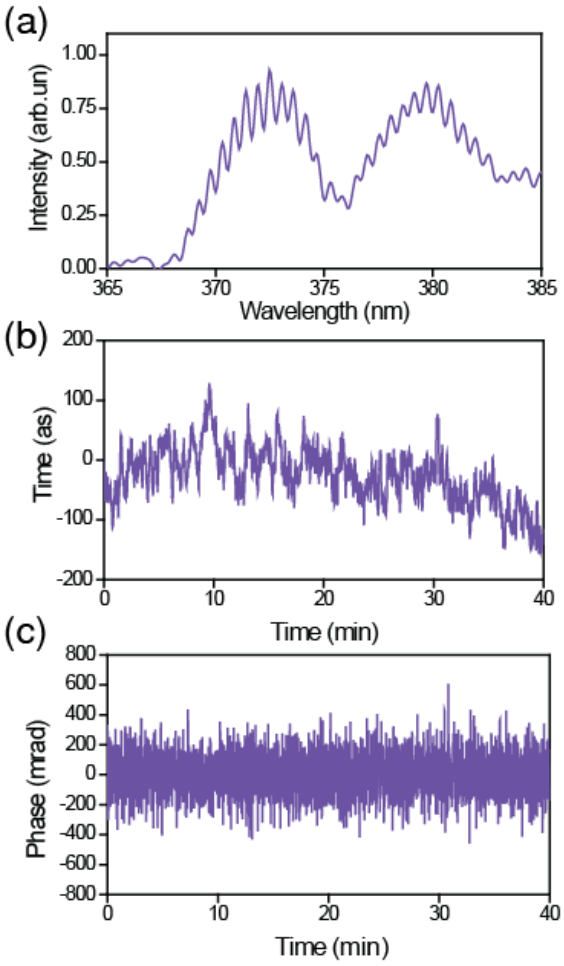

Figure 6-11: Active stabilization for the Ch_{DUV}. (a) Interference fringes between $Ch_{Vis\text{-}UV}$ and Ch_{DUV} when the constituent pulses of the synthesizer are temporally overlapped at the exit of the synthesizer. (b) Corresponding delay compensated for Ch_{DUV}. (c) Phase drift between (Ch_{DUV} and $Ch_{Vis\text{-}UV}$) with the feedback loop turned on. The standard deviation of the phase drift between Ch_{DUV} and $Ch_{Vis\text{-}UV}$ is ~ $\pi/6$.

6.3 Attosecond light transients

Under the same metrology in the four-channel synthesizer, the compression of the two octaves supercontinuum led to the generation of a light transient faster than the subcycle transient generated by the three-channel synthesizer. The subcycle transient generated by the four-channel synthesizer, carried at central wavelength $\lambda_c = 636\,\text{nm}$, has τ_{FWHM} pulse duration of ~ 1.7 fs (Figure 6-12)

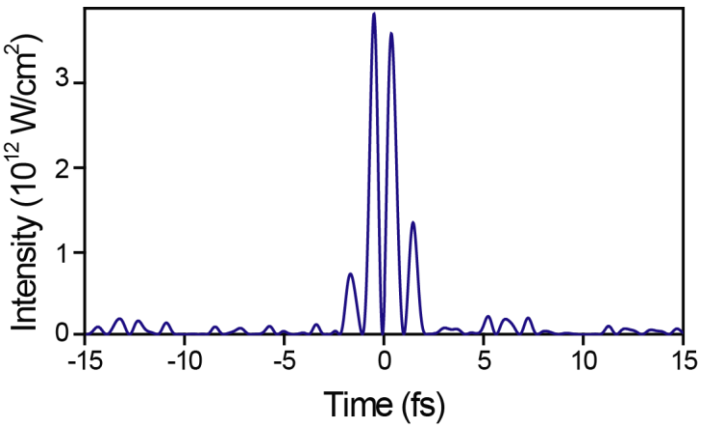

Figure 6-12: The (2-octave) subcycle light field transient.

The generation of the "Attosecond light transient" (ALT), presented in Figure 6-1, is not possible solely by controlling the relative phases but also the relative amplitude of the different spectral bands. The relative intensity ratio between the constituent channels at the exit of the synthesizer is 4% Ch_{DUV}, 10% $Ch_{UV\text{-}VIS}$, 36% Ch_{Vis}, and 50%Ch_{NIR}. However, in order to generate an attosecond light transient, as that of Figure 6-1, the relative intensity ratio should be 15% Ch_{DUV}, 10% $Ch_{UV\text{-}VIS}$, 25% Ch_{Vis} and 50% Ch_{NIR}. This can be achieved by adjusting the aperture opening introduced in the path of each individual channel or by the introduction of band pass filters; however, this will reduce the power of the transient at the exit of the synthesizer such that the generation of the attosecond EUV pulse via HHG is not possible.

For the first demonstration, the sampling of the ALTs is an essential prerequisite, and since the sampling (attosecond streaking) technique requires generating of attosecond EUV pulse the control of the relative intensity ratio between the constituent channels has to be realised after the attosecond EUV pulse generation state, that is after the EUV chamber of Figure 5-1.

6.3.1 2-octave supercontinuum amplitude control

In order to reach the desired relative intensity ratio between the constituent channels after attosecond EUV pulse generation, we opted to use metallic dichroic metallic (MDM) outer mirror instead of the metallic Al-coated outer mirror, in Figure 5-2. The basic coating design of this mirror has been demonstrated and invented in [112, 113] in order to be used as VUV filter. In this work, The MDM coating design has been optimized and tailored to our needs and it is used for the first time to control the amplitude of the 2-octave supercontinuum. The main advantage of the MDM mirror is that it does not affect the spectral phase of individual channels as it was proven by FROG measurements.

The MDM can be designed to reflect > 95% at a certain part and almost zero at another spectral part of the supercontinuum. The coating of MDM consists of four layers; a metallic reflective layer (Al, Ag and Au), a spacer layer of transparent dielectric material (SiO_2, MgF_2 and CaF_2), thin film of a heavy metal (W, Hf and Os), and finally a very thin protective layer could be added in top of the heavy metal layer. The position of the high reflectivity peak depends on the thickness of the dielectric (spacer layer), as shown in Figure 6-13 Figure 6-14(a). This figure shows the estimated reflectivity curves for two different coating designs; In coating design (A) the consequence of the layers is: Al layer (120 nm), SiO_2 layer (90 nm), Hf layer (10 nm) and protective layer of SiO_2 layer (5 nm), while in design (B) is: Al layer (120 nm), SiO_2 layer (70 nm), Hf layer (10 nm) and protective layer of SiO_2 layer (5 nm). The change in the thickness of the spacer layer changes the position of the reflectivity peak.

For coating design (A) the spacer layer thickness is (90nm) and the highest reflectivity peak centered at 275 nm. By changing the thickness of the spacer layer to (70nm) as in design (B) the highest reflectivity peak centre shifts to 335 nm. Thus, one can conclude that, by reducing the spacer layer thickness, the higher reflectivity peak is shifted to the lower frequency side, while by increasing the thickness layer, the peak is shifted to the higher frequency side.

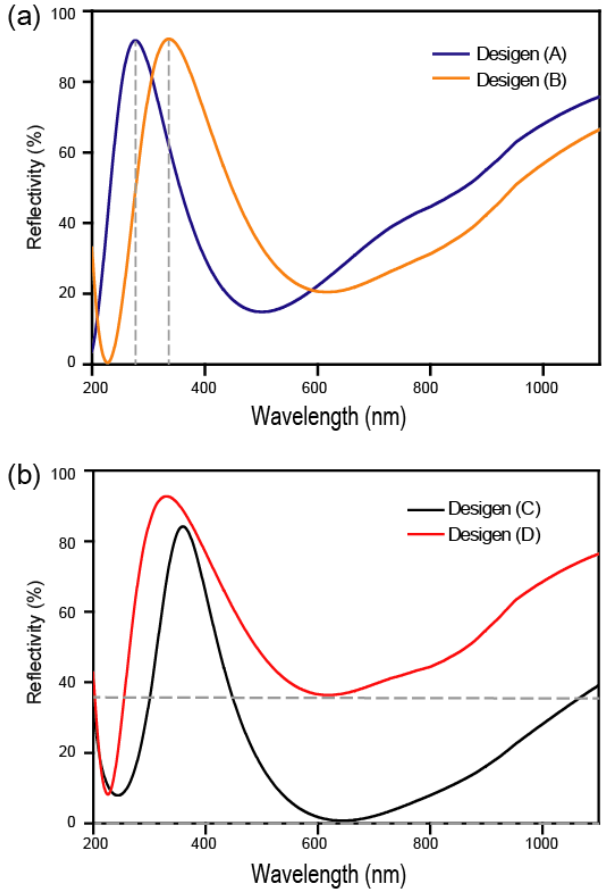

Figure 6-13: The Metallic-Dielectric-Metallic (MDM) mirror coating design. (a) The position of the high reflectivity peak depends on the thickness of the spacer layer of the dielectric material. The estimated reflectivity curve of coating design (A) is shown in blue line and for coating design (B) in orange line. The difference between these two coating designs is the spacer layer thickness, for A (~90nm) and for B (~70 nm), this causes shift in the high reflectivity peak. (B) The reflectivity contrast between high reflectivity peak and low reflectivity area depends on the thickness of the heavy metal thickness. The estimated reflectivity curve for coating design (C) is shown in black line. In this design the thickness of the Hf layer is 25 nm. If the thickness of this layer reduced to 6 nm, as in coating design (D), the reflectivity contrast reduced. The estimated reflectivity curve of coating design (D) is shown in red line.

On the other hand, the contrast between the highest reflectivity peak and the lower reflectivity area is controlled by changing the thickness of the heavy metal thickness; Figure 6-13 (b) shows the estimated reflectivity curves for coating design (C) with layer sequence: Al layer (120 nm), SiO_2 layer (90 nm), Hf layer (25 nm) and protective layer of SiO_2 layer (5 nm), and coating design (D) with consequence layers: Al layer (120 nm), SiO_2 layer (90 nm), Hf layer (6 nm) and protective layer of SiO_2 layer (5 nm). They are different in the thickness of the (Hf) metal layer. In coating design (C), the reflectivity at the highest peak is ~80% at 350 nm and dropped to the lowest reflectivity ~0% at 650 nm. While in design (D), the reflectivity at the highest peak is ~90% at 320 nm and dropped to the lowest reflectivity ~35% at 650 nm. Thus, one can conclude that, to certain limit, increasing the thickness of the heavy metal increases the contrast and reduces by decrease this layer thickness.

In our experiment, the MDM has been designed as schematically illustrates in Figure 6-14(a). The coating design consists of four layers; metal layer of (Al) with thickness 100nm, spacer dielectric layer (SiO_2) with thickness 80nm, and heavy metal (Hf) layer with thickness 12nm. A protective 5nm layer of SiO_2 has been added at the surface. The designed reflectivity curve of the MDM is shown in Figure 6-14 (b). The design of this mirror is optimized to reflect very well (85%) at the spectral region from 280nm to 350nm and the reflectivity gradually decreases for the low frequency side. The minimum reflectivity (20%) is at the region from 500-700 nm. The reflectivity starts to increase rapidly again in the NIR region. The reflectivity curve of this MDM mirror is applied to the supercontinuum spectrum of the light transient at the exit of the synthesizer, represented in red line in Figure 6-14 (c)) to produce the spectrum represented in black line in Figure 6-14 (c).

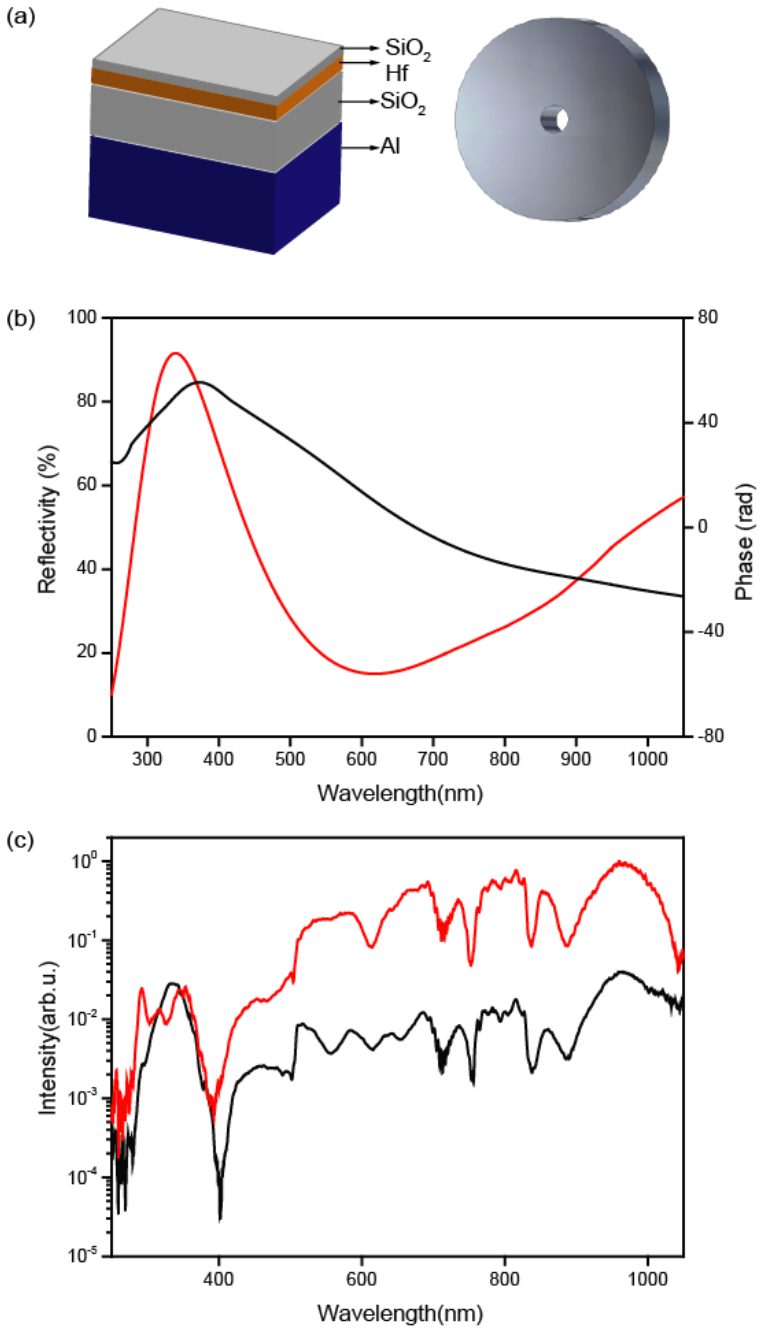

Figure 6-14: Metallic-Dielectric-Metallic (MDM) outer mirror. (a) The coating design for the outer mirror. (b) The estimated reflectivity curve of designed coating for the outer mirror is shown in red while the phase in black line. (c) Applying the estimated reflective curve of the designed coating shown in (b) on the broadband spectrum after the synthesizer (red line) obtains the spectrum (black line) after the MDM mirror. The spectrum after the MDM mirror is normalized to the spectrum after the synthesizer the region from (350-280nm) to highlight the dispersion less control of the relative intensities.

Therefore, by reflecting the spectrum of the light transient on this mirror, the desired relative intensity ratio between the constituent channels is achieved. To investigate if the mirror dispersion can affect the compression of the pulses, a replica of this mirror has been installed before the TG-FROG apparatus and the temporal profile of each of the channel pulses has been measured. The effect was found to be negligible. This proves that this mirror can control the amplitude of the amplitude of the supercontinuum without causing spectral phase distortion. For 2-octave light transient, the relative intensity ratio between the constituent channels has been modified to (18% Ch_{DUV}, 17% $Ch_{UV\text{-}VIS}$, 25% Ch_{VIS} and 40% Ch_{NIR}). The total energy after reflection is reduced to 25%.

6.3.2 Attosecond light field synthesis

The filed synthesis by control the relative phase and intensity of the constituent four channels is demonstrated in Figure 6-15. In this figure; the sampled streaking spectrograms of the synthesized light fields is shown in the first row, the retrieved electric fields in the second row and the instantaneous intensity in the third row. When the relative phase of the four channels pulses is adjusted to maximize the generated EUV flux, the pulse in Figure 6-15 (a) is generated. Tailoring the field is possible by adjusting the relative phase between the four channels to generate that light transient in Figure 6-15 (b). The instantaneous intensity of this light transient reveals three field crests with almost equal intensity amplitude. The second example of a complex synthesized waveform is shown in Figure 6-15 (c), this waveform consists of two subcycle pulses separated 3.5 fs can be engineered by adjust the relative delays between the constituent channels such the first subcycle pulse synthesized by superimposed coherently two channels ($Ch_{DUV\ and}\ Ch_{NIR}$) while the second subcycle pulse is obtained by delay and superimpose the other two channels ($Ch_{UV\text{-}Vis\ and}\ Ch_{Vis}$).

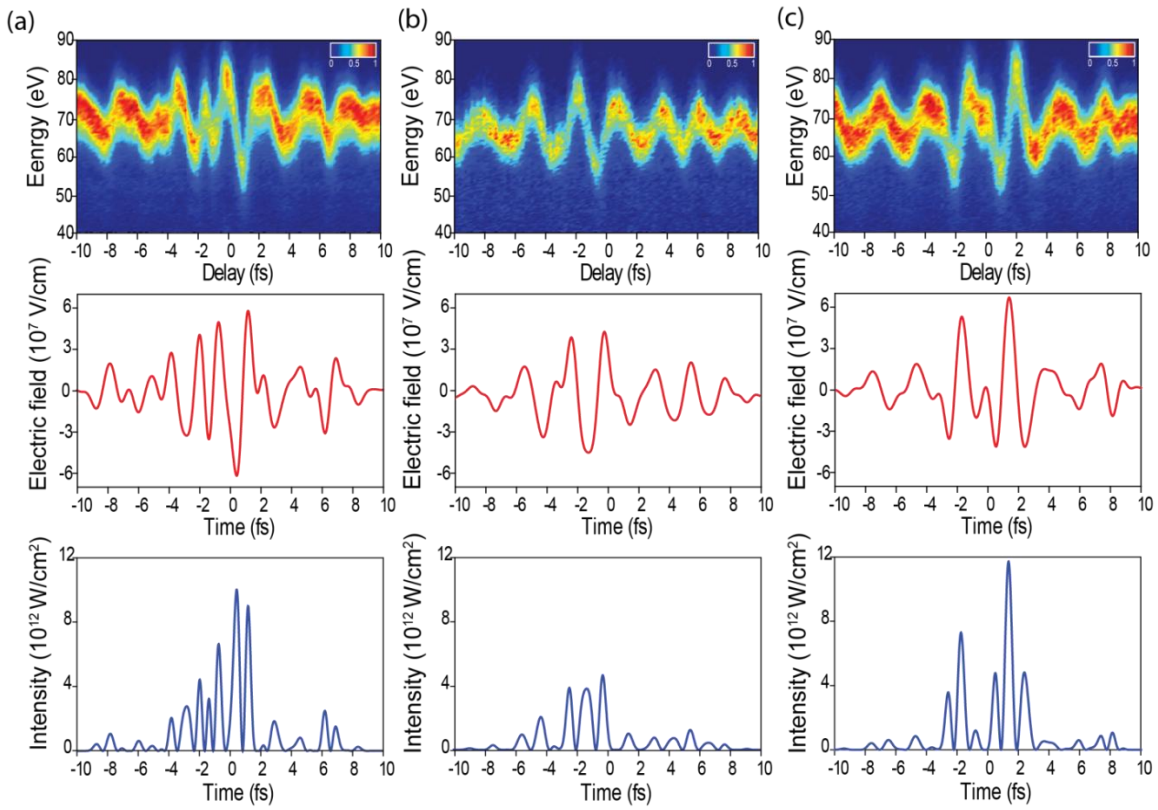

Figure 6-15: Synthesis of complex subcycle field of light transients by controlling the relative intensity and phase of the constituent channels in the apparatus. The streaking spectrograms are shown in the first row, the retrieved electric fields in the second row and the instantaneous intensity in the third row. (a) The generated light transient when the four channels not perfectly superimpose. (b) Tailored light transient with equal field intensity crests in the instantaneous intensity. (c).

6.3.3 Generation of attosecond light transients

If the pulses from the four channels are superimposed coherently such as their phase difference is zero in the middle of the trace, the "attosecond light transient" (ALT) is generated. A measured ATL is shown in Figure 6-16. In the instantaneous intensity of the ATL (Figure 6-16(c)), the central field crest is ~4.5 times more intense than the adjacent half cycles very close to the predictions of Figure 6-1. The τ_{FWHM} duration for the central field crest is ~335 as. This attosecond transient is carried at central wavelength λ_0 ~530 nm. These attosecond light transients are generated reproducibly.

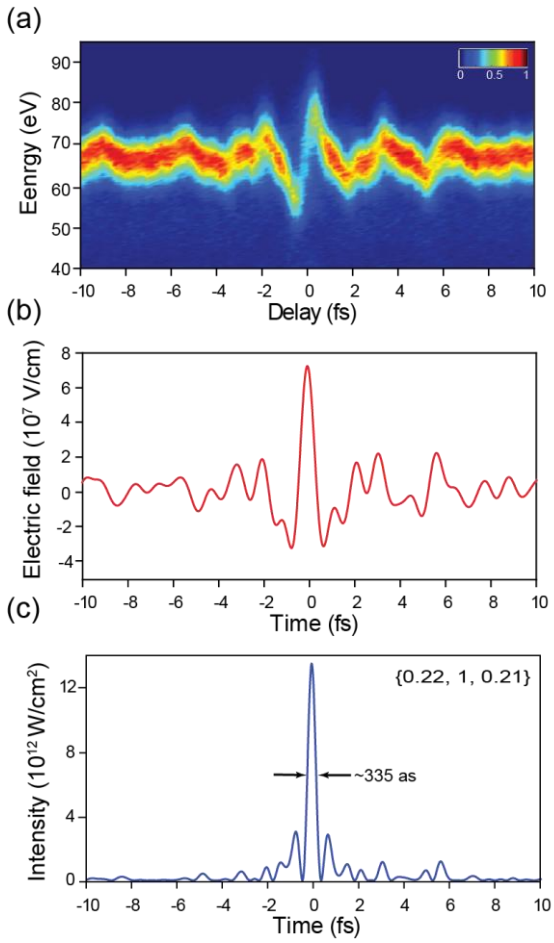

Figure 6-16: "Attosecond light transient" (ALT): (a) The sampled streaking spectrogram of the, (b) the retrieved electric field, and (c) the instantaneous intensity of the Attosecond light transient. The contrast between the main crest and the adjacent crests is ~4.5 times. The FWHM pulse duration of the main crest is < 350as.

Chapter 7

Attosecond applications of synthesized light transients

The generation and synthesis of the subcycle and attosecond light transients opens the door for a new realm in the attosecond science. In this chapter we will discuss the first attosecond applications of the subcycle and the attosecond light transients. In the first part, we will demonstrate the first attosecond pump-attosecond probe experiment utilizing the subcycle light transients by the ionization dynamics in the Krypton atomic system in subfemtosecond time scale. In the second part, the attosecond light transients have been used to demonstrate, for the first time, the attosecond control of bound electrons in Krypton atoms in the absence of ionization.

7.1 Attosecond triggering of electronic motion

First attosecond Transient Absorption (TA) spectroscopy experiments have been performed in our research team in 2010. In these experiments, 1.5 cycles laser pulses carried at a wavelength of 750nm have been utilized to pump ionization dynamics in atomic krypton and to study the valance electron motion[9, 114, 115]. In this work, as a first application for the subcycle light transients, revisit were made to the transient absorption experiment and to explore new insights, based on the enhanced resolution. The subcycle transients have been used to pump ionization dynamics of krypton atom on subfemtosecond time scale. This allows to perform the first attosecond pump-attosecond probe experiment [71].

7.1.1 Attosecond transient absorption spectroscopy

In an attosecond transient-absorption spectroscopy experiment, the NIR-laser light is used for exciting the system ('pump') and the EUV radiation for measuring the absorbance ('probe') of the system under study. General layout of a pump-probe experiment, where both pulses are propagating at vacuum speed of light c along the x axis of the lab frame Σ, is shown in Figure 7-1.

For the semi-classical description of the interaction of the pump and probe pulses with the atoms in the target gas, the following simplifications are made: The experimental interaction length of the gas cell is substantially shorter than the Rayleigh length.

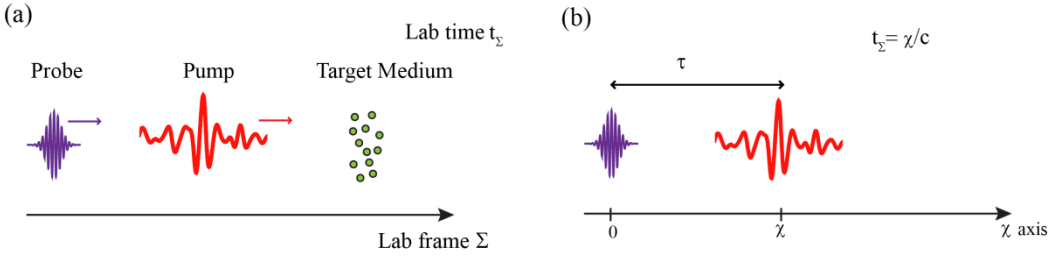

Figure 7-1: (a) General layout of a pump-probe experiment in lab frame Σ at lab time t_Σ. Specific arrangement of the problem as used for theoretical investigation where both pump and probe pulses are propagating along the x axis is shown in (b) (illustration is taken from [114]).

Hence, both pulses can be described by transverse, infinite plane waves propagation along the x axis and being linearly polarized along the z axis. Harmonic generation driven by the pump pulse in the target medium does not spectrally overlap with the spectral content of the probe pulse. The probe pulse is weaker than the pump pulse and thus fulfils the requirements for a non-invasive probe process. These pervious assumptions are experimentally verified [9].Moreover, before interaction of the atom with the light fields, the electronic system of the target medium is in its ground state $|\Psi 0\rangle$.

Temporal structure changes of the probe pulse are only due to the absorption process. The validity of this assumption is numerically verified in [116]. The pump pulse undergoes no significant modifications as it propagates through the pump-

modified target medium. Pulse propagation calculations for the experimental intensities have yielded only weak distortions of the pump beam upon its propagation through the gas target. This proves that the assumption is a good approximation.

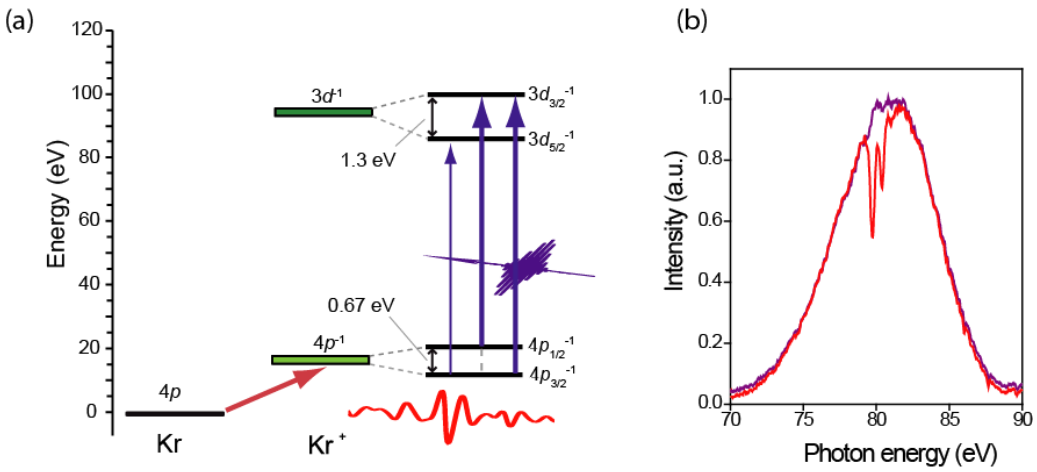

Figure 7-2: (a) the subcycle synthesized transients ionize the krypton atom and produced the Kr^+ ion. The electron liberates from the valence shell of the Krypton atoms (*4p*) to generate singly charged ($4p^{-1}$), then it is prompted by EUV pulse to create ($3d^{-1}$) core hole states . (b) Transient EUV absorption is recorded as a function of pump-probe delay; the EUV attosecond pulse spectrum transmitted from the gas target is plotted in red line and after ionization is plotted in violet line (illustration is taken from [114]).

The ionization dynamics of the system can be studied if the pump and probe pulses have temporal overlap so the absorption takes place in the presence of a strong pump field [117]. Moreover, the real time observation of valance electron motion can be studied with another interesting attosecond transient absorption spectroscopy regime in which the attosecond EUV probe pulse has no temporal overlap with the strong laser field [116].

7.1.2 Experiment method and setup

In the experiment, the subcycle synthesized transients ionize the krypton atoms and the electron liberates from the valence shell of the Krypton atoms (*4p*) to generate singly charged ($4p^{-1}$) Kr^+ ions, as schematically illustrated in Figure 7-2(a) in red line. An attosecond EUV pulse carried at photon energy of ~80 eV prompts the Kr^+ ion created at ($4p^{-1}$) manifold to the ($3d^{-1}$) core hole states, as represented by the violet line in Figure 7-2(a).

The EUV spectrum is transmitted from the quasi-static gas target in the absence of the subcycle transient field is recorded by a XUV spectrometer. The EUV spectrum is shown with violet line in Figure 7-2(b). In the presence of the subcycle transient field, the ionization of the Kr atoms takes place and the created Kr^+ ions absorb EUV photons. The transmitted EUV spectrum carries the signature of this absorption and is plotted by the red line in Figure 7-2(b).

The subcycle field transients are sampled and synthesized in the same foci point where the ionization takes place by the implementation of dual target module. For that we utilize the setup schematically illustrated in Figure 7-3: The dual target module consists of a three-axis closed-loop controlled micro-translation stage. This allows for the synthesis and sampling of the transients with highest contrast to be used in the experiment. The iris opening is adjusted from the streaking level to transient absorption experiment level. The subcycle pulse and EUV attosecond-pulse are focused on the Krypton gas target.

The EUV pulse transmitted through the target is reflected by a molybdenum-silicon mirror (reflectivity of this mirror is shown in Figure A 1 in Appendix) to image the EUV beam onto the slit of the prober spectrometer. The EUV pulse spectrum is recorded by the EUV spectrometer. A second Zr foil is installed before the entrance of the spectrometer to filter out the laser beam. The attosecond transient absorption spectrogram of Kr^+ ion is recorded as a function of the delay between the subcycle transient and the EUV attosecond pulse.

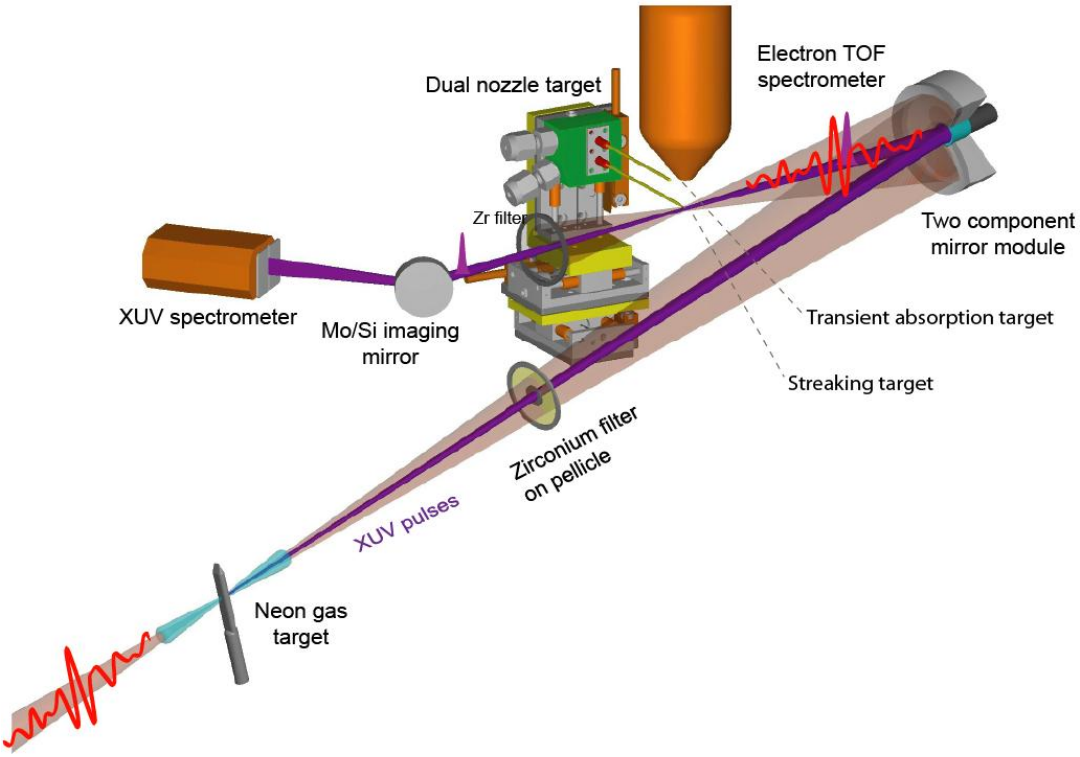

Figure 7-3: A schematic illustration of the transient absorption spectroscopy setup. The subcycle transient is sampled by the attosecond streaking technique, then; The EUV pulse and the subcycle transient are focused on the quasi-static krypton target. The transmitted EUV pule spectrum is recorded by EUV spectrometer. The attosecond transient absorption spectrogram is recorded as a function between the subcycle transient and the EUV attosecond pulse introduced by the double mirror module (illustration is taken from [114]).

7.1.3 Real time sampling of sub-femtosecond field ionization (attosecond pump - attosecond probe spectroscopy)

The subcycle light transient is sampled and synthesized to create transient with a central field crest ~1.7 times more intense than the adjacent half cycles. The streaking spectrogram, electric field and instantaneous intensity of this transient are shown in Figure 7-4 (a), (b) and (c), respectively.

This transient has been used to ionize ~16% krypton atoms enclosed in a quasi-static gas cell (length $l \approx 0.75\,mm$) at a density of $\approx 5.6 \cdot 10^{18}\,cm^{-3}$. The gas cell is positioned at the laser focus. Ionization dynamics was probed by measuring transient absorption spectra with the delayed attosecond pulse [9, 71].

Krypton ions created in their $4p^{-1}_{j=3/2}$ ground-state manifold and the $4p^{-1}_{j=1/2}$ excited-state manifold, comprising four ($m_{j=3/2} = -3/2, -1/2, 1/2, 3/2$) and two ($m_{j=1/2} = -1/2, 1/2$) states, respectively, are promoted to the $3d^{-1}$ core-hole excited states by the absorption of EUV photons from the EUV attosecond pulse (j denotes the total angular momentum and m_j denotes its projection on the z axis), as illustrated in Figure 7-2(a).

The resultant spectra transmitted through the gas cell are recorded as a function of the delay between the attosecond probe pulse (duration ~200 as, centered at ~85 eV, shown in Figure 4.3), and the ionizing field transient (pump) and yield the attosecond absorption spectrogram, which is shown in Figure 7-4 (d). The relevant absorption lines: $4p^{-1}_{3/2} \rightarrow 3d^{-1}_{5/2}$, $4p^{-1}_{1/2} \rightarrow 3d^{-1}_{3/2}$, and $4p^{-1}_{3/2} \rightarrow 3d^{-1}_{3/2}$ are indicated with arrows in the level diagram of Figure 7-2(a), where nl^{-1}_j indicates that, relative to the ground state configuration, a hole (vacancy) is created in the nl subshell. The absorption lines recorded at the leading edge of the ionizing field transient spectrum.

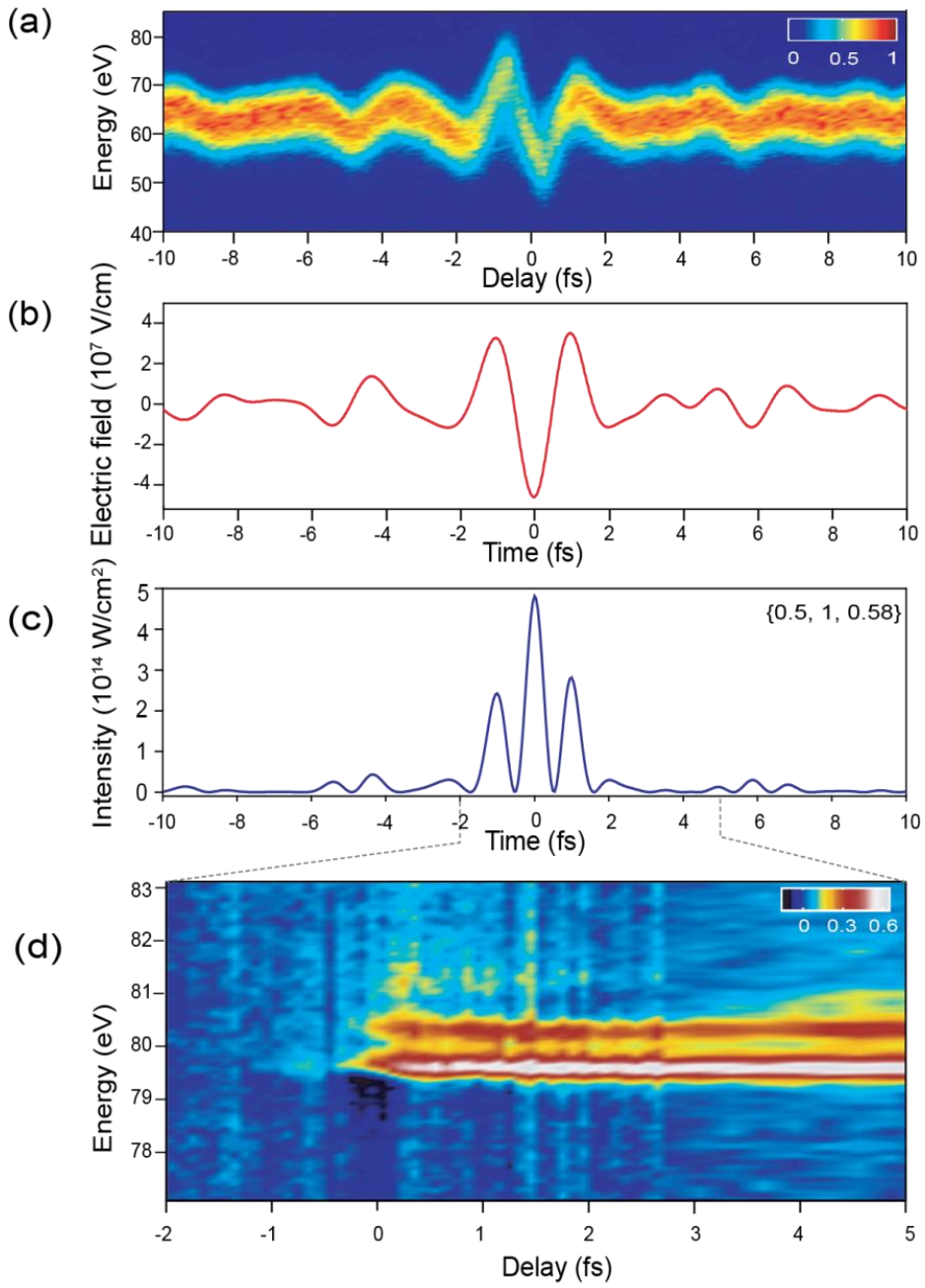

Figure 7-4: Ionization of krypton with a subcycle light field transient. (a) Streaking spectrogram, (b) retrieved electric field, and (c) the instantaneous intensity of the transient used for field ionization of Kr atoms. (d) The attosecond absorption spectrogram of Kr ions (illustration is taken from [71]).

In Figure 7-5(a), the sub-femtosecond evolution of the "effective" transient population $\rho^{eff}_{3/2,3/2}(t) = \rho^{(\pm 1/2)}_{3/2,3/2}(t) + a\rho^{(\pm 3/2)}_{3/2,3/2}(t)$ in the excited-state manifold $4p^{-1}_{j=3/2}$ (black dots), where $a = 2/3$, reflects the higher transition cross section from the $(m_j = \pm 1/2)$ states of $4p^{-1}_{j=3/2}$ to the $3d^{-1}_{5/2}$ excited state, and that of the $4p^{-1}_{j=1/2}$ manifold, $\rho^{(\pm 1/2)}_{1/2,1/2}(t)$ (black diamonds), retrieved from the $4p^{-1}_{3/2} \rightarrow 3d^{-1}_{5/2}$ and $4p^{-1}_{1/2} \rightarrow 3d^{-1}_{3/2}$ absorbance versus pump-probe delay, respectively.

Thanks to attosecond streaking in the same apparatus, this evolution can be, for the first time, directly timed and contrasted with the evolution of the ionizing field $\left|E_L(t)\right|^2$, shown in Figure 7-4(c). The build-up of the ionic populations exhibits steps in synchrony with the field crests of the transient. This becomes even more evident from the population rates obtained by temporal derivation of the full lines in Figure 7-5(a). The resultant instantaneous production rate of $\rho^{eff}_{3/2,3/2}(t)$ shown in Figure 7-5(b) (in red line) exhibit three main features at the crests of the ionizing field. The main ionization burst is responsible for approximately 80% of the ion population and has a full width at half maximum of < 0.7 fs, indicating sub-femtosecond confinement of field ionization. This confinement to a single field crest allows, for the first time, quantitative evaluation of the instantaneous rate of optical field ionization and state-selective population dynamics. For the population depicted one evaluates a peak production rate of $\rho^{eff}_{3/2,3/2}(t)$ as $\Gamma_{peak} = (0.1 \pm 0.0042)\, fs^{-1}$ and for $\rho^{1/2}_{1/2,1/2}(t)$ as $\Gamma_{peak} = (0.6 \pm 0.0036)\, fs^{-1}$ in excellent agreement with results obtained by numerically integrating Schrödinger equation of a single-active electron model in three dimensions, which also well reproduces details of the temporal evolution of the ionic populations, as shown with green and magenta lines in Figure 7-5(a) and green line of Figure 7-5(b).

On the basis of a theoretical model [71, 117] this was performed by colleagues, A. Moulet, R. Santra and a co-worker (CFEL Theory division – Hamburg). Since, in this experiment, EUV probe pulse duration amounts to ~200 as , the present approach suggests that the technique of tracking the peak of the absorption offers a possibility to recover the underlying population dynamics with an accuracy superior to 10%.

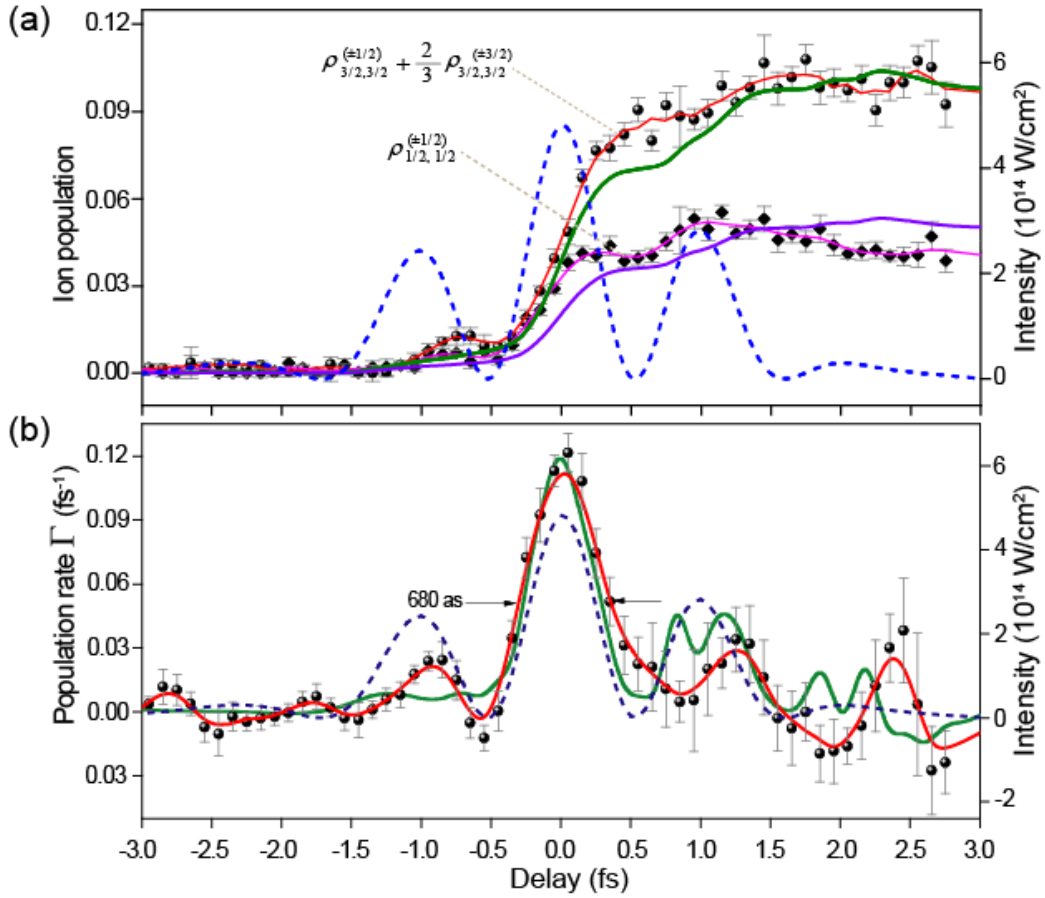

Figure 7-5: Attosecond ionization. (a) Population dynamics in the ground-state $4p^{-1}_{j=3/2}$ manifold (dots), $\rho^{eff}_{3/2,3/2}(t)$, and in the excited-state $4p^{-1}_{j=1/2}$ manifold (diamonds), $\rho^{(1/2)}_{1/2,1/2}(t)$, retrieved from the absorption spectrogram of Figure 7-4(d), and contrasted with the instantaneous intensity (dashed line) as well as with the prediction of numerical simulations being convolved with the EUV probe pulse duration (green and purple lines). (b) Ionization rate $d\rho^{eff}_{3/2,3/2}(t)/dt$ evaluated from the data in (A) (dots and red line) in comparison with the theoretical prediction (green line) (illustration is taken from [71]).

7.1.4 Real-time observation of valence electron motion in Kr^+ with well-defined quantum phase

Attosecond probing of few-cycle-driven field ionization of Kr atoms has revealed the emergence of a valence electron wave packet in the $4p$ sub-shell of the Kr^+ ensemble, as a consequence of liberation of electrons from the $4p_{j=3/2}$ as well as the $4p_{j=1/2}$ manifolds, separated in energy by spin-orbit coupling in the krypton atoms[9]. By repeating this attosecond absorption spectroscopic experiment with our subcycle transient shown in Figure 7-4(c), and supplementing it with attosecond streaking in Figure 7-4(a-c), one can now launch a valence wavepacket within a subfemtosecond interval and with subfemtosecond absolute timing accuracy for the first time, implying unprecedented control of new insights into valence electron dynamics. From the recorded absorption spectrogram (Figure 7-6 (a)) one retrieves the fractional populations of the six ionic states, in the form of the diagonal matrix elements $\rho^{(m_j)}_{j,j'=j}$ of the reduced density matrix—$\rho^{(3/2)}_{3/2,3/2} + \rho^{(-3/2)}_{3/2,3/2} = 0.315 \pm 0.024$, $\rho^{(1/2)}_{3/2,3/2} + \rho^{(-1/2)}_{3/2,3/2} = 0.400 \pm 0.024$, $\rho^{(1/2)}_{1/2,1/2} + \rho^{(-1/2)}_{1/2,1/2} = 0.285 \pm 0.004$—and with a degree of coherence of $g = 0.85 \pm 0.06$ which exceeds that measured in the previous experiment [9] by ~1.4 times, and is unparalleled for long-lived (> 1 fs) coherences in the valence shell. The measured coherence is well predicted, as well as fractional populations in the $4p^{-1}_{j=1/2}$ and $4p^{-1}_{j=3/2}$ manifolds by the simulation, which has been done based on a state-of-the-art 3D time-dependent configuration-interaction singles approach [118]. This simulation includes correlation dynamics between the field-generated hole and the photoelectron, it has been extended to include spin-orbit interaction [119]. The nearly perfect coherence is a direct consequence of the sub-fs width of the ionization gate. This confinement, along with sub-fs absolute timing information from streaking, allows launching the wavepacket with a well-defined initial phase.

Figure 7-6 (b) and (c), show the retrieved phase $\phi(t)$ (Eq. 2 in [9]) of the quantum superposition along with representative snapshots of the generated ensemble-averaged hole density distributions, as evaluated from the relevant data in Figure 7-6 (a). Linear extrapolation of $\phi(t)$ to "time zero", the birth of the hole at the peak of the ionizing field transient (blue line in Figure 7-6 (b)), yields $\phi(t_0) = (0.99 \pm 0.04)\pi$, in very good agreement with the prediction of our configuration-interaction based simulations: $\phi(t_0) = 1.06\pi$. This initial quantum phase implies to an elongated initial hole-density distribution aligned with the ionizing field vector, and commensurate with intuitive expectation.

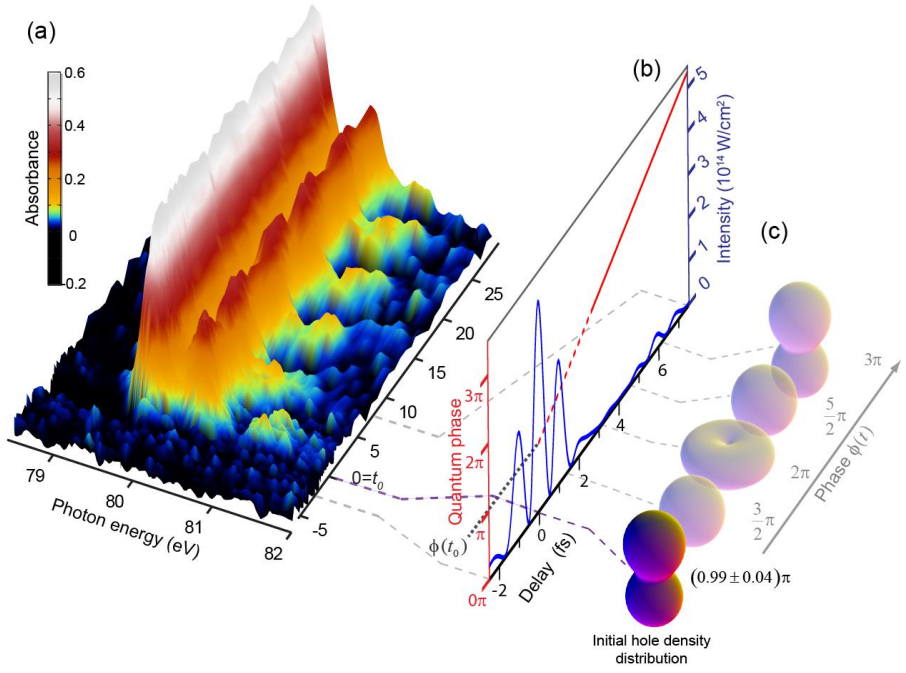

Figure 7-6: Initial quantum phase and density distribution of a valence electron wavepacket. (A) Attosecond transient absorption spectrogram of krypton atoms field-ionized by a sub-cycle field transient is shown by the blue line in (B). Linear extrapolation of the retrieved quantum phase $\phi(t)$ shown by the red line in (B) to time zero determined by attosecond streaking, allows access to the initial quantum phase $\varphi(t_0) = (0.99 \pm 0.04)\pi$ of the valence electron wavepacket. (C) Ensemble-averaged initial hole density distribution in the valence shell at the instant of ionization and its subsequent evolution, as evaluated from (A) (illustration is taken from [71]).

7.2 Attosecond control of bound electron

This section will offer a first glimpse to the control possibilities that emerge not by the synthesized subcycle transients of Chapter 5 but by the attosecond light transients of chapter 6 and how they can be used to explore a new realm of attosecond physics. An essential question that sooner or later we will have to answer is if we can control electrons without ionizing the systems in question. If this is possible, this will considerably extend the capabilities in attosecond science to drive the attosecond dynamics in atoms, molecules nanostructures and solids. As a preliminary application of the attosecond light transients, controlling the bound electron dynamic motion of krypton atoms is demonstrated.

7.1 First steps towards attosecond bound electron control

The use of a controlled CEP stable waveforms permit the triggering and controlling of free electronic wavepacket on the attosecond time scale. This has been demonstrate in [120] for the first time. After this seminal experiment, many efforts have paved the way of electron control based on ionization and recollision of free electrons. In this first experiment, the attosecond control of electronic polarizability has been attained in the high field regime. The peak intensity is high enough to set free several electronic wave packets which are removed from their parent ion, but within a laser period they are pulled back to trigger and probe atoms. The highest-energy portion of the wave packet re-collides with the parent ion near the second zero transition of the laser field, as shown in Figure 7-7 (a). The equidistant emitted lines are corresponding to the high odd harmonics of the driver laser pulse. Energetic EUV photons are emitted and sequences of sub-femtosecond bursts in the time domain are generated. The spectral distribution of these photons depends sensitively on the carrier-envelope phase (CEP) as we discussed in the initial chapters, which defines whether or not they are emitted in a single sub-femtosecond EUV burst or in a couple of bursts. For a cosine waveform ($\varphi = 0$) featuring a “single” strongest half-cycle, the highest-energy photons are emitted within a single burst, while for a sine waveform ($\varphi = \pi / 2$) the most two intense

half cycles resulting in a pair of most energetic re-colliding wave packets, thus, the two different waveforms have different spectral distributions of the highest energy photons, the spectral distributions is continuous in case of the cosine waveform and the distribution exhibiting periodic modulation in the case of sin waveform.

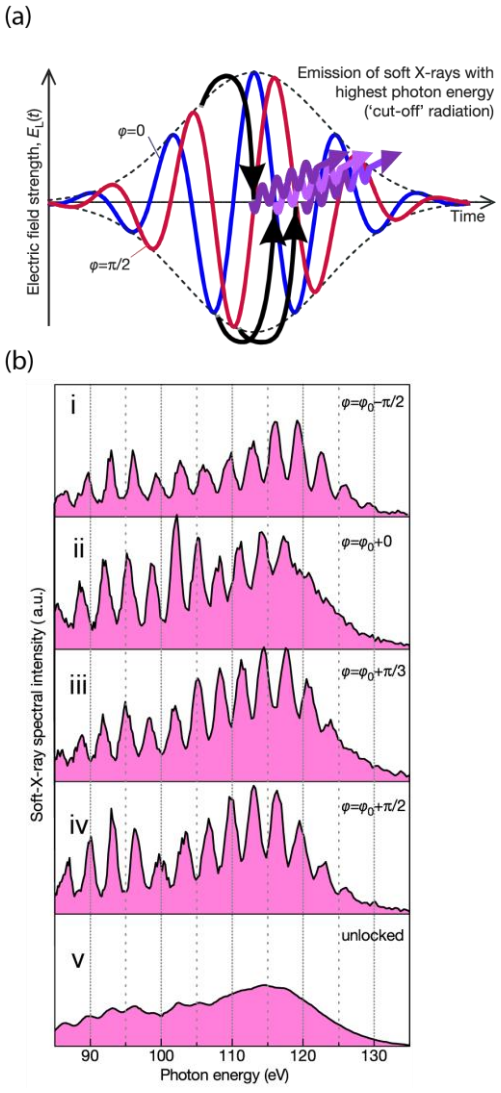

Figure 7-7: Control the electronic wave packet in an ionized atom. (a) Illustration of the highest-energy EUV photons emission, for a cosine waveform (blue line) they are temporally confined to one single burst, while sine waveform (red line) yields two bursts of comparable amplitude separated by~$T_0/2$. (b) the effect of the CEP variation on measured spectral intensity of few-cycle-driven soft-X-ray emission from ionizing atoms. From b(i) to b(iv), the measure spectral is measured for phase-stabilised pulses for different CEP settings, and b(v) spectrum measured without phase stabilization (illustration is taken from [71]).

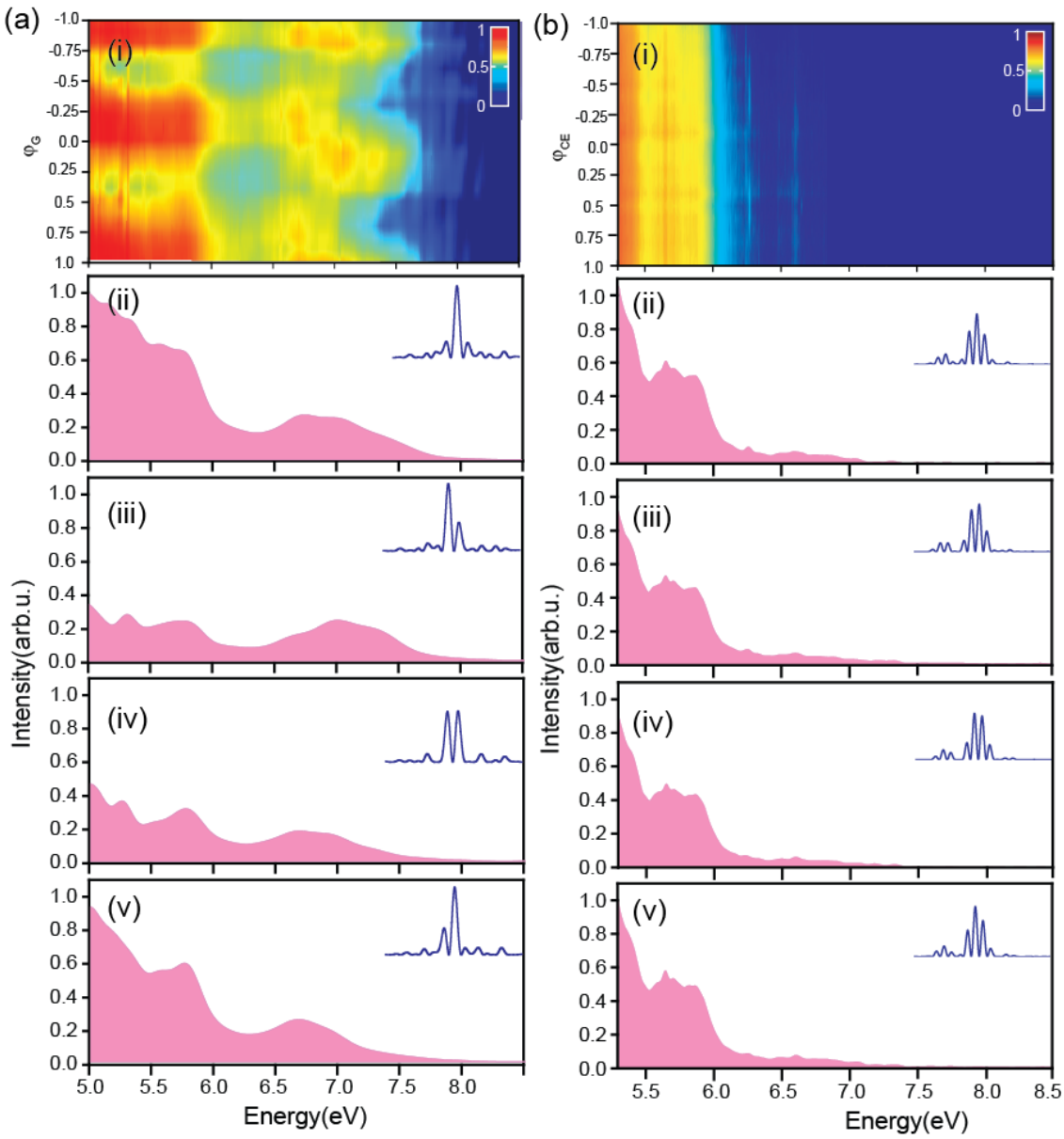

Figure 7-8: Attosecond polarizability control of bound electrons. The conspicuous modulation of the emitted VUV spectra as a function of the global phase φ_G of the waveform for the attosecond light transient is shown in (a), while in (b) for 1.5 cycle pulse which is composed by utilizing only Ch_{vis} and Ch_{NIR} of the synthesizer, with more detail in the text.

As first application of the attosecond light transients (ALTs), the bound electron control in attosecond time scale is explored. In our experiment, the generated light transient from the synthesizer is sampled. In a next step the phases between different bands are adjusted in order to generate an attosecond light transient (Figure 6-16). It is then focused into a quasi-static Kr gas target (85 mbar) to generated radiation in the VUV part of the spectrum (5-10 eV); the setup is very similar as in the experiments of chapter7 (Figure 7-3). Instead of the metallic filter installed before the EUV spectrometer, two silicon mirrors at 72º have been introduced in order to filter out the intense components of light transient from the generated VUV spectrum. Because the interest is in capturing the dynamics of bound electrons, the VUV emitted radiation by the attosecond light transients is recorded by the VUV spectrometer. Changing the driver global phase setting φ_G of the attosecond light transients yields dramatic change in the spectral distribution of emitted radiation in close analogy with the experiments with free electrons alluded to earlier. For comparison, the same measurement was performed; utilizing a 1.5 cycle pulse utilizing only two channels of the synthesizer (Ch_{Vis} and Ch_{NIR}) has been recorded where the dynamic control of the VUV is absent.

Figure 7-8 (a) shows the effect on the spectral distribution of the harmonic radiation spectrum generated by ALTs by changing the global phase; while Figure 7-8 (b) shows that the changing the global phase does not change the spectral distribution of the harmonic spectrum generated by a 1.5 cycle driver pulse. This confirms the ability of controlling the system polarizability utilizing the attosecond light transient which triggers the dynamics for the bound electrons for the first time on the attosecond time scale.

More detailed studies on the capabilities of the attosecond light transients to drive on the electronic dynamics in atoms, molecules and nanostructures are in progress and it will be reported in upcoming works.

Chapter 8

Conclusions and Outlook

7.2 Conclusions

New capabilities in controlling light waveforms have been demonstrated for the first time in this thesis. The instantaneous field of subcycle light transients has been tailored on demand with attosecond resolution by ultrawideband light field synthesis in the visible and flanking ranges. First experiments utilizing the considerably improved resolution been conducted such as the study of ionization dynamics of the Kr atom. Utilizing these transients, the ionization window has been confined, for the first time, to the sub-fs time scale permitting the demonstration of the first attosecond pump attosecond probe experiment. The improved coherence of the generated bound wavepackets in the Kr^+ ion is also witnessing the new capabilities. By extending the synthesis to over more than two optical octaves "attosecond light transients" have been created. First steps towards the control of bound electrons, utilizing these transients, have been explored.

7.3 Future prospects

The attosecond control of the instantaneous field of the subcycle light transients opens new prospects in ultrafast science. This may make a revolutionary step in control of the electronic motion in atoms and molecules. On the other hand, this high resolution of field control enables high accuracy in triggering and clocking atomic scale phenomena such as coherent ultrafast electronic superposition.

"Nanoscale circuitry" is an area in which some of the most prominent applications of light control may be applied in the near future. The highest density of infor-

mation that can be encoded into a propagating burst of light relates to the potential of tailoring (encoding) the field as well as to characterizing it (decoding).
Ultrafast technologies [121] have given important examples of this emerging capability via the control of the intensity profile of picosecond pulses in order to encode bits of information through the switching of temporal features within femtosecond time intervals.

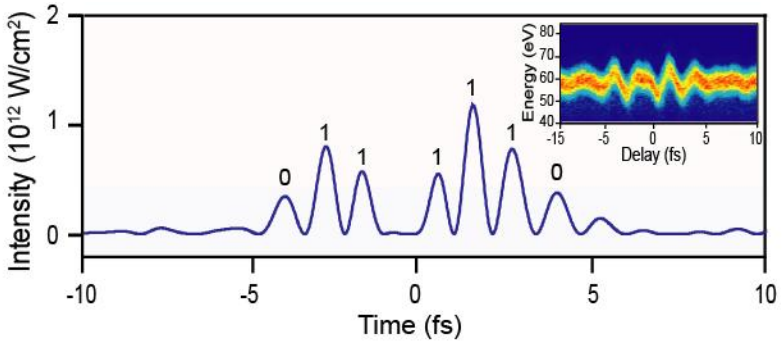

Figure 8-1: Instantaneous intensity profile of synthesized light transients appropriate for encoding of digital information at individual half-cycles to transmit and process information on the Pbit/sec scale (illustration is taken from [70]).

Now, the subcycle synthesis of light transients unlocks the potential of extending this capability to its ultimate limits: the encoding of digital information on light transients through the real-time switching of specific half-cycles in a light transient (Figure 8-1) at rates that exceed 1 Pbit/sec. This will extend the frontiers of modern electronics and information processing technologies to the PHz realm.

As the subcycle light transients open new aspects in ultrafast science, the attosecond light transients open new realm in the attosecond science. Attosecond light transients give the opportunity to explore the electronic dynamics with attosecond resolution in the weak field regime.
On the other hand, it can be combined with EUV attosecond pulse to perform the attosecond pump- probe time resolved experiment.

Equally exciting are the envisaged applications of attosecond light transients in molecular electronic control. Studies in prototypical molecules based upon carrier and envelope controlled pulses [26], as well as numerous theoretical studies [122, 123] suggest new ways of molecular control that could profoundly benefit from the exertion of a controlled transient of light to steer the relevant dynamics.

Scalability of the light field synthesis can be occurring by extend synthesis of the light to over several more optical octaves. Additional spectral channels in the deep and vacuum ultraviolet, as well as in the infrared region of the spectrum, are required to introduce in the light field synthesizer to create a new generation of light-sculpting tools. The prerequisite of this extension is the development of the supercontinuum light sources. Recent progress in the developments of superoctave VUV sources [124], and light sources in the near and mid-infrared [125] promise the extension of these technologies into this demanding field.

On the other hand, the power scalability is possible due to the simplicity of the light field synthesizer and the fact that it is based exclusively on dielectric optics by simply increasing the size of the optics in the apparatus to sustain synthesis of pulses in the multi-terawatt or petawatt scales.

APPENDIX

I. Numerical procedure for evaluating the field of a light transient

The following is a description of the particular methods we used for extracting the field transient waveforms from the streaked spectra, done by Justin Gagnon, First, the centroids of the spectra are evaluated for each EUV-NIR delay, from which the vector potential $A_{TR}(t)$ is obtained by solving (1) (ignoring the last term). The vector potential is then numerically differentiated, giving the electric field $E_{TR}(t) = -\partial_t A_{TR}(t)$ of the transient. Since $A_{TR}(t)$ is relatively noisy after being extracted from the streaked spectra, we compute its derivative in the frequency domain:

$$\partial_t A_{TR}(t) = \frac{1}{\sqrt{2\pi}} \int_{-\infty}^{\infty} i\omega H(\omega) \tilde{A}_{TR}(\omega) e^{-i\omega t}\, d\omega,$$

$$H(\omega) = S\left(\frac{\omega+\Omega}{\delta}\right) S\left(-\frac{\omega-\Omega}{\delta}\right),$$

$$S(x) = \begin{cases} 0, & x \le -1/2 \\ \frac{8}{9}\sin^4\left[\frac{2\pi}{3}\left(x+\frac{1}{2}\right)\right], & -1/2 < x \le 0 \\ -\frac{8}{9}\sin^4\left[\frac{2\pi}{3}\left(x-\frac{1}{2}\right)\right], & 0 < x \le 1/2 \\ 1, & 1/2 < x \end{cases},$$

where $\tilde{A}_{TR}(\omega)$ is the Fourier transform of $A_{TR}(t)$. $S(x)$ is a smoothed step function that is thrice differentiable. We choose the width of the spectral window, $\Omega = 0.5 \Big/ \Delta t_{\min}$, such that temporal structure finer than $\Delta t_{\min} = 0.5\ fs$ is ignored upon taking the derivative. After obtaining the time series $E_{TR}(t)$, it is windowed in the time domain by $H(t)$ to ensure that it falls to zero at the edges of the overall temporal window. This suppresses noise in the evaluated light transient spectrum, particularly around the high frequency edge. The (real) time series for $E_{TR}(t)$ is then transformed into an analytic signal $\tilde{E}_{TR}(t) = \frac{1}{\sqrt{2\pi}} \int_{-\infty}^{\infty} \Theta(\omega) \tilde{E}_{TR}(\omega) e^{-i\omega t} d\omega$, Where $\tilde{E}_{TR}(\omega)$ is the Fourier transform of $E_{TR}(t)$, and $\Theta(\omega)$ is the Heaviside step function, thus removing the negative frequencies from $E_{TR}(t)$. Following this procedure, the electric field is converted from atomic units to *V*/*m* multiplying it by $\hbar^2 / m_e a_0^3 e$, from which are evaluated the temporal intensity envelope and phase of the waveform, given by $c\varepsilon_0 \left|\tilde{E}_{TR}(t)\right|^2$ and $\arg\left[\tilde{E}_{TR}(t)\right]$, respectively. The transient's (complex) spectrum is then given by: $S_{TR}(\lambda) = \frac{c\varepsilon_0}{2\lambda^2} \left|\tilde{E}_{TR}(2\pi c/\lambda)\right|^2 e^{i\arg\left[\tilde{E}_{TR}(2\pi c/\lambda)\right]}$, where $\tilde{E}(\omega)$ is the Fourier transform of the analytical field.

II. Time axis adjustments between consecutively sampled light transients

According to the principles of high order harmonic generation, the timing of an attosecond burst and that of its driver pulse are intimately related; in particular, the emission of the attosecond burst is linked to the most intense field cycle of the driver field. In our experiments, this implies that if two successively synthesized light transients have considerably different field waveforms, a temporal offset associated to the above mentioned timing may need to be compensated for, prior to their comparison. The tools presented in Section II and in Appendix I offer this capability. In a first step, both waveforms are decomposed into their constituent channels (c). Because the fine timing of pulses in Ch_{Vis} is not adjustable by our synthesizer apparatus – only the optical paths in $Ch_{Vis\text{-}UV}$ and Ch_{NIR} can be finely adjusted –their fields can be used to define an absolute time reference and to adjust the temporal axes of successively synthesized light transients with respect to each other. In particular, we temporally translate the field of one of the two light transients in order to overlap their Ch_{Vis} waveforms. Practically, this is achieved at a relative delay that minimizes their rms difference. Adjustments up to 1.6 fs have been introduced in the data shown in Figure 5-8 (d). The accuracy of this approach has been verified by HHG simulations based on the Lewenstein model and this methodology is quite universal. It can also be used to compensate for other kinds drifts between the attosecond probe and light transients in the measuring apparatus.

III. The EUV multilayer mirror

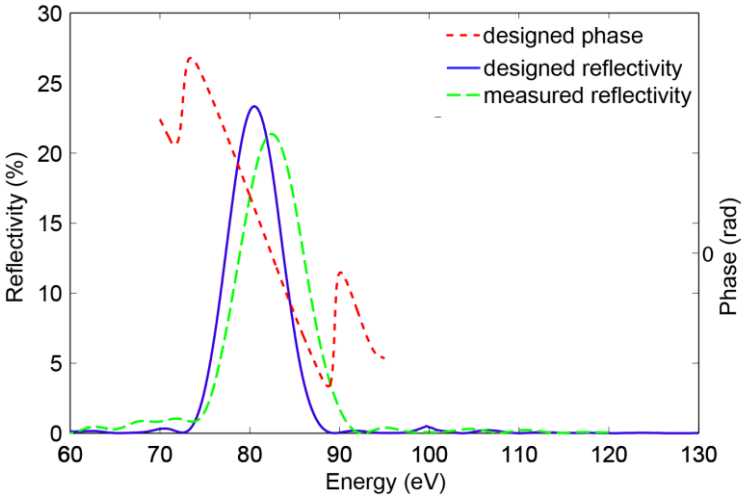

Figure A 1: EUV multilayer coated mirror, optimised for high reflectivity at central energy ~82 eV. Simulated and measured reflectivity curve and spectral phase of EUV mirror at an angle of incidence of 5° are shown in solid blue, dashed green, and dashed red, respectively.

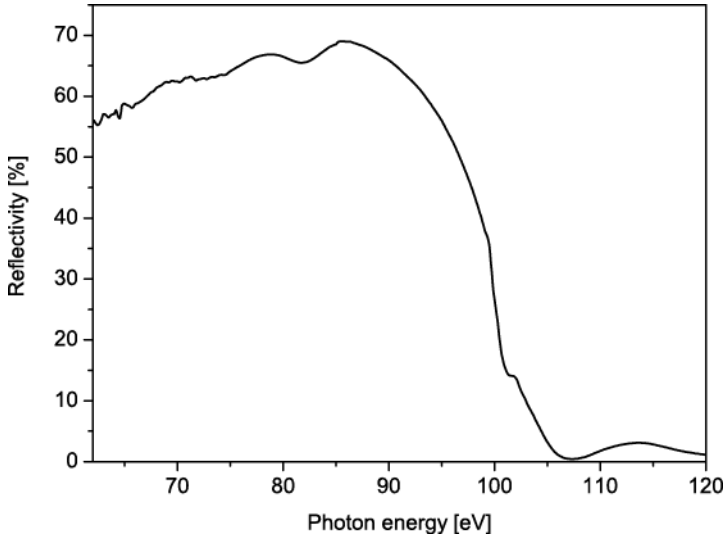

Figure A 2: Simulated reflectivity curve of broadband molybdenum-silicon EUV imaging mirror for p-polarized light at an angle of incidence of 67°. This mirror is used to image the EUV beam onto the slit of the EUV spectrometer. The mirror designed by M. Hofstetter and A. Guggenmos.

IV. Delay correction between streaking and transient absorption spectrograms

Strong-field ionization, as studied in our attosecond transient absorption experiments, requires field intensities on the order of 10^{14} W/cm^2 and beyond. In contrast, streaking measurements of the light waveforms require intensities on the order of 10^{12} W/cm^2. In the transient absorption experiments, the intensity of the laser beam is varied by adjusting its size with an adjustable aperture placed before the focusing mirror.

Increase the illuminated area of the mirror between a streaking and a transient absorption (TA) measurement can be responsible for spatiotemporal effects which cause a delay between the weak (streaking) and the strong (TA) pulse, which must be corrected before comparing the sampled field by the streaking and transient absorption measurements on the same delay axis.

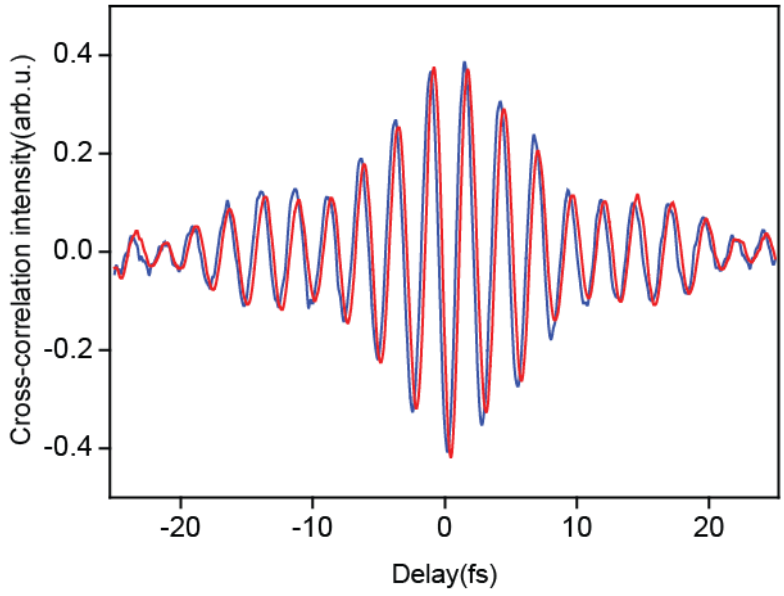

Figure A 3: Variation of the focal point intensity in a cross-correlation measurement obtained under streaking (red line) and transient absorption (blue line) intensity settings.

This effect has been investigated by removing the metallic filter of the pellicle used in the experiments and recording the linear cross-correlation trace between the central part of the NIR beam, and the portion reflected off the outer mirror for two different setting of illumination, corresponding to those of the streaking and TA measurements, respectively. Figure A 1 shows the variation of the intensity at the focal point of the beams imaged on a CCD camera (averaged over 5×5 pixels covering the central part of the beam) as a function of the delay between inner and outer mirror. The delay between the two traces is evaluated by a linear fit of the spectral phases of both signals and amounts to (280 ± 50) as.

Retrieval of population during strong-field perturbation

The formation of the population in the presence of the pump pulse has been addressed by fitting the spectrogram using:

$$A_P(\omega,\tau) = -\ln\left[\exp\left[-c(\omega,\tau)\right] * G(\omega)\right] + A_0(\tau)$$

where $G(\omega)$ and $A_0(\tau)$ are introduced above, and $c(\omega,\tau)$ describes the absorption lines by three Lorentzian line shape functions:

$$c(\omega,\tau) \propto \frac{1}{2\pi}\sum_{i=1}^{3} n_i(\tau)\frac{\Gamma}{\left(\omega-\omega_i(\tau)\right)^2+\left(\Gamma/2\right)^2}\,.$$

Here, the $n_i(\tau)$ denotes the effective population and $\omega_i(\tau)$ the center frequency of the i^{th} absorption line. The fit was carried out for the delay range of -20.25 to 29.75 fs and within the spectral window extending from 77.9 to 83 eV, where the results obtained in the range 2.75 to 29.75 fs served to scale the effective populations according to the determined population by utilizing above equation.

V. Reconstruction of electron motion and determination of fractional ionization

Preparation of data prior to fitting

The absorbance spectrogram shown in Figure 7-6 (a) was obtained by averaging over 12 consecutive scans taken under the same experimental conditions. All EUV spectra of the combined spectrogram were normalized in the spectral range from 83.0 - 86.7 eV (high energy side besides the Kr^+ absorption lines) to reduce noise originating from flux fluctuations of the EUV probe pulse. For calculating the absorbance $A(\omega,\tau)$, the mean spectral density in the range before ionization (-20.25 to -6.25 fs) has been used as a reference spectrum.

Fitting procedure

To reconstruct the Kr^+ quantum state distribution, the coherence of the spin-orbit wavepacket motion as well as the quantum phase, a fit of the experimental data shown in Figure 7-6 (a) is performed by fitting the equation

$$A(\omega,\tau) = -\ln\left[\exp\left[-n_0\sigma(\omega,\tau)L\right] * G(\omega)\right] + A_0$$

to the spectrogram. Here, $\sigma(\omega,\tau)$ is an analytical description of the cross-section of the three absorption lines of Kr^+ as reported in [116] (Eq. 35) where the reported reduced transition matrix elements are employed. Furthermore, τ indicates the time of probing, $n_0 = 5.75\cdot 10^{18} cm^{-3}$ the initial number density of neutral atoms, $L = 0.74\,mm$ the length of the target cell and $G(\omega)$ an area-normalized Gaussian convolution function with Δ being the FWHM value characterizing the finite spectrometer resolution and A_0 a constant offset. The coherence term in $\sigma(\omega,\tau)$ is described by

$$\rho^{(1/2)}_{3/2,1/2}(\tau) = \left|\rho^{(1/2)}_{3/2,1/2}\right| \exp\left(i\,\phi(\tau)\right) = \left|\rho^{(1/2)}_{3/2,1/2}\right| \exp\left(i\Delta E_{SO}\tau + i\delta\right)$$

where ΔE_{SO} is the spin-orbit wave packet splitting and δ a phase offset which depends on the choice of the time origin $\tau = 0$. The term, $\tau = 0$, was chosen, such that it coincides with the maximum of the instantaneous intensity of the synthesized light field transient. Hence, the quantity δ equals the initial quantum phase.

The data set is fitted by employing the Levenberg-Marquardt optimization algorithm in the range 78.5 – 82 eV and for the delays 2.75 to 29.75 fs, avoiding the fit in the presence of the strong single-cycle initiation pulse since Eq. 35 (provided in [116]) is not valid for describing EUV absorption under strong field influence. Fitted parameters have been the populations $\rho_{1/2,1/2}^{(1/2)}$, $\rho_{3/2,3/2}^{(1/2)}$, $\rho_{3/2,3/2}^{(3/2)}$, the terms describing the coherence $\left|\rho_{3/2,1/2}^{(1/2)}\right|$, ΔE_{SO}, δ, the three central energies of the EUV transitions $E_{3d_{5/2}} - E_{4p_{3/2}}$, $E_{3d_{3/2}} - E_{4p_{3/2}}$, $E_{3d_{3/2}} - E_{4p_{1/2}}$, as well as the spectrometer resolution Δ and the constant offset A_0.
The sum of populations permits evaluation of the fractional ionization.

Error Analysis

Error bars of the fit quantities represent the standard error of fit results obtained by applying the described fitting approach to six consecutive pairs of the 12 delay scans.

Bibliography

[1] H. Abraham, and T. Lemoine, "Disparition instantanée du phénomène de Kerr", Compt. Rend., (1899) 206.

[2] T.H. Maiman, "Stimulated Optical Radiation in Ruby", Nature, 187 (1960) 493-94.

[3] M. Dantus, R.M. Bowman, A.H. Zewail, "Femtosecond laser observations of molecular vibration and rotation", Nature, 343 (1990) 737-39.

[4] A.H. Zewail, "Femtochemistry: Atomic-Scale Dynamics of the Chemical Bond†", The Journal of Physical Chemistry A, 104 (2000) 5660-94.

[5] M. Hentschel, R. Kienberger, C. Spielmann, G.A. Reider, N. Milosevic, T. Brabec, P. Corkum, U. Heinzmann, M. Drescher, F. Krausz, "Attosecond metrology", Nature, 414 (2001) 509-13.

[6] Y. Mairesse, A. de Bohan, L.J. Frasinski, H. Merdji, L.C. Dinu, P. Monchicourt, P. Breger, M. Kovačev, R. Taïeb, B. Carré, H.G. Muller, P. Agostini, P. Salières, "Attosecond Synchronization of High-Harmonic Soft X-rays", Science, 302 (2003) 1540-43.

[7] M. Drescher, M. Hentschel, R. Kienberger, M. Uiberacker, V. Yakovlev, A. Scrinzi, T. Westerwalbesloh, U. Kleineberg, U. Heinzmann, F. Krausz, "Time-resolved atomic inner-shell spectroscopy", Nature, 419 (2002) 803-07.

[8] R. Kienberger, E. Goulielmakis, M. Uiberacker, A. Baltuska, V. Yakovlev, F. Bammer, A. Scrinzi, T. Westerwalbesloh, U. Kleineberg, U. Heinzmann, M. Drescher, F. Krausz, "Atomic transient recorder", Nature, 427 (2004) 817-21.

[9] E. Goulielmakis, Z.-H. Loh, A. Wirth, R. Santra, N. Rohringer, V.S. Yakovlev, S. Zherebtsov, T. Pfeifer, A.M. Azzeer, M.F. Kling, S.R. Leone, F. Krausz, "Real-time observation of valence electron motion", Nature, 466 (2010) 739-43.

[10] W.S. Warren, H. Rabitz, M. Dahleh, "Coherent Control of Quantum Dynamics: The Dream Is Alive", Science, 259 (1993) 1581-89.

[11] P.W. Brumer, M. Shapiro, Principles of the Quantum Control of Molecular Processes Wiley-Interscience, New Jersey, 2003.

[12] T. Brixner, N.H. Damrauer, G. Gerber, Femtosecond quantum control, in: B. Benjamin, W. Herbert (Eds.) Advances In Atomic, Molecular, and Optical Physics, Academic Press, 2001, pp. 1-54.

[13] A. Assion, T. Baumert, M. Bergt, T. Brixner, B. Kiefer, V. Seyfried, M. Strehle, G. Gerber, "Control of Chemical Reactions by Feedback-Optimized Phase-Shaped Femtosecond Laser Pulses", Science, 282 (1998) 919-22.

[14] M. Wollenhaupt, V. Engel, T. Baumert, "FEMTOSECOND LASER PHOTOELECTRON SPECTROSCOPY ON ATOMS AND SMALL MOLECULES: Prototype Studies in Quantum Control", Annual Review of Physical Chemistry, 56 (2005) 25-56.

[15] J. Reichert, R. Holzwarth, T. Udem, T.W. Hänsch, "Measuring the frequency of light with mode-locked lasers", Opt. Commun., 172 (1999) 59-68.

[16] A. Apolonski, A. Poppe, G. Tempea, C. Spielmann, T. Udem, R. Holzwarth, T.W. Hänsch, F. Krausz, "Controlling the Phase Evolution of Few-Cycle Light Pulses", Phys. Rev. Lett., 85 (2000) 740-43.

[17] D.J. Jones, S.A. Diddams, J.K. Ranka, A. Stentz, R.S. Windeler, J.L. Hall, S.T. Cundiff, "Carrier-Envelope Phase Control of Femtosecond Mode-Locked Lasers and Direct Optical Frequency Synthesis", Science, 288 (2000) 635-39.

[18] T. Udem, R. Holzwarth, T.W. Hansch, "Optical frequency metrology", Nature, 416 (2002) 233-37.

[19] S. Koke, C. Grebing, H. Frei, A. Anderson, A. Assion, G. Steinmeyer, "Direct frequency comb synthesis with arbitrary offset and shot-noise-limited phase noise", Nat. Photon., 4 (2010) 462-65.

[20] T.W. Hänsch, "Nobel Lecture: Passion for precision", Rev. Mod. Phys., 78 (2006) 1297-309.

[21] A. Baltuska, T. Udem, M. Uiberacker, M. Hentschel, E. Goulielmakis, C. Gohle, R. Holzwarth, V.S. Yakovlev, A. Scrinzi, T.W. Hansch, F. Krausz, "Attosecond control of electronic processes by intense light fields", Nature, 421 (2003) 611-15.

[22] F. Krausz, M. Ivanov, "Attosecond physics", Rev. Mod. Phys., 81 (2009) 163-234.

[23] E. Goulielmakis, M. Schultze, M. Hofstetter, V.S. Yakovlev, J. Gagnon, M. Uiberacker, A.L. Aquila, E.M. Gullikson, D.T. Attwood, R. Kienberger, F. Krausz, U. Kleineberg, "Single-Cycle Nonlinear Optics", Science, 320 (2008) 1614-17.

[24] E. Goulielmakis, M. Uiberacker, R. Kienberger, A. Baltuska, V. Yakovlev, A. Scrinzi, T. Westerwalbesloh, U. Kleineberg, U. Heinzmann, M. Drescher, F. Krausz, "Direct Measurement of Light Waves", Science, 305 (2004) 1267-69.

[25] J. Mauritsson, T. Remetter, M. Swoboda, K. Klünder, A. L'Huillier, K.J. Schafer, O. Ghafur, F. Kelkensberg, W. Siu, P. Johnsson, M.J.J. Vrakking, I. Znakovskaya, T. Uphues, S. Zherebtsov, M.F. Kling, F. Lépine, E. Benedetti, F. Ferrari, G. Sansone, M. Nisoli, "Attosecond Electron Spectroscopy Using a Novel Interferometric Pump-Probe Technique", Phys. Rev. Lett., 105 (2010) 053001.

[26] M.F. Kling, C. Siedschlag, A.J. Verhoef, J.I. Khan, M. Schultze, T. Uphues, Y. Ni, M. Uiberacker, M. Drescher, F. Krausz, M.J.J. Vrakking, "Control of Electron Localization in Molecular Dissociation", Science, 312 (2006) 246-48.

[27] G. Sansone, E. Benedetti, F. Calegari, C. Vozzi, L. Avaldi, R. Flammini, L. Poletto, P. Villoresi, C. Altucci, R. Velotta, S. Stagira, S. De Silvestri, M. Nisoli, "Isolated Single-Cycle Attosecond Pulses", Science, 314 (2006) 443-46.

[28] A.L. Cavalieri, N. Muller, T. Uphues, V.S. Yakovlev, A. Baltuska, B. Horvath, B. Schmidt, L. Blumel, R. Holzwarth, S. Hendel, M. Drescher, U. Kleineberg, P.M. Echenique, R. Kienberger, F. Krausz, U. Heinzmann, "Attosecond spectroscopy in condensed matter", Nature, 449 (2007) 1029-32.

[29] S.E. Harris, A.V. Sokolov, "Subfemtosecond Pulse Generation by Molecular Modulation", Phys. Rev. Lett., 81 (1998) 2894-97.

[30] A.V. Sokolov, D.R. Walker, D.D. Yavuz, G.Y. Yin, S.E. Harris, "Raman Generation by Phased and Antiphased Molecular States", Phys. Rev. Lett., 85 (2000) 562-65.

[31] T. Suzuki, M. Hirai, M. Katsuragawa, "Octave-Spanning Raman Comb with Carrier Envelope Offset Control", Phys. Rev. Lett., 101 (2008) 243602.

[32] J.Q. Liang, M. Katsuragawa, F.L. Kien, K. Hakuta, "Sideband Generation Using Strongly Driven Raman Coherence in Solid Hydrogen", Phys. Rev. Lett., 85 (2000) 2474-77.

[33] Z.-M. Hsieh, C.-J. Lai, H.-S. Chan, S.-Y. Wu, C.-K. Lee, W.-J. Chen, C.-L. Pan, F.-G. Yee, A.H. Kung, "Controlling the Carrier-Envelope Phase of Raman-Generated Periodic Waveforms", Phys. Rev. Lett., 102 (2009) 213902.

[34] S. Baker, I.A. Walmsley, J.W.G. Tisch, J.P. Marangos, "Femtosecond to attosecond light pulses from a molecular modulator", Nat. Photon., 5 (2011) 664-71.

[35] H.-S. Chan, Z.-M. Hsieh, W.-H. Liang, A.H. Kung, C.-K. Lee, C.-J. Lai, R.-P. Pan, L.-H. Peng, "Synthesis and Measurement of Ultrafast Waveforms from Five Discrete Optical Harmonics", Science, 331 (2011) 1165-68.

[36] E. Goulielmakis, V.S. Yakovlev, A.L. Cavalieri, M. Uiberacker, V. Pervak, A. Apolonski, R. Kienberger, U. Kleineberg, F. Krausz, "Attosecond Control and Measurement: Lightwave Electronics", Science, 317 (2007) 769-75.

[37] E. Treacy, "Optical pulse compression with diffraction gratings", IEEE J. Quantum Electron., 5 (1969) 454-58.

[38] O.E. Martinez, J.P. Gordon, R.L. Fork, "Negative group-velocity dispersion using refraction", J. Opt. Soc. Am. A, 1 (1984) 1003-06.

[39] R.L. Fork, O.E. Martinez, J.P. Gordon, "Negative dispersion using pairs of prisms", Opt. Lett., 9 (1984) 150-52.

[40] R. Szipöcs, K. Ferencz, C. Spielmann, F. Krausz, "Chirped multilayer coatings for broadband dispersion control in femtosecond lasers", Opt. Lett., 19 (1994) 201-03.

[41] V. Pervak, "Recent development and new ideas in the field of dispersive multilayer optics", Appl. Opt., 50 (2011) C55-C61.

[42] A.M. Weiner, Dispersion and Dispersion Compensation, in: Ultrafast Optics, John Wiley & Sons, Inc., 2008, pp. 147-97.

[43] F. rainbow™, in, .http://www.femtolasers.com/RAINBOW-TM.114.0.html.

[44] R.R. Alfano, S.L. Shapiro, "Emission in the Region 4000 to 7000 Å Via Four-Photon Coupling in Glass", Phys. Rev. Lett., 24 (1970) 584-87.

[45] F. Silva, D.R. Austin, A. Thai, M. Baudisch, M. Hemmer, D. Faccio, A. Couairon, J. Biegert, "Multi-octave supercontinuum generation from mid-infrared filamentation in a bulk crystal", Nat Commun, 3 (2012) 807.

[46] A.M. Zheltikov, "Let there be white light: supercontinuum generation by ultrashort laser pulses", Physics-Uspekhi, 49 (2006) 605.

[47] M. Nisoli, S. DeSilvestri, O. Svelto, R. Szipocs, K. Ferencz, C. Spielmann, S. Sartania, F. Krausz, "Compression of high-energy laser pulses below 5 fs", Opt. Lett., 22 (1997) 522-24.

[48] T. Brabec, F. Krausz, "Intense few-cycle laser fields: Frontiers of nonlinear optics", Rev. Mod. Phys., 72 (2000) 545-91.

[49] C. Lin, R.H. Stolen, "New nanosecond continuum for excited-state spectroscopy", Applied Physics Letters, 28 (1976) 216-18.

[50] Z. Chang, Fundamentals of Attosecond Optics, CRC Press, United States of America, 2011.

[51] C. Froehly, B. Colombeau, M. Vampouille, II Shaping and Analysis of Picosecond Light Pulses, in: E. Wolf (Ed.) Progress in Optics, Elsevier, 1983, pp. 63-153.

[52] A. Monmayrant, S. Weber, B. Chatel, "A newcomer's guide to ultrashort pulse shaping and characterization", J. Phys. B: At. Mol. Opt. Phys, 43 (2010) 103001.

[53] W. Andrew M, "Ultrafast optical pulse shaping: A tutorial review", Opt. Commun., 284 (2011) 3669-92.

[54] A. Monmayrant, B. Chatel, "New phase and amplitude high resolution pulse shaper", Rev. Sci. Instrum., 75 (2004) 2668-71.

[55] M.M. Wefers, K.A. Nelson, "Analysis of programmable ultrashort waveform generation using liquid-crystal spatial light modulators", J. Opt. Soc. Am. B, 12 (1995) 1343-62.

[56] C.W. Hillegas, J.X. Tull, D. Goswami, D. Strickland, W.S. Warren, "Femtosecond laser pulse shaping by use of microsecond radio-frequency pulses", Opt. Lett., 19 (1994) 737-39.

[57] M.A. Dugan, J.X. Tull, W.S. Warren, "High-resolution acousto-optic shaping of unamplified and amplified femtosecond laser pulses", J. Opt. Soc. Am. B, 14 (1997) 2348-58.

[58] I.C. Chang, "Collinear beam acousto-optic tunable filters", Electronics Letters, 28 (1992) 1255-56.

[59] E. Zeek, K. Maginnis, S. Backus, U. Russek, M. Murnane, G. Mourou, H. Kapteyn, G. Vdovin, "Pulse compression by use of deformable mirrors", Opt. Lett., 24 (1999) 493-95.

[60] D.J. Kane, R. Trebino, "Characterization of arbitrary femtosecond pulses using frequency-resolved optical gating", IEEE J. Quantum Electron., 29 (1993) 571-79.

[61] C. Iaconis, I.A. Walmsley, "Spectral phase interferometry for direct electric-field reconstruction of ultrashort optical pulses", Opt. Lett., 23 (1998) 792-94.

[62] H.P. Weber, "Method for Pulsewidth Measurement of Ultrashort Light Pulses Generated by Phase-Locked Lasers using Nonlinear Optics", Journal of Applied Physics, 38 (1967) 2231-34.

[63] R. Trebino, K.W. DeLong, D.N. Fittinghoff, J.N. Sweetser, M.A. Krumbugel, B.A. Richman, D.J. Kane, "Measuring ultrashort laser pulses in the time-frequency domain using frequency-resolved optical gating", Rev. Sci. Instrum., 68 (1997) 3277-95.

[64] L. Cohen, "Time-frequency distributions-a review", Proceedings of the IEEE, 77 (1989) 941-81.

[65] D.J. Kane, "Real-time measurement of ultrashort laser pulses using principal component generalized projections", IEEE J. SEL TOP QUANT., 4 (1998) 278-84.

[66] D.J. Kane, "Recent progress toward real-time measurement of ultrashort laser pulses", IEEE J. Quantum Electron., 35 (1999) 421-31.

[67] R. Trebino, D.J. Kane, "Using phase retrieval to measure the intensity and phase of ultrashort pulses: frequency-resolved optical gating", J. Opt. Soc. Am. A, 10 (1993) 1101-11.

[68] R. Trebino, Frequency-Resolved Optical Gating: The Measurement of Ultrashort Laser Pulses, Kluwer Academic, Massachusetts 2000.

[69] A.C. Eckbreth, "BOXCARS: Crossed-beam phase-matched CARS generation in gases", Applied Physics Letters, 32 (1978) 421-23.

[70] M.T. Hassan, A. Wirth, I. Grguras, A. Moulet, T.T. Luu, J. Gagnon, V. Pervak, E. Goulielmakis, "Invited Article: Attosecond photonics: Synthesis and control of light transients", Rev. Sci. Instrum., 83 (2012) 111301-19.

[71] A. Wirth, M.T. Hassan, I. Grguraš, J. Gagnon, A. Moulet, T.T. Luu, S. Pabst, R. Santra, Z.A. Alahmed, A.M. Azzeer, V.S. Yakovlev, V. Pervak, F. Krausz, E. Goulielmakis, "Synthesized Light Transients", Science, 334 (2011) 195-200.

[72] J. Itatani, F. Quéré, G.L. Yudin, M.Y. Ivanov, F. Krausz, P.B. Corkum, "Attosecond Streak Camera", Phys. Rev. Lett., 88 (2002) 173903.

[73] V.S. Yakovlev, J. Gagnon, N. Karpowicz, F. Krausz, "Attosecond Streaking Enables the Measurement of Quantum Phase", Phys. Rev. Lett., 105 (2010) 073001.

[74] M. Kitzler, N. Milosevic, A. Scrinzi, F. Krausz, T. Brabec, "Quantum Theory of Attosecond XUV Pulse Measurement by Laser Dressed Photoionization", Phys. Rev. Lett., 88 (2002) 173904.

[75] J. Gagnon, E. Goulielmakis, V.S. Yakovlev, "The accurate FROG characterization of attosecond pulses from streaking measurements", Applied Physics B: Lasers and Optics, 92 (2008) 25-32.

[76] J. Gagnon, V. Yakovlev, "The direct evaluation of attosecond chirp from a streaking measurement", Applied Physics B: Lasers and Optics, 103 (2011) 303-09.

[77] M.T. Hassan, A. Wirth, I. Grguras, A. Moulet, T.T. Luu, J. Gagnon, V. Pervak, E. Goulielmakis, "Invited Article: Attosecond photonics: Synthesis and control of light transients", Rev. Sci. Instrum., 83 (2012) 111301.

[78] M. Lewenstein, P. Balcou, M.Y. Ivanov, A. L'Huillier, P.B. Corkum, "Theory of high-harmonic generation by low-frequency laser fields", Phys. Rev. A, 49 (1994) 2117-32.

[79] M. Protopapas, D.G. Lappas, C.H. Keitel, P.L. Knight, "Recollisions, bremsstrahlung, and attosecond pulses from intense laser fields", Phys. Rev. A, 53 (1996) R2933-R36.

[80] M. Protopapas, C.H. Keitel, P.L. Knight, "Atomic physics with super-high intensity lasers", Reports on Progress in Physics, 60 (1997) 389.

[81] B. W., F. Grasbon, D.B. Kopold, D.B. Miloševič, G.G. Paulus, H. Walther, "Above-Threshold Ionization: From Classical Features to Quantum Effects", Advances in Atomic Molecular and Optical Physics, 48 (2002) 36-98.

[82] L.V. Keldysh, "Ionization in the field of a strong electromagnetic wave", Sov. Phys. JETP, 20 (1965) 1307.

[83] D.M. Wolkow, "Über eine Klasse von Lösungen der Diracschen Gleichung", Zeitschrift für Physik A Hadrons and Nuclei, 94 (1935) 250-60.

[84] E. Mevel, P. Breger, R. Trainham, G. Petite, P. Agostini, A. Migus, J.-P. Chambaret, A. Antonetti, "Atoms in strong optical fields: Evolution from multiphoton to tunnel ionization", Phys. Rev. Lett., 70 (1993) 406-09.

[85] S. Augst, D. Strickland, D.D. Meyerhofer, S.L. Chin, J.H. Eberly, "Tunneling ionization of noble gases in a high-intensity laser field", Phys. Rev. Lett., 63 (1989) 2212-15.

[86] G.L. Yudin, M.Y. Ivanov, "Nonadiabatic tunnel ionization: Looking inside a laser cycle", Phys. Rev. A, 64 (2001) 013409.

[87] J.L. Krause, K.J. Schafer, K.C. Kulander, "High-order harmonic generation from atoms and ions in the high intensity regime", Phys. Rev. Lett., 68 (1992) 3535-38.

[88] P.B. Corkum, "Plasma perspective on strong field multiphoton ionization", Phys. Rev. Lett., 71 (1993) 1994-97.

[89] P.B. Corkum, F. Krausz, "Attosecond science", Nat. Phys., 3 (2007) 381-87.

[90] K. Varj´u, P. Johnsson, R. L´opez-Martens, T. Remetter, E. Gustafsson, J. Mauritsson, M.B. Gaarde, K.J. Schafer, C. Erny, I. Sola, A. Za¨ır, E. Constant, E. Cormier, E. M´evel, A. L'Huillier, "Experimental studies of attosecond pulse trains", Laser. Phys., 15 (2005).

[91] I.J. Sola, E. Mevel, L. Elouga, E. Constant, V. Strelkov, L. Poletto, P. Villoresi, E. Benedetti, J.P. Caumes, S. Stagira, C. Vozzi, G. Sansone, M. Nisoli, "Controlling attosecond electron dynamics by phase-stabilized polarization gating", Nat. Phys., 2 (2006) 319-22.

[92] X. Feng, S. Gilbertson, H. Mashiko, H. Wang, S.D. Khan, M. Chini, Y. Wu, K. Zhao, Z. Chang, "Generation of Isolated Attosecond Pulses with 20 to 28 Femtosecond Lasers", Phys. Rev. Lett., 103 (2009) 183901.

[93] J. Rauschenberger, T. Fuji, M. Hentschel, A.J. Verhoef, T. Udem, C. Gohle, T.W. Hänsch, F. Krausz, "Carrier-envelope phase-stabilized amplifier system", Laser Physics Letters, 3 (2006) 37-42.

[94] J.R. T. Fuji, C. Gohle, A. Apolonski, T. Udem, V. S. Yakovlev,G. Tempea, T. W. Hänsch, and F. Krausz, "Attosecond control of optical waveforms", New. J. Phys., 7 (2005) 116.

[95] S.T. Cundiff, "Phase stabilization of ultrashort optical pulses", Journal of Physics D: Applied Physics, 35 (2002).

[96] A.L. Cavalieri, E. Goulielmakis, B. Horvath, W. Helml, M. Schultze, M. Fiess, V. Pervak, L. Veisz, V.S. Yakovlev, M. Uiberacker, A. Apolonski, F. Krausz, R. Kienberger, "Intense 1.5-cycle near infrared laser waveforms and their use for the generation of ultra-broadband soft-x-ray harmonic continua", New. J. Phys., 9 (2007).

[97] G.G. Paulus, F. Lindner, H. Walther, A. Baltuška, E. Goulielmakis, M. Lezius, F. Krausz, "Measurement of the Phase of Few-Cycle Laser Pulses", Phys. Rev. Lett., 91 (2003) 253004.

[98] I. Znakovskaya, P. von den Hoff, S. Zherebtsov, A. Wirth, O. Herrwerth, M.J.J. Vrakking, R. de Vivie-Riedle, M.F. Kling, "Attosecond Control of Electron Dynamics in Carbon Monoxide", Phys. Rev. Lett., 103 (2009) 103002.

[99] S. Zherebtsov, T. Fennel, J. Plenge, E. Antonsson, I. Znakovskaya, A. Wirth, O. Herrwerth, F. Suszmann, C. Peltz, I. Ahmad, S.A. Trushin, V. Pervak, S. Karsch, M.J.J. Vrakking, B. Langer, C. Graf, M.I. Stockman, F. Krausz, E. Ruhl, M.F. Kling, "Controlled near-field enhanced electron acceleration from dielectric nanospheres with intense few-cycle laser fields", Nat. Phys., 7 (2011) 656-62.

[100] A. Baltuska, M. Uiberacker, E. Goulielmakis, R. Kienberger, V.S. Yakovlev, T. Udem, T.W. Hansch, F. Krausz, "Phase-controlled amplification of few-cycle laser pulses", IEEE J. SEL TOP QUANT., 9 (2003) 972-89.

[101] T. Wittmann, B. Horvath, W. Helml, M.G. Schatzel, X. Gu, A.L. Cavalieri, G.G. Paulus, R. Kienberger, "Single-shot carrier-envelope phase measurement of few-cycle laser pulses", Nat. Phys., 5 (2009) 357-62.

[102] "Calculation of the probability of photoprocesses induced by ultrashort electromagnetic pulses", Russian Physics Journal, (2010).

[103] A.V. Tikhonravov, M.K. Trubetskov, G.W. DeBell, "Application of the needle optimization technique to the design of optical coatings", Appl. Opt., 35 (1996) 5493-508.

[104] J.N. Sweetser, D.N. Fittinghoff, R. Trebino, "Transient-grating frequency-resolved optical gating", Opt. Lett., 22 (1997) 519-21.

[105] "Spectral analysis and control to obtain sub-5 fs pulses by femtosecond filamentation", Opt. Lett., 33 (2008) 2964.

[106] V.A. Astapenko, "Simple formula for photoprocesses in ultrashort electromagnetic field", Physics Letters A, 374 (2010) 1585.

[107] Y.-X. Wang, Z. Yang, S.-J. Xiong, "Study of Zitterbewegung in graphene bilayer with perpendicular magnetic field", EPL (Europhysics Letters), 89 (2010) 17007.

[108] M. Schultze, A. Wirth, I. Grguras, M. Uiberacker, T. Uphues, A.J. Verhoef, J. Gagnon, M. Hofstetter, U. Kleineberg, E. Goulielmakis, F. Krausz, "State-of-the-art attosecond metrology", J Electron Spectrosc, 184 (2011) 68-77.

[109] G. Time-of-flight (TOF) Spectrometers manufactured by Stefan Kaesdorf, für Forschung und Industrie, "http://www.kaesdorf.de/", http://www.kaesdorf.de/.

[110] C. Dorrer, I.A. Walmsley, "Accuracy criterion for ultrashort pulse characterization techniques: application to spectral phase interferometry for direct electric field reconstruction", J. Opt. Soc. Am. B, 19 (2002) 1019-29.

[111] P.M. Paul, E.S. Toma, P. Breger, G. Mullot, F. Augé, P. Balcou, H.G. Muller, P. Agostini, "Observation of a Train of Attosecond Pulses from High Harmonic Generation", Science, 292 (2001) 1689-92.

[112] W.R. Hunter, "High Reflectance Coatings for the Extreme Ultra-violet", Optica Acta: International Journal of Optics, 9 (1962) 255-68.

[113] L.A. Stelmack, Vacuum ultraviolet reflectance filter in: A.R. Corporation (Ed.), United States, 1980.

[114] A. Wirth, Attosecond Transient Absorption Spectroscopy, in: Fakultät für Physik Ludwig-Maximilians-Universität, 2011.

[115] A. Wirth, R. Santra, E. Goulielmakis, "Real time tracing of valence-shell electronic coherences with attosecond transient absorption spectroscopy", Chem. Phys.

[116] R. Santra, V.S. Yakovlev, T. Pfeifer, Z.-H. Loh, "Theory of attosecond transient absorption spectroscopy of strong-field-generated ions", Phys. Rev. A, 83 (2011) 033405.

[117] S. Pabst, A. Sytcheva, A. Moulet, A. Wirth, E. Goulielmakis, R. Santra, "Theory of attosecond transient-absorption spectroscopy of krypton for overlapping pump and probe pulses", Phys. Rev. A, 86 (2012) 063411.

[118] L. Greenman, P.J. Ho, S. Pabst, E. Kamarchik, D.A. Mazziotti, R. Santra, "Implementation of the time-dependent configuration-interaction singles method for atomic strong-field processes", Phys. Rev. A, 82 (2010) 023406.

[119] S. Pabst, L. Greenman, P.J. Ho, D.A. Mazziotti, R. Santra, "Decoherence in Attosecond Photoionization", Phys. Rev. Lett., 106 (2011) 053003.

[120] A. Baltuska, T. Udem, M. Uiberacker, M. Hentschel, E. Goulielmakis, C. Gohle, R. Holzwarth, V. Yakovlev, A. Scrinzi, T. Hänsch, F. Krausz, "Attosecond control of electronic processes by intense light fields", Nature, 421 (2003) 611-15.

[121] D.E. Leaird, A.M. Weiner, "Femtosecond optical packet generation by a direct space-to-time pulse shaper", Opt. Lett., 24 (1999) 853-55.

[122] F. Remacle, M. Nest, R.D. Levine, "Laser Steered Ultrafast Quantum Dynamics of Electrons in LiH", Phys. Rev. Lett., 99 (2007) 183902.

[123] P. von den Hoff, R. Siemering, M. Kowalewski, R. de Vivie-Riedle, "Electron Dynamics and Its Control in Molecules: From Diatomics to Larger Molecular Systems", IEEE J. SEL TOP QUANT., 18 (2012) 119-29.

[124] F. Reiter, U. Graf, E.E. Serebryannikov, W. Schweinberger, M. Fiess, M. Schultze, A.M. Azzeer, R. Kienberger, F. Krausz, A.M. Zheltikov, E. Goulielmakis, "Route to Attosecond Nonlinear Spectroscopy", Phys. Rev. Lett., 105 (2010) 243902.

[125] T. Fuji, T. Suzuki, "Generation of sub-two-cycle mid-infrared pulses by four-wave mixing through filamentation in air", Opt. Lett., 32 (2007) 3330-32.

Data archiving

The experimental raw data, the evaluation files, and the figures can be found on the Data Archive Sever of the Laboratory for Attosecond Physics at the Max Planck Institute of Quantum Optics. The Archiving has been as follows;

The next table shows the number and description for the figures following the order as they appear in the thesis. Moreover, it shows also if the figure is illustration, measurement or a simulation and which tool has been used for that, at the last row of the table it shows the path in the archiving folder.
In the archiving folder a word file named "**Measurement and analysis**", in this document we show the measurements have been done in the framework of the thesis with full explanations how it is measured, the apparatus, and the software have been used in the acquisition process and the analysis of the data.
Another folder in the archive named "**Tools**" contains all the tools(software's, Matlab scripts, labview, …etc.) has been used in this work

Data Archiving Table

Figure	Content	Type	measurement / simulation type	Measured	Tool	Archive file
Fig1.1	The phase effects on the pulse properties	Illustration				chapter1/Fig.1.1/
Fig1.2	Ultrafast laser pulse dispersion control	Illustration				chapter1/Fig.1.2/
Fig1.3	Principles of light synthesis	Illustration				chapter1/Fig.1.3/
Fig1.4	Principles of light field synthesis	Illustration				chapter1/Fig.1.4/
Fig1.5	The process of cascaded Raman scattering	Illustration				chapter1/Fig.1.5/
Fig1.6	4f-line arrangement set up of pulse shaper	Illustration				chapter1/Fig.1.6/
Fig1.7	Waveform synthesis of harmonics generated in molecular modulator	Illustration				chapter1/Fig.1.7/
Fig1.8	Scheme diagram of retrieving algorithm for FROG trace	Illustration				chapter1/Fig.1.8/
Fig1.9	Transient grating (TG-FROG) geometry	Illustration				chapter1/Fig.1.9/
Fig1.10	The concept of attosecond light field sampling	Illustration				chapter1/Fig.1.10/
Fig1.11	Attosecond streak camera principle	Illustration				chapter1/Fig.1.11/
Fig1.12	Attosecond streak camera principle in case of chirped attosecond XUV pulse	Illustration				chapter1/Fig.1.12/
Fig2.1	The mechanisms of photoionization	Illustration				chapter2/Fig.2.1/
Fig2.2	The HHG spectra	Illustration				chapter2/Fig.2.2/
Fig2.3	Illustration for the three-step model explains HHG mechanism	Illustration				chapter2/Fig.2.3/
Fig2.4	Generation of single isolated attosecond light bursts by	Illustration				chapter2/Fig.2.4/
Fig3.1	Scheme illustrates the commercially available front end laser	Illustration				Chapter 3/Fig3.1/

	system					
Fig3.2	The characterization of the laser amplified pulse	Experimental measurement	FROG and spectrum measurement	FROG trace and spectrum	TG-FROG and HR4000 ocean optics spectrometer	Chapter 3/Fig3.2/
Fig3.3	scheme for f-to-zero measurement	Illustration				Chapter 3/Fig3.3/
Fig3.4	Scheme for f-to-2f measurement	Illustration				Chapter 3/Fig3.4/
Fig3.5	f-2f interferometer setup	Illustration				Chapter 3/Fig3.5/
Fig4.1	Supercontinuum light generation	Illustration and Experimental measurement	Spectrum measurement	spectrum	HR4000 ocean optics spectrometer	Chapter 4/Fig4.1/and With elat, Science2011/Fig1B
Fig4.2	Prototypical three-channel (1.5 –octave) light field synthesizer	Illustration				Chapter 4/Fig4.2/
Fig4.3	Dichroic Beamsplitters	Illustration and theoretical calculation				Chapter 4/Fig4.3/
Fig4.4	Uncompressed measured pulses of the constituent channels	Experimental measurement	FROG measurement	FROG trace	TG-FROG appratus	Chapter 4/Fig4.4/
Fig4.5	Spectra of pulses in the constituent channels of the three channel synthesizer	Experimental measurement	FROG measurement	FROG trace	TG-FROG appratus	Chapter 4/Fig4.5/
Fig4.6	Temporal characterization of three channel synthesizer pulses	Experimental measurement	FROG measurement	FROG trace	TG-FROG appratus	Chapter 4/Fig4.6/and With elat, Science2011/Fig1C
Fig4.7	Spatial overlap of the constituent beams in the field synthesizer	Illustration and Experimental measurement	Beam profile measurement	Beam profile capture	DAT-WinCamD-XHR	Chapter 4/Fig4.7/
Fig4.8	Divergence of the constituent beams in the field synthesizer	Illustration and Experimental measurement	Beam profile measurement	Beam profile capture	DAT-WinCamD-XHR	Chapter 4/Fig4.8/
Fig4.9	Temporal synchronization of the constituent channels in the field synthesizer	Illustration and Experimental measurement	Spectrum measurement	spectrum	HR4000 ocean optics spectrometer	Chapter 4/Fig4.9/
Fig4.10	The passive stabilization of the light field synthesizer	Illustration				Chapter 4/Fig4.10/
Fig4.11	Active interferometric stabilization of the light field synthesizer	Illustration and Experimental measurement	Spectrum measurement	spectrum	HR4000 ocean optics spectrometer	Chapter 4/Fig4.11/
Fig5.1	Apparatus for sampling the synthesized field transients and attosecond pump-probe exper-	Illustration				Chapter 5/Fig5.1/

	iments					
Fig5.2	Sampling set up of the synthesized light transients	Illustration				Chapter 5/Fig5.2/
Fig5.3	The temporal profile of the EUV attosecond pulse implies for sampling synthesized light transients	Experimental measurement	Streaking measurement	Streaking spectrogram	TOF spectrometer	Chapter 5/Fig5.3/
Fig5.4	Subcycle light transient	Experimental measurement	Streaking measurement	Streaking spectrogram	TOF spectrometer	Chapter 5/Fig5.4/and With elat, Science2011/Fig2F
Fig5.5	Demonstration of the sampling stability	Experimental measurement	Streaking measurement	Streaking spectrogram	TOF spectrometer	Chapter 5/Fig5.5/
Fig5.6	Designing a light transient	Illustration and simulation	LFS script	Simulated electric field	LFS script	Chapter 5/Fig5.6/
Fig5.7	Light field synthesis with subcycle resolution	Experimental measurement and simulation calculation	Streaking measurement and LFS script	Streaking spectrogram and predicted electric field	TOF spectrometer	Chapter 5/Fig5.7/and With elat, Science2011/Fig2A,2B and 2C
Fig5.8	Light field synthesis for complex light transients	Experimental measurement and simulation calculation	Streaking measurement and LFS script	Streaking spectrogram and predicted electric field	TOF spectrometer	Chapter 5/Fig5.8/and With elat, Science2011/Fig2D and 2E
Fig6.1	Simulated attosecond light transient (ATL).	Simulation calculation	LFS script	Simulated electric field	LFS script	Chapter 6/Fig6.1/
Fig6.2	Spectra of pulses in the constituent channels of the four channel synthesizer	Experimental measurement	Spectrum measurement	spectrum	HR4000 ocean optics spectrometer	Chapter 6/Fig6.2/
Fig6.3	The reflectivity of the Aluminum coated reflector at different incident angles	Experimental measurement	Optics coating design	Reflectivity curve		Chapter 6/Fig6.3/
Fig6.4	The grazing incident set up for transferring the 2-octave supercontinuum	Illustration				Chapter 6/Fig6.4/
Fig6.5	The designed reflectivity of Ch_{DUV} optics	theoretical calculation				Chapter 6/Fig6.5/
Fig6.6	Uncompressed pulse of Ch_{DUV}	Experimental measurement	FROG measurement	FROG trace	TG-FROG apparatus	Chapter 6/Fig6.6/
Fig6.7	Group-delay dispersion (GDD) of the synthesizer channels	Experimental measurement	FROG measurement	FROG trace	TG-FROG apparatus	Chapter 6/Fig6.7/
Fig6.8	Prototypical four channel (2 – octave) light field synthesizer	Illustration				Chapter 6/Fig6.8/
Fig6.9	Temporal characterization of the pulses in the four-channel	Experimental measurement	FROG measurement	FROG trace	TG-FROG apparatus	Chapter 6/Fig6.9/

	light field synthesizer					
Fig6.10	The beam profiles of the pulses in the four-channel light field synthesizer	Experimental measurement	Beam profile measurement	Beam profile capture	DAT-WinCamD-XHR	Chapter 6/Fig6.10/
Fig6.11	Active stabilization for the Ch_{DUV}	Experimental measurement	Spectrum measurement	spectrum	HR4000 ocean optics spectrometer	Chapter 6/Fig6.11/
Fig6.12	2-octave light field transient	Experimental measurement	Streaking measurement	Streaking spectrogram	TOF spectrometer	Chapter 6/Fig6.12/
Fig6.13	The Metallic-Dielectric-Metallic (MDM) mirror coating design	simulation calculation	IMD4.1.1.1 soft wear calculations	Reflectivity curves	IMD4.1.1.1 soft wear	Chapter 6/Fig6.13/
Fig6.14	Metallic–dichroic-metallic (MDM) outer mirror	Experimental measurement and simulation calculation	IMD4.1.1.1 soft wear and spectrum measurement	Reflectivity curve and measured spectrum	IMD4.1.1.1 soft wear and HR4000 ocean optics spectrometer	Chapter 6/Fig6.14/
Fig6.15	Complex synthesize of the subcycle light transient	Experimental measurement	Streaking measurement	Streaking spectrogram	TOF spectrometer	Chapter 6/Fig6.15/
Fig6.16	Attosecond light transient	Experimental measurement	Streaking measurement	Streaking spectrogram	TOF spectrometer	Chapter 6/Fig6.16/
Fig7.1	General layout of a pump-probe experiment in lab frame	Illustration				Chapter 7/Fig7.1/
Fig7.2	Transient absorption principle	Illustration				Chapter 7/Fig7.2/
Fig7.3	The transient absorption spectroscopy setup	Illustration				Chapter 7/Fig7.3/
Fig7.4	Ionization with a subcycle light field transient	Experimental measurement	Streaking measurement and transient absorption measurement		TOF spectrometer and Model 248/310G Grazing Incidence Monochromator	Chapter 7/Fig7.4/ and Wirth elat, Science2011/Fig3.a,Fig3.b and Fig3.c
Fig7.5	Population dynamics of Kr^+	Experimental measurement	Transient absorption measurement	Transient Absorption spectrogram	Model 248/310G Grazing Incidence Monochromator	Chapter 7/Fig7.5/ and Wirth elat, Science2011/Fig4.a,Fig4.b
Fig7.6	Initial quantum phase and density distribution of a valence electron wavepacket	Experimental measurement and simulation calculation	Transient absorption measurement	Transient Absorption spectrogram	Model 248/310G Grazing Incidence Monochromator	Chapter 7/Fig7.6/ and With elat, Science2011/Fig5
Fig7.7	Controlling of the electronic wavepacket in ionized atom	Illustration				Chapter 7/Fig7.7/
Fig7.8	Attosecond polarization control	Experimental measurement	VUV spectrum measurement	VUV spectra	Model 234/302 Vacuum Ultraviolet Monochromator	Chapter 7/Fig7.8/
Fig8.1	Synthesized light transients appropriate for encoding of	Experimental				Chapter 8/Fig8.1/

	digital information	measurement				
FigA.1	XUV multilayer coated mirror	Simulation calculation				Appendix/FigA.1/
FigA.2	Simulated reflectivity curve of broadband molybdenum-silicon EUV imaging mirror	Simulation calculation				Appendix/FigA.2/
FigA.3	cross-correlation measurement obtained under streaking and transient absorption intensity settings	Experimental measurement	Cross correlation measurement		HR4000 ocean optics spectrometer	Appendix/FigA.3/

Acknowledgment

I am very grateful to Prof. Ferenc Krausz for providing me the opportunity to perform my PhD studies in his division at the Max Planck Institute of Quantum Optics. The excellent research conditions allowed me to substantially advance my scientific experience.

I would like to express my deepest gratefulness to Eleftherios Goulielmakis for giving me the opportunity to work in his research group (Attoelectronics) and for supervising my PhD project. He provided me great training and feedback in all important aspects of science. Despite all his other tasks, he still invested countless hours with us in the lab and this has allowed me not only to collect very high level of experience but also to learn the spirit of planning of complex experiments.

I am especially thankful to Adrian Wirth, Tran Trung Luu, Antoine Moulet as well as my new colleague Manish Garg for their contributions. I would like to express my thanks also to Vladimir Pervak and Olga Razskazovskaya for their invaluable contributions on the side of ultrafast optics, coating and their excellent designs as well as to Justin Gagnon, Antoine Moulet and Tran Trung Luu for supporting the analysis of the experimental data of this thesis with excellent computational tools.

Furthermore, I am very thankful to Alexander Guggenmos, Michael Hofstetter and Prof. Ulf Kleineberg for providing unique EUV optics for the transient absorption and light field synthesis. The success of the PhD work is also based on the work of several previous colleagues who have explored the basic concept of light field synthesizer and the development of the attosecond beamline. I am grateful to Ivanka Grguras for her great work in previous stages of the light synthesis project, Martin Schultze, Adrian Wirth, and Florentin Reiter.

I am also grateful to Reinhard Kienberger, Matthias Kling, Prof. Abdallah M. Azzeer, Zeyad A. Alahmed, Martin Schultze, Nicholas Karpowicz, Laszlo Veisz and Vladislav Yakovlev for stimulating discussions.

Thanks goes to my colleagues; Wolfram Helml, Elisabeth Bothschafter, Christoph Skrobol, Michael Jobst, Elisabeth Magerl, Patrick Heißler, Hanieh Fattahi, Wolfgang Schweineberger, Frederik Sußmann, Izhar Ahmad, Sergei Trushin, Alexander Kessel, Matthias Kübel, Alexander Schwarz, Sabine Keiber, Tim Paasch-Colberg, Christoph Wandt, and Annkatrin Sommer, you made the atmosphere in the lab and outside always very pleasant for me.

I acknowledge great and prompt support from our workshop team especially to Thomas Strobl, for realizing my design for the synthesizer baseplate on a very short time scale beside all the other required components. Thanks to the entire purchasing department (Caroline Zenger, Claudia Schenker, Carina Steinkrebs, and Thomas Florian as they had to process a lot of orders in limited time.

I would like also to thank: Johannes Wulz, Alois Böswald, Harald Haas, Manfred Fischer, Walter Fölsner, Anton Horn, and Tobias Kleinhenz for the great technical support.

Last, but not least, I would like to express my gratefulness to the administrative staff of Prof. Krausz' office (Monika Wild, Franziska Hoss, Valentina Rot, Simone Mann, Bernd Ullmann, Thorsten Naeser and Christine Kortenbruck), as well as the coordinators of International Max Planck Research School on Advanced Photon Sciences (IMPRS-APS), especially to the coordinators Matthias Kling, Peter Hommelhoff, Nicholas Karpowicz and Vladislav Yakovlev.

International Oral Conference Presentations

[C1] **Synthesis and Applications of Subcycle Light Transients** ,
UP 2012, July, 2012, Lausanne, Switzerland.

[C2] **Sub-optical-cycle waveform light synthe-**
sis, **CLEO11**, May 201, Munich, Germany.

[C3] **Preparation and study nanofibers and nano-composites polymer**,
AMAAV, Jan 2009,Cairo, Egypt.

Publications

[P1] **Attosecond light transients**
M. Th. Hassan, et.al, in preparation.

[P2] **"Invited Article":Attosecond Photonics**: **Synthesis and Control of Light Transients**
M. Th. Hassan, A. Wirth, I. Grguraš, A. Moulet, T.T. Luu, J. Gagnon,
V. Pervak and E. Goulielmakis,
Rev. Sci. Instrum., 83 (2012) 111301-19.

[P3] **Synthesized Light Transients**
A. Wirth, **M. Hassan**, I. Grguraš, J. Gagnon, A. Moulet, T.T. Luu, S. Pabst, R. Santra, Z. Alahmed, A.M. Azzeer, V.S. Yakovlev, V. Pervak, F. Krausz and E. Goulielmakis, ,
SCIENCE, DOI: 10.1126/science.1210268 (2011).